

Bioactive Silicon Oxycarbide Based Glasses & Glass-ceramics

A dissertation approved by the Department of Materials and Earth Sciences in fulfilment
of the requirements for the degree of Doctor-Ingenieur (Dr.-Ing.)

M.Sc. Fangtong Xie

Born on 17.07.1990 in Jiangxi, China

First assessor: PD Dr. Emanuel Ionescu

2020 – Darmstadt – D-17

Second assessor: Prof. Dr.-Ing. Aldo R. Boccaccini



TECHNISCHE
UNIVERSITÄT
DARMSTADT



Bioactive silicon oxycarbide based glasses & glass-ceramics

Genehmigte Dissertation von M.Sc. Fangtong Xie aus Jiangxi, China

Fachbereich Material- und Geowissenschaften, Technische Universität Darmstadt

Jahr der Veröffentlichung der Dissertation auf TUpriints: 2020

1. Gutachter: PD Dr. Emanuel Ionescu

2. Gutachter: Prof. Dr.-Ing. Aldo R. Boccaccini

Tag der Einreichung: 17.12.2019

Tag der Prüfung: 06.03.2020

Darmstadt D-17

URN: urn:nbn:de:tuda-tuprints-115458

Veröffentlicht unter CC BY-SA 4.0 International

<https://creativecommons.org/licenses/>

“A journey of a thousand miles begins with a single step”

----- Laozi

“千里之行始于足下”

----- 老子

Declaration of Authorship

I hereby declare that the thesis submitted is my own unaided work. All direct or indirect sources used are acknowledged as references.

I am aware that the thesis in digital form can be examined for the use of unauthorized aid and in order to determine whether the thesis as a whole or parts incorporated in it may be deemed as plagiarism. For the comparison of my work with existing sources I agree that it shall be entered in a database where it shall also remain after examination, to enable comparison with future theses submitted. Further rights of reproduction and usage, however, are not granted here.

This thesis was not previously presented to another examination board and has not been published.

Eidesstattliche Erklärung

Ich erkläre hiermit ehrenwörtlich, dass ich die vorliegende Arbeit selbständig angefertigt habe. Die aus fremden Quellen direkt und indirekt übernommenen Gedanken sind als solche kenntlich gemacht.

Ich weiß, dass die Arbeit in digitalisierter Form daraufhin überprüft werden kann, ob unerlaubte Hilfsmittel verwendet wurden und ob es sich – insgesamt oder in Teilen – um ein Plagiat handelt. Zum Vergleich meiner Arbeit mit existierenden Quellen darf sie in eine Datenbank eingestellt werden und nach der Überprüfung zum Vergleich mit künftig eingehenden Arbeiten dort verbleiben. Weitere Vervielfältigungs- und Verwertungsrechte werden dadurch nicht eingeräumt.

Die Arbeit wurde weder einer anderen Prüfungsbehörde vorgelegt noch veröffentlicht.

Darmstadt, 14.03.2020

(Fangtong Xie)

Table of Contents

Table of Contents	I
List of Abbreviations.....	III
List of Symbols.....	V
Abstract	VII
Zusammenfassung.....	IX
1. Scope and Motivation	1
2. Fundamentals and State of the Art.....	3
2.1. Silicon oxycarbide.....	3
2.1.1. Polymer derived ceramic method.....	4
2.1.2. Structure of silicon oxycarbide	5
2.1.3. Modification of silicon oxycarbide.....	9
2.2. Biomaterials and bioactive glasses	11
2.2.1. Classification and mechanism of bioactivity	12
2.2.2. Therapeutic effects of released ions	15
2.2.3. Processing of bioactive glasses	17
2.3. Silicon oxycarbide for prospective biomedical applications	19
2.3.1. Biocompatibility of silicon oxycarbide	20
2.3.2. Bioactivity of silicon oxycarbide	23
2.3.3. Silicon oxycarbide based surface active materials.....	24
3. Experimental Procedure	26
3.1. Material preparation.....	26
3.1.1. PMS derived silicon oxycarbide	26
3.1.2. Sol-gel derived silicon oxycarbide	27
3.2. Bioactivity assessment	29
3.2.1. Simulated body fluid	29
3.2.2. TC04 method	29
3.3. Material characterization	31
3.3.1. Elemental analysis.....	31
3.3.2. Thermogravimetric analysis with evolved gas analysis.....	31
3.3.3. X-ray diffraction	31
3.3.4. Fourier-transform infrared spectroscopy	31
3.3.5. Transmission electron microscopy	32
3.3.6. Scanning electron microscopy	32
3.3.7. Solid state nuclear magnetic resonance	32
3.3.8. Laser particle size analysis	33
3.3.9. Zeta potential analysis.....	33
3.3.10. Inductively coupled plasma - optical emission spectroscopy analysis	33
3.3.11. N ₂ sorption analysis	33

4. Results and Discussion	34
4.1. PMS derived Si(B,Ca)OC bioactive materials	34
4.1.1. Polymer-to-ceramic transformation.....	34
4.1.2. Structure characterization	38
4.1.3. Ion release kinetics upon SBF exposure	48
4.1.4. Biomineralization upon SBF exposure	53
4.1.5. Structure-bioactivity correlation	61
4.2. PMS derived Si(B,Ca,Sr)OC bioactive materials.....	64
4.2.1. Structure characterization	64
4.2.2. Ion release kinetics upon SBF exposure	65
4.2.3. Biomineralization upon SBF exposure	69
4.3. Sol-gel derived Si(Ca)OC bioactive materials	73
4.3.1. Structure characterization	74
4.3.2. Biomineralization upon SBF exposure	86
4.3.3. Structure-property correlation	89
5. Conclusion and Outlook	90
6. References.....	92
Acknowledgement	103
List of Figures	104
List of Tables.....	106
Curriculum Vitae	107
List of publications.....	108

List of Abbreviations

BET	Brunauer-Emmett-Teller theory
BJH	Barrett-Joyner-Halenda method
CVD	Chemical vapor deposition
EDS	Energy dispersive spectroscopy
EGA	Evolved gas analysis
FTIR	Fourier-transform infrared spectroscopy
HA	Hydroxyapatite
HCA	Carbonated hydroxyapatite
HEC-1-A	Human uterus/endometrium epithelial cell
HEK-293	Human embryonic kidney cell
ICP-OES	Inductively coupled plasma-optical emission microscopy
L929	Mouse fibroblast cell
LDH	Lactate dehydrogenase
LO	Longitudinal-optic Si-O-Si asymmetric stretching
MAS	Magic angle spinning
MEF	Mouse embryonic fibroblast cell
MG-63	Human osteosarcoma cell
MT-2	Human lymphoblastic cell
NBO	Non-bridging-oxygen
NC	Network connectivity
NMR	Nuclear magnetic resonance
OV	Overlapping Si-O-Si and Si-C vibrations
PDC	Polymer derived ceramic
PMS	Polymethylsilsesquioxane
PPP	Platelet poor plasma
PRP	Platelet rich plasma
PSD	Particle size distribution
SAXS	Small-angle X-ray scattering

SBF	Simulated body fluid
SEM	Scanning electron microscopy
Si(B,Ca)OC	Boron and/or calcium modified silicon oxycarbide
Si(B,Ca,Sr)OC	Boron, calcium and strontium modified silicon oxycarbide
Si(Ca)OC	Ca modified silicon oxycarbide
Si(Fe)OC	Fe modified silicon oxycarbide
Si(M)OC	Metal modified silicon oxycarbide
Si(Sn)OC	Sn modified silicon oxycarbide
SiOC	Silicon oxycarbide
SSA	Specific surface area
TC04	Technical committee on Bioglasses
TEM	Transmission electron microscopy
TGA	Thermogravimetric analysis
TO	Transverse-optic Si-O-Si asymmetric stretching
TPPM	Two pulse phase modulation
Tris	Tris(hydroxymethyl)aminomethane
XRD	X-ray diffraction

List of Symbols

$\text{BO}_x\text{C}_{3-x}$	Boron unit with boron connecting to x oxygen atoms and 3-x carbon atoms
C_Q	Quadrupolar coupling constant
d_{50}	Average particle size
E_a	Activation energy for Si release
M^I	Alkali metal
M^{II}	Alkaline earth metal
Q^n	SiO_4 tetrahedron with n bridging oxygens (n ranging from 0 to 4)
R	Universal constant of gas
$\text{SiO}_x\text{C}_{4-x}$	Silicon unit with silicon connecting to x oxygen atoms and 4-x carbon atoms
T	Absolute temperature
$T_{c,o}$	Glass crystallization onset temperature
T_g	Glass transition temperature
η	Asymmetry parameter



Abstract

The present work introduces a detailed study related to the synthesis of novel silicon oxycarbide based glasses and glass-ceramics as well as their *in vitro* bioactivity, *i.e.*, their ability to induce surface mineralization of hydroxyapatite upon exposure to simulated body fluid (SBF). The focus of the work was to rationalize the correlations between the structural features of the prepared silicon oxycarbide based materials and their bioactivity. Thus, the effect of the glass network architecture, of secondary phases as well as of the specific surface area and porosity on the bioactivity of silicon oxycarbide was investigated. This was achieved upon modification of the silicon oxycarbide glass network with additional elements, *i.e.*, B, Ca, Sr, which were shown to affect both the glass network architecture and the phase composition of the prepared silicon oxycarbides. Moreover, the specific surface area of the prepared materials was modulated upon adjusting their synthetic procedure, as shown exemplarily in the present work for Ca-modified silicon oxycarbide glasses.

The incorporation of additional B, Ca and/or Sr elements into silicon oxycarbide modified its microstructure in three different ways: (i) by forming minor soluble secondary calcium silicate and/or strontium silicate phases as for Ca and Sr modification, (ii) by introducing Q³ units (silicon tetrahedra with one non-bridging-oxygen) into silicon oxycarbide amorphous network as for Ca modification and (iii) by reducing network carbon content as for B modification. The dissolution of crystalline silicate phases during bioactivity assessment of prepared silicon oxycarbide materials in SBF solution resulted in increased Si release, which was beneficial for apatite formation. On the other hand, both the formation of Q³ units and the decrease of carbon content in the glassy network decreased its network connectivity (NC). The less connected network architecture was responsible for the improved bioactivity of the investigated silicon oxycarbide materials. Furthermore, the slight network depolymerization effect upon Q³ formation was found to have a higher influence on the silicon oxycarbide bioactivity than network carbon content. Thus, slight network depolymerization in silicon oxycarbide based glasses is sufficient to achieve high bioactivity.

The specific surface area and the porosity of silicon oxycarbide were modulated in a case study on sol-gel based Ca-modified silicon oxycarbide glasses. Thereafter, the introduction of Ca into the oxycarbide glass was shown to have significant effects on the structural features of the prepared xerogels as well as the resulting Ca-containing silicon oxycarbide glasses. Moderate content of Ca modifier was shown

to generate mesoporosity in the xerogel and stabilize it against collapse; while higher content resulted in a significantly reduced surface area and porosity in the xerogel. Moreover, two main effects were observed in the resulting oxycarbide glasses: (i) moderate Ca content led to high surface area and amorphous glasses and (ii) high Ca content induced the formation of calcium silicate secondary phase. It was shown in this case study that high specific surface area, which was provided by relatively large fractions of mesoporosity, is highly beneficial for achieving high bioactivity.

Zusammenfassung

In der vorliegenden Arbeit wird eine detaillierte Studie vorgestellt, die sich mit der Synthese neuartiger Siliziumoxycarbid-basierter Gläser und Glaskeramiken sowie mit ihrer *in vitro* Bioaktivität befasst, d. h. mit ihrer Fähigkeit, eine Oberflächenmineralisierung von Hydroxylapatit bei ihrer Aussetzung in simulierter Körperflüssigkeit (SBF) zu induzieren. Der Schwerpunkt der Arbeit lag daran, die Korrelationen zwischen den Strukturmerkmalen der hergestellten Siliziumoxycarbid-basierten Materialien und ihrer Bioaktivität zu rationalisieren. Dementsprechend wurde der Einfluss der Glasnetzwerkarchitektur, der Sekundärphasen sowie der spezifischen Oberfläche und Porosität auf die Bioaktivität von Siliziumoxycarbid untersucht. Dies wurde erreicht durch Modifikation des Siliziumoxycarbid-Glasnetzwerks mit zusätzlichen Elementen, d. h. B, Ca, Sr. Es wurde gezeigt, dass sie sowohl die Glasnetzwerkarchitektur als auch die Phasenzusammensetzung der hergestellten Siliziumoxycarbid-basierten Materialien beeinflussten. Darüber hinaus wurde die spezifische Oberfläche der hergestellten Materialien durch das Einstellen ihres Syntheseverfahrens moduliert, wie dies beispielhaft in der vorliegenden Arbeit für Ca-modifizierte Siliziumoxycarbid-Gläser gezeigt wurde.

Der Einbau zusätzlicher B, Ca und / oder Sr Elemente in Siliziumoxycarbid modifizierte seine Mikrostruktur auf drei verschiedene Arten: (i) durch Bildung von geringfügigen löslichen sekundären Kalziumsilikat- und / oder Strontiumsilikat-Phasen wie bei der Ca- und Sr-Modifikation, (ii) durch Einführen von Q³-Einheiten (Siliziumtetraeder mit einem nicht-brückenden-Sauerstoff) in das amorphe Siliziumoxycarbid-Netzwerk wie bei der Ca-Modifikation und (iii) durch Verringern des Netzwerkkohlenstoffgehalts wie bei der B-Modifikation. Die Auflösung kristalliner Silikat-Phasen während der Bioaktivitätsauswertung von hergestellten Siliziumoxycarbid-Materialien in SBF-Lösung führte zu einer erhöhten Si-Freisetzung, die für die Apatit-Bildung von Vorteil war. Andererseits verringerten sowohl die Bildung von Q³-Einheiten als auch die Abnahme des Kohlenstoffgehalts im glasartigen Netzwerk die Netzwerkkonnektivität (NC). Die weniger vernetzte Netzwerkarchitektur war für die verbesserte Bioaktivität der untersuchten Siliziumoxycarbid-Materialien verantwortlich. Darüber hinaus wurde festgestellt, dass die leichte Netzwerk-Depolymerisation bei der Q³-Bildung einen höheren Einfluss auf die Bioaktivität von Siliziumoxycarbid als der Netzwerkkohlenstoffgehalt hatte. Eine leichte Depolymerisation des Glasnetzwerks von Siliziumoxycarbid ist daher ausreichend, um eine hohe Bioaktivität zu erzielen.

Die spezifische Oberfläche und die Porosität von Siliziumoxycarbid wurden in einer Fallstudie an Sol-Gel abgeleiteten Ca-modifizierten Siliziumoxycarbid-Gläsern moduliert. Demnach wurde es gezeigt, dass die Einführung von Ca in das Oxycarbid-Glas bedeutende Auswirkungen auf die Strukturmerkmale der hergestellten Xerogele sowie der sich daraus ergebenden Ca-haltigen Siliziumoxycarbid-Gläser hatte. Es wurde gezeigt, dass ein mäßiger Gehalt an Ca-Modifikator Mesoporosität im Xerogel erzeugte und sie gegen Kollaps stabilisierte; während ein höherer Gehalt zu deutlich verringerter Oberfläche und Porosität im Xerogel führte. Darüber hinaus wurden bei den resultierenden Oxycarbid-Gläsern zwei Haupteffekte beobachtet: (i) ein mäßiger Ca-Gehalt führte zu einer hohen Oberfläche und amorphen Gläsern und (ii) ein hoher Ca-Gehalt induzierte die Bildung der Kalziumsilikat-Sekundärphase. In dieser Fallstudie wurde gezeigt, dass eine hohe spezifische Oberfläche, die durch relativ große Anteile an Mesoporosität bereitgestellt wurde, für eine verbesserte Bioaktivität von großem Vorteil ist.

1. Scope and Motivation

The clinical treatment of critical size bone defects requires the usage of bioactive materials to trigger or accelerate natural bone healing process [1]. Bioactive glasses have been important bone grafting materials since the discovery of Bioglass® 45S5 (45 wt.% SiO₂, 24.5 wt.% CaO, 24.5 wt.% Na₂O and 6.0 wt.% P₂O₅) by LL Hench [2]. The ability of bioactive glasses to induce hydroxyapatite (bone mineral) formation during contact with physiological fluids provides a high bone-bonding ability [3]. Furthermore, leaching products from bioactive glasses have effects on promoting osteogenesis and angiogenesis, enhancing new bone formation [4]. The high bioactivity of bioactive glasses is correlated to their weak network structure, allowing fast glass dissolution in physiological fluids. The weakening of glass network is realized by incorporating high content of network modifiers, *i.e.*, alkali or alkaline earth metal ions, in glass compositions.

However, some drawbacks related to high alkali content in bioactive glasses have been reported. On one hand, the fast dissolution of alkali ions leads to high pH environment, which may be cytotoxic [5]. On the other hand, weak network structure leads to low mechanical strength and a high crystallization tendency of bioactive glasses. The fabrication of 3D scaffold from bioactive glasses is thus difficult, since the partial glass crystallization at processing temperature can lead to mechanical instability [6, 7]. Moreover, the degradation of bioactive glasses is too fast, and not able to match slower new bone formation [8].

Correspondingly, significant work has been done, in order to solve the issues of alkali-containing bioactive glasses. Alkali-free bioactive glasses have been developed by replacing alkali metals with alkaline earth metals [9, 10]. Bioactive glasses with relatively large processing window has been achieved by optimizing glass composition [11, 12]. Bioactive ceramics, such as calcium silicate, tricalcium phosphate and synthetic hydroxyapatite, have shown high bone-bonding ability and low ceramic degradation in human body fluid [13, 14]. Furthermore, composite materials, such as glass-ceramic or glass-polymer composites, have shown mechanical properties that can fulfill clinical requirements [3, 12, 15]. In general, these research works are based on the optimization of original Bioglass® 45S5 composition or on the modification of well-known bioceramics.

In the present work, a new generation of alkali-free bioactive materials based on amorphous silicon oxycarbide will be investigated. Clinical application requires high biocompatibility, high mechanical

strength, high processability and tunable bioactivity of bioactive materials. Silicon oxycarbide is a promising candidate to fulfill these requirements: (i) the mix-bonded structure of Si-O and Si-C in silicon oxycarbide provides higher intrinsic mechanical strength than that of vitreous silica; (ii) the synthesis of silicon oxycarbide via so-called polymer derived ceramic method makes it possible to apply polymer forming techniques for fabricating silicon oxycarbide implants; (iii) the carbon incorporation in silicon oxycarbide creates unique oxycarbide matrix / "free carbon" nano-domain structure, which shows high temperature crystallization resistance that is beneficial for the thermal processing of the materials [16]; (iv) the modification of silicon oxycarbide with metal elements has been investigated extensively [17], and the incorporation of therapeutic metal ions in silicon oxycarbide can be easily realized.

Until now, the high biocompatibility, *i.e.*, non-cytotoxicity, of silicon oxycarbide has been confirmed in several studies [18, 19]. Preliminary research work has proven the ability of silicon oxycarbide to show bioactivity, *i.e.*, apatite forming ability, in simulated body fluid [20, 21]. However, a systematic investigation on the structure-property correlation for bioactive silicon oxycarbide materials still needs to be done.

For this purpose, two approaches have been applied in the present study. Firstly, the network architecture and phase composition of silicon oxycarbide will be modified by incorporating alkaline earth metals (Ca and Sr) and an additional network former (B). Secondly, the porosity of silicon oxycarbide will be varied via sol-gel process. The correlation between these structural features and observed bioactivity upon SBF assessment will be discussed.

2. Fundamentals and State of the Art

2.1. Silicon oxycarbide

The use of silicon oxycarbide as a material name can be traced back to the begin of 20th century, where silicon oxycarbide was referred to a carbon-silica mixture for high-temperature insulating applications [22]. Since the 1990s, the term of silicon oxycarbide has been restricted to materials, which contains not only carbon in elementary form (sp^2 carbon), but also network carbon (sp^3 carbon) [23]. Thus, the coexisting of Si-C and Si-O covalent bonds is characteristic for silicon oxycarbide.

Due to the high temperature carbothermal reaction between silica and carbon and the extremely low solubility of carbon in silicon oxide, silicon oxycarbide is difficult to be synthesized via conventional solid state reaction from inorganic sources [24, 25]. The possibility to incorporate carbon into silica network, as in the case of silicon oxycarbide, has been essentially limited to several methods, namely chemical vapor deposition (CVD), radio frequency (RF) magnetron sputtering, polymer derived ceramic (PDC). In CVD method, organic small-molecular Si species, such as siloxanes and carbosilanes, are deposited on substrates to form silicon oxycarbide thin films under energy input (*i.e.*, laser, heat etc.) [26, 27]. In typical RF magnetron sputtering, SiC ceramic target is sputtered in Ar/O₂ gas flow to synthesize amorphous silicon oxycarbide thin films or coatings [28, 29]. In PDC method, organic Si-containing monomers or oligomers, such as siloxanes and silsesquioxane, are crosslinked to polymer chains or networks, which then undergo thermal decomposition under non-oxidative gas atmosphere (*i.e.*, Ar or N₂). The lack of oxidation reaction during the thermolysis preserves the Si-C/Si-O bonds, that already exist in polymer structure, in obtained silicon oxycarbide [30, 31]. Compared to the high complexity and cost of CVD and RF magnetron sputtering processes, PDC method prevails thanks to its similarity to a conventional ceramic calcination / sintering process. Besides, the possibility to apply polymer forming techniques to polymer precursors in PDC method allows to achieve different material forms for silicon oxycarbide, ranging from coatings, monoliths to porous structures [32].

Tetravalent sp^3 hybridized network carbon in silicon oxycarbide leads to more connected network structure, which is shown to improve its mechanical properties compared to vitreous silica [33, 34]. Silicon oxycarbide is also a high temperature material and has outstanding oxidation resistance [35]. Furthermore, silicon oxycarbide shows high temperature crystallization resistance [36]. Recently, the functional properties of silicon oxycarbide, such as electrical properties, optical properties and bioactivity, have

gained increasing attentions [32]. By varying the O:C atomic ratio or introducing additional elements into silicon oxycarbide, its properties can be adjusted.

2.1.1. Polymer derived ceramic method

In polymer derived ceramic (PDC) method, various Si-based ceramics are achievable by the thermolysis of Si-containing organic polymers in inert gas atmosphere [31, 37, 38]. Figure 2-1 summarizes the polymer precursors for PDC process. Thereafter, PDC method can be utilized for synthesizing silicon carbide (SiC), silicon oxycarbide (SiOC) and silicon carbonitride (SiCN). For silicon oxycarbide, polysiloxane and polysilsesquioxane are widely used precursors [39, 40].

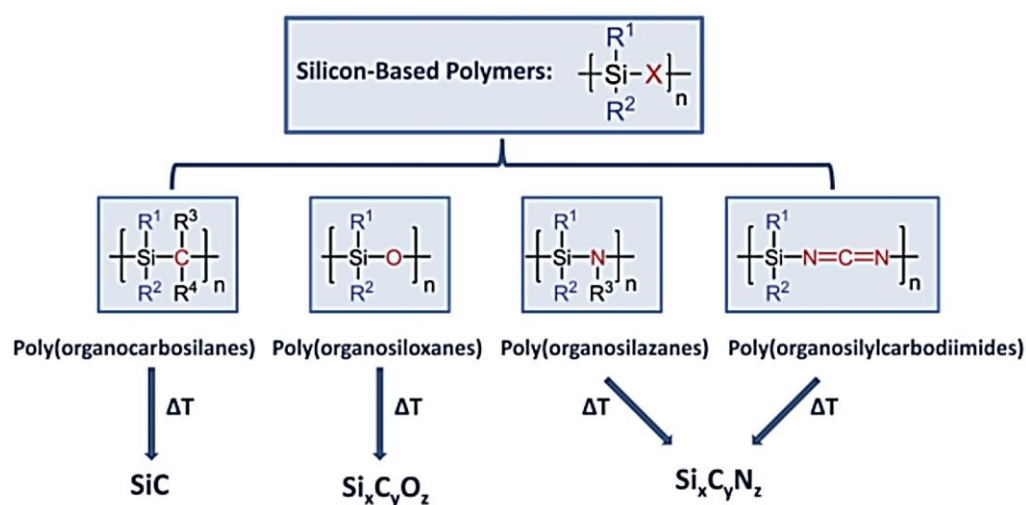
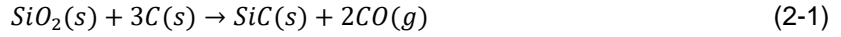


Figure 2-1. Thermal decomposition of Si-based polymers and their corresponding ceramic products [38].

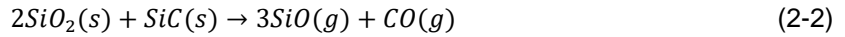
The polymer-to-ceramic transformation during the thermolysis undergoes several stages. At low temperatures (100-400 °C), functional groups, such as ethoxy groups of the polymer precursors, crosslink to increase the molecular mass of polymer chain, reducing the mass loss related to molecule evaporation [32, 37]. From 400 to 800 °C, the rearrangement of polymer molecules and the decompositions of organic groups occur accompanied by gas evolution of small molecules, such as CH₄ and C₂H₄ [41, 42]. From 800 to 1000 °C, hydrogen content is still detectable in the derived ceramics and decreases continuously with increasing temperature [43-45]. After thermolysis at 1000 °C, the hydrogen in PDC-derived silicon oxycarbide is removed extensively [46]. 1000 °C is thus considered generally as the temperature, at which the polymer-to-ceramic transformation completes [32, 37].

The decomposition of carbon-containing organic groups leads to segregated carbon formation, *i.e.*, so-called “free carbon”. The content of “free carbon” in PDC-derived silicon oxycarbide is dependent on the

carbon content in its polymer precursor [47, 48]. At temperatures higher than 1200 °C, phase separation into SiC nanocrystalline and amorphous SiO₂ occurs, followed by carbothermal reaction between formed SiO₂ and “free carbon” according to equation (2-1) [16, 49]:



The ongoing carbothermal reaction leads to the decrease of “free carbon” content. Thus, at higher temperatures (> 1400 °C) direct reactions (equation (2-2) [50]) between SiO₂ and formed SiC is preferred, leading to gas evolution and a complete decomposition of silicon oxycarbide.



2.1.2. Structure of silicon oxycarbide

Silicon oxycarbide contains corner-linked SiO_xC_{4-x} (x can be chosen from 0-4) building units [32]. NMR investigation of silicon oxycarbide shows no direct C-O bond, thus carbon can only bond to silicon or carbon itself [33]. In Figure 2-2 (a) a typical ²⁹Si NMR spectrum of PDC-derived silicon oxycarbide can be deconvoluted into different SiO_xC_{4-x} building units. A quantitative assessment of the SiO_xC_{4-x} fractions via integration of the deconvoluted components exhibits significant deviation from the fractions calculated based on a statistically random distribution of Si-C and Si-O bonds [51]. Therefore, a concentration of SiO_xC_{4-x} units to carbon-rich SiC₄ and oxygen-rich SiO₄ units in silicon oxycarbide is confirmed [51]. Besides, the existence of “free carbon” (see Figure 2-2 (b)) is confirmed in various Raman investigations [40, 52]. In summary, silicon oxycarbide has an inhomogeneous microstructure, in which carbon-rich, oxygen-rich SiO_xC_{4-x} and “free carbon” domains coexist.

Silicon oxycarbide is X-ray amorphous up to ca. 1300 °C [37, 50]. However, small-angle X-ray scattering (SAXS) investigation discovers a nano-domain structure with domain size of 1-3 nm in silicon oxycarbide [36], corresponding to the NMR and Raman investigations discussed above. At temperatures higher than 1300 °C, phase separation and carbothermal reaction in silicon oxycarbide lead to the observation of β-silicon carbide crystallization [49, 50]. The crystallization of amorphous SiO₂ to cristobalite can occur at even higher temperatures (> 1500 °C) or after extra heat treatment [53]. The high crystallization resistance for amorphous silica in silicon oxycarbide is related to residual Si-C bonds, “free carbon” in the

silica domains or formed fine phase separated nanostructure that prevent the nucleation of cristobalite [16, 49].

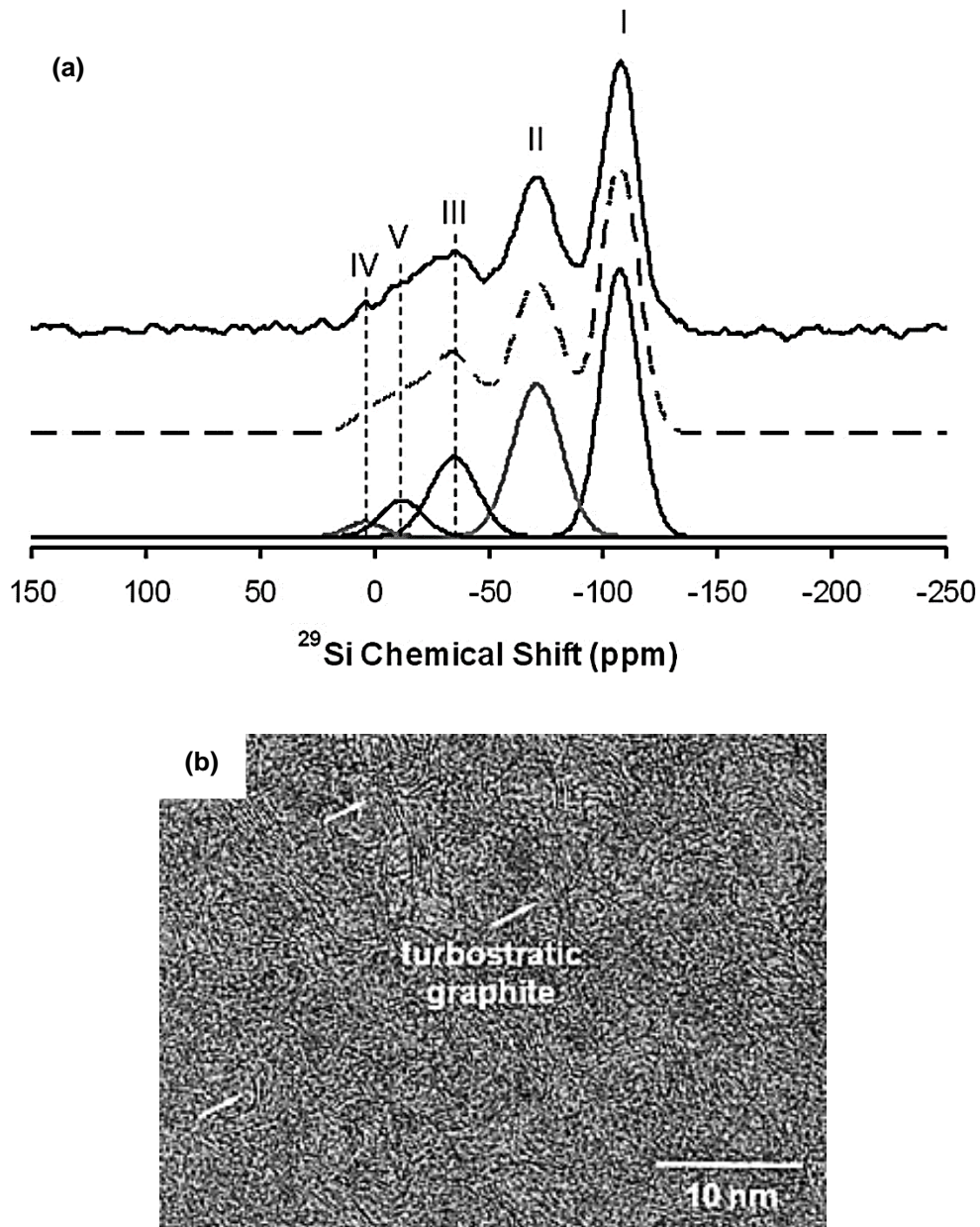


Figure 2-2. (a) Typical ^{29}Si MAS NMR spectrum of polysiloxane derived silicon oxycarbide (solid bold line) with the simulated spectrum (dashed line) and individual simulation components (thin solid lines). The peaks (I, II, III, IV and V) correspond to SiO_4 , SiO_3C , SiO_2C_2 , SiOC_3 and SiC_4 units, respectively [51]; (b) TEM micrograph of a C-rich silicon oxycarbide sample synthesized at 1400 °C [54].

Two models have been developed for the nano-domain structure in silicon oxycarbide. As shown in Figure 2-3 (a), Widgeon *et al.* [51] consider oxygen-rich $\text{SiO}_x\text{C}_{4-x}$ regions to build a continuous matrix and “free carbon” particles are dispersed inside this matrix; in Figure 2-3 (b), Saha *et al.* [36] consider “free carbon” sheets or layers to build continuous cage walls that divide oxygen-rich $\text{SiO}_x\text{C}_{4-x}$ regions (silica domains). In both models, carbon-rich $\text{SiO}_x\text{C}_{4-x}$ regions sit between oxygen-rich $\text{SiO}_x\text{C}_{4-x}$ and “free carbon” regions. The Widgeon’s model is supported by mass fractal analysis of oxygen-rich $\text{SiO}_x\text{C}_{4-x}$ domains in silicon oxycarbide [51]; while the Saha’s model is based on the assumption that high creep resistance in silicon oxycarbide is related to a continuous “free carbon” network [36]. However, recent research results correlate the high creep resistance in silicon oxycarbide to domain-interfaces but not to the morphology of “free carbon” [34]. The low percolation threshold (*i.e.*, 5 vol %) for “free carbon” in silicon oxycarbide is rather considered to be responsible for the formation of a continuous “free carbon” phase [55]. Thus, the microstructure of silicon oxycarbide should be described by a combination of these two models and both oxygen-rich $\text{SiO}_x\text{C}_{4-x}$ and “free carbon” domains are continuous.

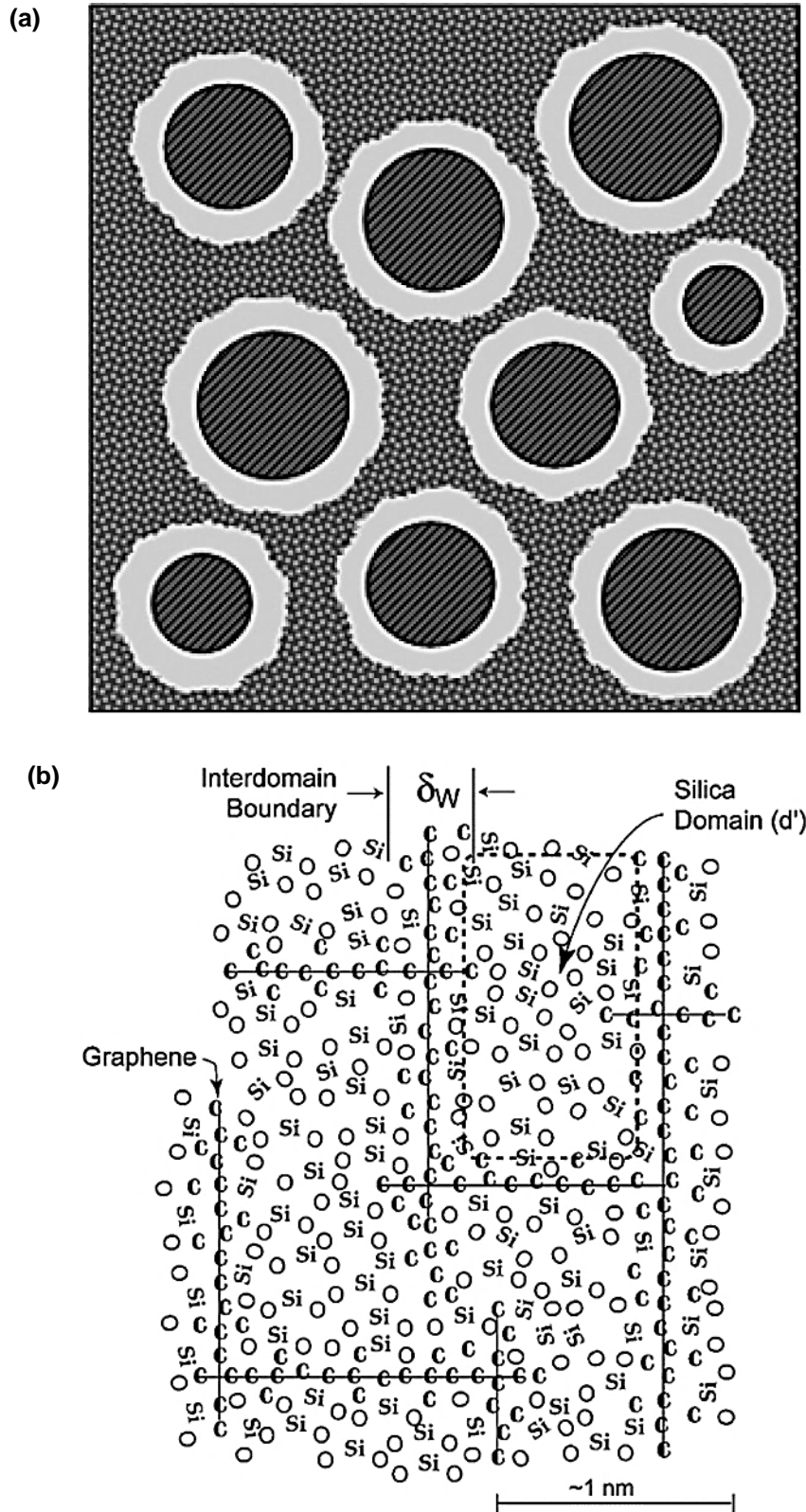


Figure 2-3. (a) Structural model of silicon oxycarbide, in which black regions represent “free carbon” and the patterned matrix is oxygen-rich silicon oxycarbide domains. Between the two regions lie the grey regions referring to carbon-rich silicon oxycarbide [51]; (b) Structural model of silicon oxycarbide, in which oxygen-rich silica regions are separated by “free carbon” sheets [36].

2.1.3. Modification of silicon oxycarbide

Additional elements are able to be introduced to silicon oxycarbide via chemical modification of its polymer precursor. The obtained so-called “single-source-precursor”, in which the doping elements are distributed homogeneously on a molecular level, is converted subsequently to silicon oxycarbide via PDC process [32, 37].

Non-metallic elements, such as N and B, are incorporated into silicon oxycarbide network by forming covalent bonds. It has been reported that N forms N-C and N-Si bonds, and N-modification tunes the high temperature oxidation, crystallization and decomposition behavior of silicon oxycarbide [56-58]. B modification, forming B-C and B-O bonds in silicon oxycarbide, has been found to improve the “free carbon” ordering and β -SiC crystallization at high temperatures in silicon oxycarbide [59, 60].

Metallic elements, such as transition metals, tend to form *in situ* secondary phases in silicon oxycarbide, resulting in silicon oxycarbide based nanocomposites [37]. A systematic analysis by Ionescu *et al.* [17] implies an underlying thermodynamic control behind the formation of secondary phases. By considering high temperature carbothermal reaction, the formed metal-containing secondary phases can be predicted. Figure 2-4 shows that metals that are stable against carbothermal reaction tend to form oxide and silicate phases; while metals that are unstable against carbothermal reaction tend to form metallic, metal silicide and metal carbide phases. Correspondingly, metal modified silicon oxycarbide combines the intrinsic properties of silicon oxycarbide matrix with functional properties of dispersed secondary phases. For example, Hf or Zr forms oxide phases in silicon oxycarbide, which have an effect on improving high temperature stability [61, 62]; Sn forms metallic Sn phase in silicon oxycarbide and lends thus Si(Sn)OC material the property to uptake / release Li reversibly [63]; Fe forms iron silicide phases in silicon oxycarbide, leading to soft magnetic properties of Si(Fe)OC [64].

2.2. Biomaterials and bioactive glasses

Biomaterial is defined as “material intended to interface with biological systems to evaluate, treat, augment or replace any tissue, organ or function of the body” [67]. Metals, polymers, ceramics and composites based biomaterials have found applications in surgery practice, for example, as implants or in medical devices [68]. The key criterion for biomaterials is their biocompatibility with host tissues in human body. Biocompatibility means that biomaterials are not cytotoxic and will not reduce cell viability [69]. Good biocompatibility can be achieved with materials that are chemically or physiologically inert such as Pt, Ti and Al_2O_3 [68, 70, 71]. The lack of corrosion and degradation of these materials in human body avoids possible cytotoxicity induced by degradation products and the change of physiochemical conditions at the host sites.

On the other hand, the need for biodegradable or bioresorbable materials, such as biopolymers or hydrogels, is increasing, since new therapeutic solutions, such as temporary implant or drug delivery medium, require materials that function by reacting with host tissues and disappear after fulfilling their purposes [72]. Moreover, the disappearance of these materials after use eliminates the potential cytotoxicity of inert materials, which could take place due to material failure after a long-term service [69]. It is known, that biocompatibility of biodegradable materials depends strongly on their degradation mechanisms and the specific host responses during the degradation [69, 73, 74]. By adjusting the molecular structure of biodegradable materials, their biocompatibility can be tuned [75, 76].

Bioactive or bioreactive materials show bioactivity, which is defined as “phenomenon by which a bio-material elicits or modulates biological activity” [67]. Since the discovery of Bioglass® 45S5 by LL Hench [2], the research of bioactive glasses is focused on bone repair application. Therefore, bioactivity of bioactive glasses is defined as the ability to trigger hydroxyapatite ($\text{Ca}_5(\text{PO}_4)_3\text{OH}$) (HA) formation on material surface upon contact with human body fluid. Since HA is a bone mineral, the HA formation is correlated to a high bone-bonding ability [77, 78].

2.2.1. Classification and mechanism of bioactivity

Hench *et al.* [2] define two bioactivity classes: class B bioactivity induces osteoconduction, referring to bone formation along material surface; class A bioactivity induces both osteoproduction and osteoconduction. Osteoproduction refers to bone formation away from material surface, induced by the activation of osteoprogenitor cells to differentiate into osteoblast cells [2, 78]. This activation has been correlated to the release of Si and Ca from bioactive glasses, which triggers genetic cellular responses [79, 80]. Typical class A bioactive materials are bioactive glasses, while typical class B bioactive materials are bioactive ceramics, such as synthetic hydroxyapatite or tricalcium phosphate [81]. Due to the intracellular genetic activation, bioactive glasses have shown better bone regeneration effects than bioactive ceramics in *in vivo* studies [82, 83].

According to Hench *et al.* [78, 81], the mechanism of bioactivity for bioactive glasses can be described in following steps:

- i. Ion exchange between glass network modifiers (Ca^{2+} , Na^+ , *etc.*) and protons in body fluids leads to formation of surface silanol (Si-OH) groups;
- ii. The increase of local pH value due to ion exchange results in further hydrolysis of silica network and release of silicic acid (Si(OH)_4) into body fluids;
- iii. Surface silanol groups condensate to form amorphous silica-gel surface layer, which is depleted of network modifiers;
- iv. Migration of Ca^{2+} and PO_4^{3-} onto silica-gel layer, accompanied by ongoing glass dissolution, leads to formation of amorphous calcium phosphate;
- v. Surface calcium phosphate takes up OH^- and CO_3^{2-} from body fluids, leading to formation of crystalline carbonated hydroxyapatite (HCA);
- vi. Adsorption and attachment of growth factors and stem cells (osteoprogenitor cell) to HCA layer. Further cell differentiation and proliferation result in new bone formation.

Despite some critical arguments against the equalization of hydroxyapatite forming ability with bioactivity [84], the use of hydroxyapatite forming ability to compare the bioactivity of biomaterials has been established [85-87]. Since the development and standardization of simulated body fluid (SBF) by Kokubo *et al.* [88], *in vitro* assessment in SBF solution has become a routine method to evaluate bioactivity of biomaterials [89, 90]. SBF solution has nearly the same ion concentrations as human blood plasma.

The evaluation of apatite forming ability of biomaterials in SBF solution can be used to predict their bioactivity *in vivo* [91, 92].

Whether a silicate glass shows bioactivity, depends on its chemical composition. Hench *et al.* [13] investigated the bioactivity of $\text{SiO}_2\text{-CaO-Na}_2\text{O}$ glass system by varying its chemical composition. As shown in Figure 2-6, 60 mol% has been found to be an upper limit for SiO_2 content, in order to achieve bioactivity for melt-derived glasses [93]. The increase of alkali and alkaline earth metal content leads to fast glass dissolution and thus high bioactivity [94]. However, although alkali ions (*i.e.*, Na) can improve apatite forming ability, they can also lead to high pH environment, which has caused certain cytotoxicity in *in vivo* studies [10, 95, 96]. Thus, the research on bioactive alkali-free glasses has been intensified. High bioactivity can be achieved for alkali-free glasses by tuning their glass network structure [9, 95, 97, 98].

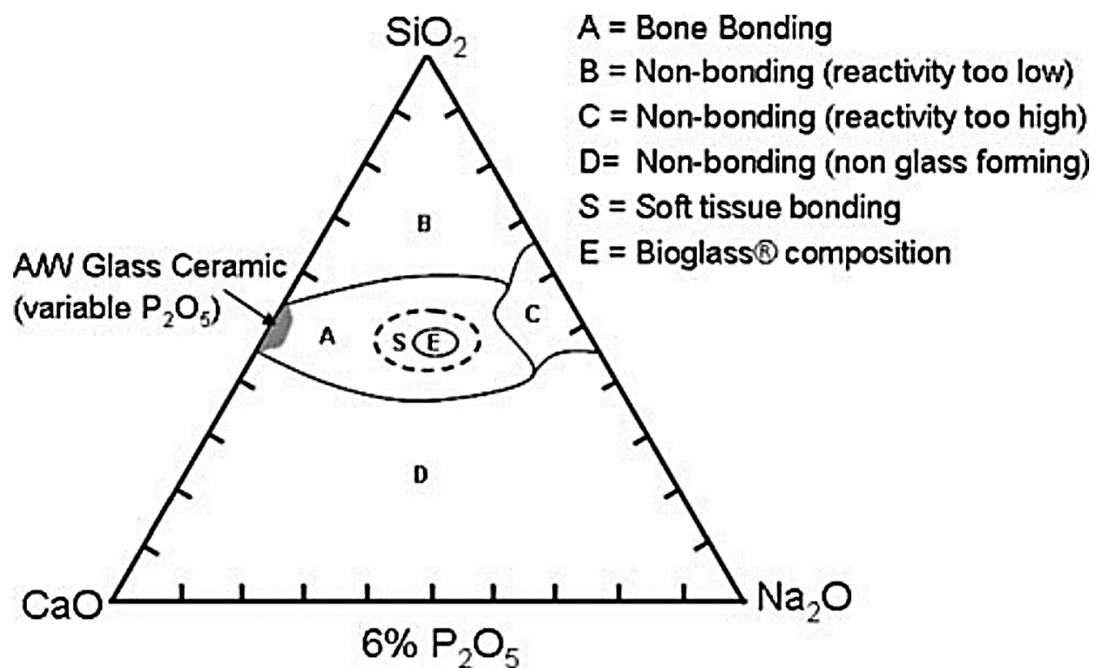


Figure 2-6. Kinetically determined boundaries for $\text{SiO}_2\text{-CaO-Na}_2\text{O}$ glasses (with 6 wt.% P_2O_5). Depending on glass compositions, different bone-bonding behaviors (bioactivity) are to be expected [2].

Solid state NMR study of glass network structure shows a correlation between bioactivity and open network structure in bioactive glasses [3, 94]. By incorporating network modifiers such as Ca^{2+} and Na^+ cations into silica network, the corner-connected SiO_4 tetrahedra network is depolymerized. The breaking of parts of the Si-O covalent bonds is necessary in order to electrostatically balance the positive charges of the incorporated metal cations [99, 100]. The subsequent distribution of non-bridging-

oxygens (NBO) in glass network results in Q^n units, in which n is the number of bridging-oxygen on a network former atom and ranges from 0 to 4 for SiO_4 tetrahedra [101]. Both Si and P are network formers in SiO_2 - P_2O_5 bioactive glasses. However, P forms orthophosphate units (PO_4^{3-}) at low content and has thus only Q^0 units for 45S5 based bioactive glasses. Therefore, glass network connectivity (NC) is defined as the average number of covalent bonds (e.g., bridging oxygen) on a Si tetrahedron and can be represented by the average n value for Si Q^n units calculated by glass compositions according to equation (2-3) [101]:

$$NC = \frac{4[SiO_2] - 2[M_2^I O + M^{II} O] + 6[P_2O_5]}{[SiO_2]} \quad (2-3)$$

where M^I and M^{II} are alkali and alkaline earth metals, respectively; $[SiO_2]$, $[M_2^I O]$, $[M^{II} O]$ and $[P_2O_5]$ represent their corresponding molar fractions. A direct evaluation of NC can also be done by applying Q^n molar fractions calculated from ^{29}Si NMR analysis according to equation (2-4):

$$NC = \sum_{n=0}^4 n [Q^n] \quad (2-4)$$

where $[Q^n]$ refers to the molar fraction of Q^n unit. Obviously, NC has a maximal value of 4 for quartz glass. The lower the NC value is, the more loosely the silica network is connected. Bioactive glasses have typical NC values between 2.0 and 2.6 [102]. At NC of ca. 2.0, Q^2 units dominate glass network and build SiO_4 tetrahedra rings that can be leached easily to aqueous solution, which is responsible for high bioactivity [100, 103]. The increase of SiO_2 content increases network connectivity (see equation (2-3)), suppressing thus glass dissolution. In contrary, the increase of phosphorus content to a certain extent increases the content of easily soluble Q^0 orthophosphate units, which are beneficial for enhancing bioactivity [101, 103]. Therefore, alkali-free bioactive glasses are achievable by replacing alkali ions with alkaline earth ions and in the meantime the network connectivity should be kept around 2.0.

On the other hand, bioactivity is kinetically dependent since ion exchange occurs at the interface between solid and liquid. Therefore, bioactivity is influenced by specific surface area (SSA) of the materials. Traditional melt-derived silicate glasses have specific surface area valued under $3 \text{ m}^2/\text{g}$, while sol-gel derived silicate glasses can reach specific surface area as high as $400 \text{ m}^2/\text{g}$ [89, 104, 105]. The increase of specific surface area enhances the bioactivity of silicate glasses and extends their composition range to show bioactivity. Sol-gel derived glasses with SiO_2 content as high as 90 mol% can be highly bioactive [106, 107].

2.2.2. Therapeutic effects of released ions

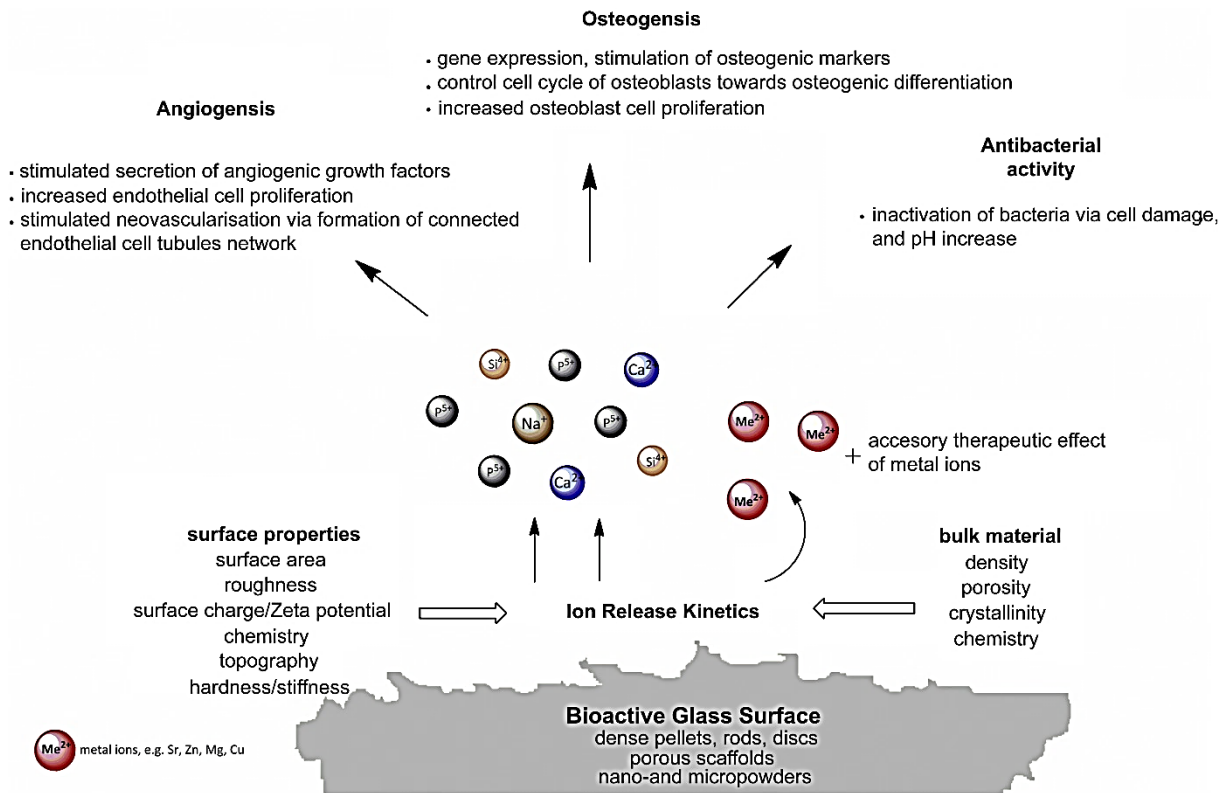


Figure 2-7. Summary of therapeutic effects of released ions from bioactive glasses [4].

The process for new bone regeneration requires not only apatite forming ability, but also beneficial cellular activation for bioactive materials [2, 84]. The dissolution products of bioactive glasses, *i.e.*, released ions, play a crucial role on the cellular activation process and can tune angiogenesis, osteogenesis and antibacterial activity at host tissues, as summarized by Hoppe *et al.* (see Figure 2-7) [4].

The release of Si and Ca in appropriate rates can enhance osteogenesis. Si release has been reported to favor osteoprogenitor cell differentiation, osteoblast-like cell proliferation, collagen-I expression and formation of extracellular matrix [108, 109]. Thus, Si-substituted hydroxyapatite has shown higher bioactivity than pure hydroxyapatite [110, 111]. Furthermore, Ca in extracellular environment improves the osteogenic differentiation of human dental pulp cells and human mesenchymal stromal cells, enhancing matrix mineralization [112, 113]. Meanwhile, the increase of intracellular Ca concentration suppresses bone resorption activity of osteoclasts [114]. As mentioned before, the class A bioactivity of Bioglass® is correlated to the osteogenic effects of released Si and Ca [2].

Mg has been reported to play a critical role in bone remodeling and skeletal tissue development, and can improve bone calcification and the attachment of osteoblast cell on biomaterial [115]. The increase

of Mg content in bioactive glasses can lower glass dissolution and thus apatite forming ability, since Mg is a network intermediate and can act as both network former and network modifier. Furthermore, Mg can enhance osteoblast cell proliferation [116]. The proliferation and differentiation of bone resorbing osteoclast cells may be suppressed at high Mg concentration [117].

Sr substitution in bioactive materials is a promising approach for treating osteoporosis disease [118]. By simultaneously enhancing metabolic activity of osteoblast cells (bone forming) and inhibiting that of osteoclast cells (bone resorbing) upon Sr^{2+} release, bone density can be enhanced [119, 120]. Moreover, *in vivo* studies of bioactive Sr-containing glasses or glass-ceramics confirm their high bone-bonding ability (osseointegration) [121, 122].

Surgery- and biomaterial-associated infections are due to the attachment of bacteria and the subsequent biofilm formation, which are difficult to be treated [123, 124]. ZnO nanoparticles show antibacterial activity against various microorganisms. The mechanisms of such antibacterial properties are related to the disruption of cell membranes, production of reactive oxygen species, nanoparticle internalization into cells [125-127]. Meanwhile, the antibacterial effect upon Zn^{2+} release has been observed for Zn/ZnO-containing bioactive glass systems [128-130].

Angiogenesis, namely the revascularization process during new bone formation, is indispensable for bone tissue engineering [131]. The formation of blood vascular network allows the supply of oxygen, nutrients and growth factors to bone regeneration sites [132, 133]. Borate dissolution from boron-containing bioactive glasses can stimulate the expression and secretion of vascular endothelial growth factor and improve thus angiogenesis [132, 134]. However, the concentration of released B plays an important role on cell viability. At high B concentration, cytotoxicity can occur [134]. A suitable B concentration is achievable by controlling boron release kinetics [135].

In summary, ion release from bioactive glasses has diverse effects on cellular activity. At controlled release rate and thus suitable ion concentration, beneficial cellular responses for bone regeneration can be expected. Thus, composition design of bioactive glasses should not only target apatite forming ability, but also tailored ion release kinetics.

2.2.3. Processing of bioactive glasses

Bioactive glasses have high tendency to crystallize during thermal treatment due to their high content of alkali and alkaline earth metals. The processing window, namely the temperature range between glass transition temperature T_g and crystallization onset temperature $T_{c,o}$, lies between 520 °C and 652 °C for Bioglass® [11]. This narrow processing window brings difficulties for processing Bioglass® into monolith or scaffolds, since partial crystallization leads to local mechanical instability [78]. Although the formed crystalline phases, *i.e.*, $\text{Na}_2\text{CaSi}_2\text{O}_6$ and $\text{Na}_2\text{Ca}_2\text{Si}_3\text{O}_9$ depending on processing temperature [136, 137], are still able to induce apatite formation, their apatite forming ability is often lower [138, 139]. Moreover, the crystallization of bioactive glasses has been reported to inhibit protein adsorption and enforce inappropriate protein conformation for cell adhesion [140]. The efforts to enlarge the processing window in order to keep an amorphous glass nature during thermal processing are usually connected with an increase of glass network connectivity and thus lower apatite forming ability [3, 141].

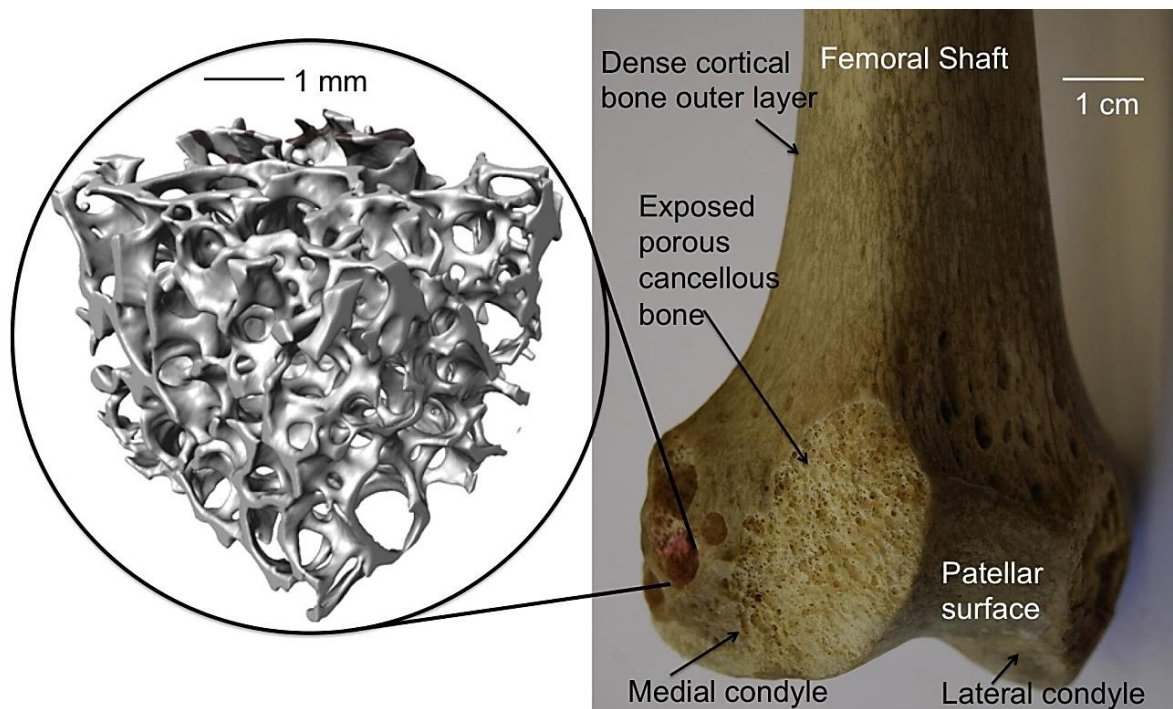


Figure 2-8. Human nature femur bone, with in the inset the 3D porous structure of the cancellous bone scanned by X-ray microtomography [3].

As shown in Figure 2-8, human cancellous bone has a highly porous structure. Thus, synthetic scaffolds with large pore size ($> 100 \mu\text{m}$) and high pore connectivity which can allow bone ingrowth and act as templates for new bone formation are highly desirable for bioactive materials [78, 142]. Typical methods for fabricating 3D scaffolds are polymer template, foaming, freeze-casting and additive manufacturing

methods [3, 143]. In polymer template method, polymer space holders or polymer foam templates with designed structure are used to form 3D scaffolds and removed after thermal annealing [144, 145]. In foaming process, gas bubbles induced by vigorous stirring are fixed in glass slurry via condensation reaction of the gelation additives. The bubbles are then left as pores in final scaffold [146, 147]. Freeze-casting makes use of the growth of frozen solvent crystals to achieve an interpenetrating glass-solvent 3D structure. After the removal of solvent via freeze-drying, a porous structure is achieved [148, 149]. Additive manufacturing emerges as a novel technique that is able to design the porous structure from the ground up. These methods are based on the processing of glass powder or slurry. Thus, the remaining glass particles after processing need to be sintered through a following thermal stabilization / densification step.

In order to solve the crystallization problem of Bioglass® scaffolds during their thermal densification [150, 151], 13-93 bioactive glass (glass composition: Na₂O 6.0 wt.%, K₂O 12 wt.%, MgO 5 wt.%, CaO 20 wt.%, P₂O₅ 4 wt.% and SiO₂ 53 wt.%) has been developed [141]. 13-93 glass has a large processing window (592–932 °C) and its amorphous scaffold shows 20 times higher mechanical strength than Bioglass® scaffold fabricated in the same way [11, 12]. Meanwhile, although high mechanical strength can be achieved by designing oriented scaffold structure via freeze-casting or additive manufacturing techniques [3, 12], the intrinsic brittleness of glass and ceramic materials remains a problem for sustaining cyclic bone loading. Therefore, bioactive polymer-glass composite has become a promising solution for fabricating clinically applicable scaffolds, which show high fracture toughness compared to pure glass scaffolds [3, 6, 12].

Moreover, bioactive glasses based coatings have been developed. Bioactive glass coating has been applied on SiC ceramic via pulsed laser ablation in order to achieve a high ceramic-bone bonding [152]. Biodegradable sutures coated with Ag-containing bioactive glasses show both bioactivity and antibacterial properties and are promising for tissue engineering and wound healing applications [153, 154]. Bioactive glass coating on zirconia substrate has significantly improved bioactivity compared to uncoated zirconia substrate [155]. Furthermore, the thermal expansion coefficient of bioactive glasses can be adjusted, in order to achieve a high bonding strength between glass coating and substrate material [156-158]. Thus, the processing of bioactive glasses into coating is a promising method to combine the high bioactivity of bioactive glasses with the high mechanical properties of substrate materials.

2.3. Silicon oxycarbide for prospective biomedical applications

The unique PDC synthesis method provides a high possibility to tune material morphology, composition and microstructure of silicon oxycarbide according to the intended application [32]. Moreover, the combination of the existence of segregated “free carbon”, high crystallization resistance and high mechanical properties in silicon oxycarbide makes it a promising material to substitute silicate or carbon based materials for various biomedical applications. Although the research work on the biomedical properties of silicon oxycarbide is still limited, its prospective biomedical applications have been highlighted in some preliminary studies, as being summarized in Figure 2-9. In the following sections, the biomedical properties of silicon oxycarbide will be reviewed based on published research results and are categorized into biocompatible, bioactive or surface active properties.

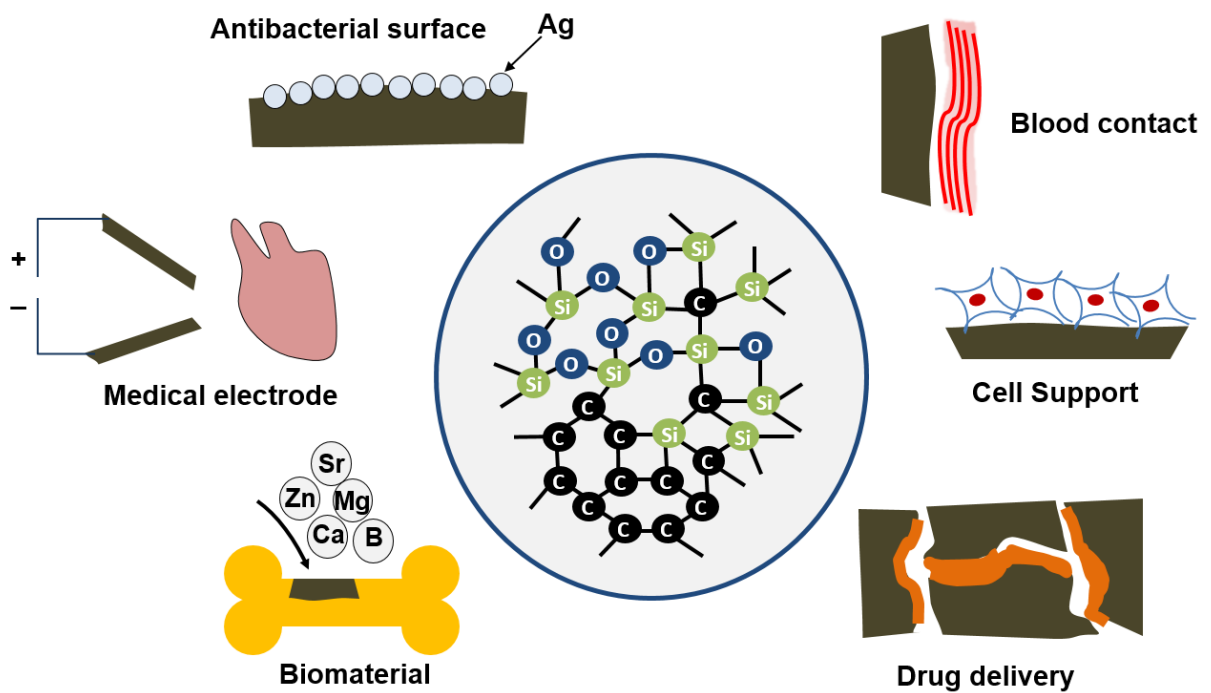


Figure 2-9. Summary of the biomedical applications of silicon oxycarbide materials in published research work.

2.3.1. Biocompatibility of silicon oxycarbide

Blood contact properties

Silicon oxycarbide is a versatile blood contact material. By incorporating carbon, the propensity of silicon oxycarbide to blood coagulation can be tuned between that of procoagulant silica and hemocompatible pyrolytic carbon. The hemocompatibility of PDC-derived silicon oxycarbides with different O and C contents has been evaluated via coagulation time in human recalcified platelet poor plasma (PPP) test, which shows a clear correlation between hemocompatibility and surface C/O atomic ratio, namely, high C/O atomic ratio can improve hemocompatibility to the level of inert silanized glass [159]. At the same time, blood contact tests on CVD-derived silicon oxycarbide nanowires with low carbon content (13.4 at.%) have shown promoted platelet activation similarly to flat silicon dioxide samples in porcine platelet rich plasma (PRP) test. Kinetic analysis of hemoglobin released from erythrocytes confirmed even stronger blood clotting formation for silicon oxycarbide nanowires than flat silicon dioxide samples [18]. Thus, despite carbon incorporation, the silicon oxycarbide nanowires do not show improved hemocompatibility, which could be related to the relatively low carbon content. However, since carbon exists in both sp^3 and sp^2 bonding states in silicon oxycarbide, a separation of these two contributions to blood contact properties still needs to be done in future research.

Properties for medical electrodes

Silicon oxycarbide is a promising material for medical electrodes in implantable pacemakers or neurostimulators, in which electrical stimulation is used to treat cardiac or cortical diseases [160, 161]. Electrodes made of conductive metals show degradation in human physiochemical environment, which lowers their life time and leads to local inflammation or fibrotic tissue growth [162]. Since silicon oxycarbide has high chemical durability in acidic and basic environments, it is a suitable material for fabricating protective layers for metal electrodes [163, 164]. Besides, silicon oxycarbide materials have a broad range of electrical conductivity values, which could be tuned via conductive doping or by adjusting its “free carbon” content [19, 165, 166]. Kaspar *et al.* [167] reported relatively high electrical conductivity of 2.3 S/m for silicon oxycarbide with 54.2 wt.% “free carbon” content. Silicon oxycarbide materials have thus the potential to be applied as biomedical electrodes. Perale *et al.* [168] fabricated silicon oxycarbide filaments via micro-co-extrusion of polymer precursors, and reached with 50 wt.% carbon black doping an electrical conductivity of about 0.4 S/m. Although still no specific biomedical research of silicon oxycarbide electrodes has been reported, conductive medical electrodes based on silicon oxycarbide are

promising substitutes for metal electrodes thanks to the high physiochemical stability and the processing advantages of silicon oxycarbide materials via polymer precursors.

Non-cytotoxic properties

Silicon oxycarbide is a non-cytotoxic substrate material. Hoppe *et al.* [4] summarized two methods for assessing the cellular response to biomaterials. In the indirect method, the cell viability is assessed in cell cultivation solutions, which are conditioned with biomaterial leaching products. And there is no direct contact between cells and biomaterial. In the direct method, cells are seeded directly on biomaterial surfaces and thus the material surface characteristics (e.g., surface topography, porosity) have a direct influence on cell growth and proliferation.

The biocompatibility of silicon oxycarbide has been extensively investigated by different cell culture tests. As shown in Table 2-1, the released species from ternary silicon oxycarbide have been shown to be non-cytotoxic in all investigated cases. However, in some tests, evaluation of cell markers when cells were attached to silicon oxycarbide monoliths or coatings has shown reduced cell viability compared to the control (usually polystyrene, titanium or cover glass). Silicon oxycarbide monoliths and coatings derived from polymer precursors undergo thermolysis with gas evolution during their conversion to silicon oxycarbide. Thus, if not polished, the surface morphology of silicon oxycarbide is expected to have high roughness and porosity, differing from that of the control surfaces polystyrene, titanium and cover glass slides. Since cell adhesion is influenced by surface morphology [169], an unsuitable surface roughness could be the reason for the reduced cell viability on silicon oxycarbide specimens, as also stated by Gaweda *et al.* [20]. On the other hand, several studies found out that a high polar surface energy is beneficial for the cell adhesion [170-172]. Silicon oxycarbide is reported to have much higher dispersive surface energy than vitreous silica [173], which could also lead to an unfavorable surface energy (comprising both polar and dispersive parts) situation for cell attaching. Therefore, direct cellular tests on silicon oxycarbide monolith samples and coatings are challenging as such tests require the surface to be conditioned for improved protein and cell adhesion.

Furthermore, since the publication of Ca/Mg modified silicon oxycarbide by Gonzalo-Juan *et al.* [21], an innovative approach is receiving attention, namely the modification of silicon oxycarbide with therapeutic ions (such as Ca, Zn, Sr, *etc.*), which should enhance the potential to achieve high bioactivity of silicon oxycarbide or to induce specific healing or therapeutic effect by the controlled release of such ions [4]. Research work on this kind of modified silicon oxycarbide materials is still in its infancy but it is expected

to increase, given the high potential of ion releasing inorganic materials for bone and soft tissue engineering [79, 174, 175].

Table 2-1. Summary of cytotoxic investigations on silicon oxycarbide materials in literature.

Material form	Sample information	Test method	Test cell	Result	Ref.
Nanowires (ca. 100 nm diameter)	CVD derived SiOC ($\text{Si}_1\text{O}_{1.42}\text{C}_{0.37}$) nanowires on Si substrate	Indirect/ Direct	L929 cells	No cytotoxic effect could be found in indirect test. Higher cell viability, cyclin D1 transcript on nanowires than on flat silica at long testing time (96 h) in direct test.	[18]
Disc (3 cm diameter)	Polymethylsiloxane derived (1200 °C in N_2) SiOC	Direct	MG-63 cells; L929 cells	Cell proliferation on SiOC disc comparable to tissue culture plastic control.	[19]
Coating on Ti substrate	Silsesquioxane derived (800 °C in Argon) SiOC	Direct	MG-63 cells	Comparable cell number (LDH activity) on coating to that on Ti and polystyrene. Lower cell viability (mitochondrial activity) on coating than on Ti or polystyrene references, indicating negative surface influence.	[20]
Monolith	Polysilsesquioxane derived (1100 °C in Argon) SiOC	Direct	MEF cells	Significantly reduced cell viability on SiOC than on polystyrene and cover glass.	[21]
Powder	Polysilsesquioxane/Vinyl-containing polysiloxane derived (1100 °C in Argon) SiOC (SSA: ca. 20 m^2/g)	Indirect	HEK-293 cells	Slightly reduced cell viability at high solid loadings. Residual “free carbon” does not affect the cytotoxicity.	[21]
Mesoporous powder	Sol-gel (siloxane) derived SiOC (SSA: ca. 450 m^2/g)	Indirect	MT-2 cell; HEC-1-A cells	No cytotoxic effect could be observed.	[176]

2.3.2. Bioactivity of silicon oxycarbide

The research work on the bioactivity of silicon oxycarbide materials is limited until now. Gaweda *et al.* [20] prepared silicon oxycarbide coating (about 1 μm thick) on Ti substrate via dip-coating method. The coated substrates were tested in SBF solution for 5 weeks, during which every week the SBF solution was refreshed. It has been found out that hydroxyapatite forms preferentially on silicon oxycarbide coatings with low carbon content [20]. The morphology of formed hydroxyapatite is correlated to the varying carbon content and surface roughness [20].

Gonzalo-Juan *et al.* [21] investigated silicon oxycarbide materials in SBF solution under stirring for different time periods. Ternary silicon oxycarbide has shown no hydroxyapatite formation after 2 weeks testing; whereas, Ca and Mg modified silicon oxycarbide glass (chemical composition: $\text{Si}_1\text{Mg}_{0.07}\text{Ca}_{0.05}\text{O}_{1.73}\text{C}_{0.96}$) has high hydroxyapatite forming ability (hydroxyapatite formation after already 3 days), confirmed by a decrease of calcium and phosphorus concentration in the solution [21]. This enhancement of silicon oxycarbide bioactivity by Ca and Mg modification is correlated to the network modifier effect: calcium is network modifier and magnesium is network intermediate (act as both network former and network modifier) [3]. As mentioned in section 2.2.1, the incorporation of network modifier in silicate glasses lowers network connectivity, increasing glass dissolution and thus bioactivity. Ionescu *et al.* [66] made a systematic investigation of the network structure in Ca and Mg modified silicon oxycarbide. Ca and Mg modification lead to the formation of Si Q^3 units, and lower the content of network carbon [66]. Both factors are responsible for the good bioactivity of Ca and Mg modified silicon oxycarbide [66]. Furthermore, the unique nano-domain structure of silicon oxycarbide (see section 2.1.2) may also play a role on the bioactivity of silicon oxycarbide.

In summary, the research work until now has proven apatite forming ability of ternary silicon oxycarbide upon SBF immersion. This apatite formation is very slow and can take as long as 5 weeks. A much faster apatite formation is achievable upon incorporating network modifiers into silicon oxycarbide network architecture.

2.3.3. Silicon oxycarbide based surface active materials

Antibacterial surface material

By introducing Ag doping, silicon oxycarbide can attain antibacterial properties. Khalilpour *et al.* [177] reported Ag/SiO_xC_y plasma antimicrobial coatings on stainless steel. Ag nanoparticles (5-50 nm) covered in chemical vapor deposited (CVD) silicon oxycarbide layer could be continuously released and thus the surfaces exhibited excellent antimicrobial activity against *Methicillin-resistant Staphylococcus aureus* (MRSA). Guo *et al.* [178] proposed Ag/SiOC composite fibers fabricated via electro-spinning of polymethylsilsesquioxane and silver oxide nanoparticles or silver acetate co-solution. The formation of Ag nano/micro-particles after thermolysis led to antibacterial effects against Gram-negative *Escherichia coli* bacteria and Gram-positive *Staphylococcus aureus* bacteria. By introducing ZnO nanoparticles into silicon oxycarbide polymer precursor, ZnO doped silicon oxycarbides could be synthesized after thermolysis in argon and they exhibited enhanced photocatalytic activity compared to ternary silicon oxycarbide [179]. As mentioned in section 2.2.2, ZnO nanoparticles and Zn-containing bioactive glasses can show antibacterial properties. ZnO doped silicon oxycarbide could thus also be antibacterial. Therefore, silicon oxycarbide based antibacterial materials can be developed via antibacterial ion doping. Unlike silicate glasses, in which ion doping and homogenization happen at glass melting temperature and the amount of doping ions is limited by the glass melting properties, such as devitrification, ion doping and homogenization in silicon oxycarbide can be conducted on polymer precursor at room temperature.

Drug delivery material

Mesoporous materials are promising for drug delivery, since their high porosity, specific surface area and pore volume provide sufficient capacity for the adsorption of drug molecules. Besides, the possibility to adjust their pore structure and conduct surface functionalization is beneficial for achieving targeted drug release, which is desirable in modern medicine [180]. Furthermore, mesoporous silicon oxycarbide based biomaterials are suitable material candidates for drug delivery application due to their high biocompatibility (see section 2.3.1). Tamayo *et al.* [176] synthesized mesoporous silicon oxycarbide via sol-gel process. The obtained silicon oxycarbide materials show a bimodal pore size distribution at 6 nm and 70 nm with SSA as high as 442 m²/g. The observed loading capacity of acyclovir drug is higher than that of mesoporous silica. This improved drug loading is correlated to additional surface carbon functional groups on silicon oxycarbide [176]. The same research group performed a systematical investigation of the dispersive surface free energy of silicon oxycarbide materials and found that their surface

is more similar to that of graphitic materials, rather than that of vitreous silica. Their high dispersive surface energy is correlated to structural heterogeneities in molecular size, which originate probably from graphitic carbon layers on silicon oxycarbide surface (see section 2.1.2) [173]. Thus, the unique heterogeneous silicon oxycarbide surface, comprising both graphitic “free carbon” and oxygen-rich Si-O_xC_{4-x} domains, allows two surface modification strategies: either the functionalization of silicon oxycarbide surface silanol groups with γ-aminopropyl trimethoxy silane or the introduction of carbonyl and carboxylic functionalities to silicon oxycarbide surface via chemical oxidation of surface “free carbon” can influence the adsorption and release kinetics of acyclovir significantly [176, 181].

Furthermore, hierarchical pore structure in silicon oxycarbide is achievable via HF etching. Vakifahmetoglu *et al.* [182] synthesized silicon oxycarbide with a bimodal pore size distribution at < 5 nm and 10-20 nm. The micropores (< 5 nm) show higher bovine serum albumin loading capacity than mesopores [182]. Interestingly, Tamayo *et al.* [176] find that the silanol modification processes preferentially inside mesopores. This pore size dependent affinity of drug or surface modifier implies the potential of hierarchical pore structure in silicon oxycarbide materials to be applied for multidrug delivery systems. Meanwhile, by applying novel processing method mesoporous hollow silicon oxycarbide capsules with a diameter of *ca.* 400 nm and a thickness of *ca.* 40 nm have been synthesized [183]. Their mesoporous shell allows the penetration of drug into the inside hollow spaces and their capsule structure promises for a controlled release [183]. The diameter or thickness of such capsules can be adjusted according to need [184]. Such flexibility in designing porous silicon oxycarbide is beneficial for its potential drug delivery applications.

3. Experimental Procedure

3.1. Material preparation

3.1.1. PMS derived silicon oxycarbide

A commercially available polymethylsilsesquioxane (PMS) with functional ethoxy groups (Silres® MK powder, Wacker, Munich, Germany) was mixed and ground in an mortar with calcium acetylacetonate ($\text{Ca}(\text{acac})_2$, Sigma Aldrich, Munich, Germany), boric acid (H_3BO_3 , Sigma Aldrich, Munich, Germany) and/or strontium acetylacetonate ($\text{Sr}(\text{acac})_2$, Sigma Aldrich, Munich, Germany) according to the set molar ratios at room temperature to achieve homogenous mixtures. All mixtures were cross-linked at 250 °C for 4 h and subsequently pyrolyzed in argon flow at 1100 °C for 3 h, as shown in the pyrolysis program in Figure 3-1. The achieved black samples were ground into powders. The amounts of chemicals for preparing the powder mixtures and the sample names before and after pyrolysis are listed in Table 3-1.

Table 3-1. The amounts of Silres® MK, calcium acetylacetonate, boric acid and strontium acetylacetonate used for the preparation of the precursor mixtures and the corresponding molar ratios.

Precursor mixture	Pyrolyzed sample	Silres® MK (g)	$\text{Ca}(\text{acac})_2$ (g)	H_3BO_3 (g)	$\text{Sr}(\text{acac})_2$ (g)	Molar ratio
MK	SiOC	2	-	-	-	-
MK-B7	SiOC-B7	2	-	0.12	-	B/Si=0.07
MK-Ca5	SiOC-Ca5	2	0.36	-	-	Ca/Si=0.05
MK-B7Ca5	SiOC-B7Ca5	2	0.36	0.12	-	B/Si=0.07, Ca/Si=0.05
MK-Ca12	SiOC-Ca12	2	0.87	-	-	Ca/Si=0.12
MK-B7Ca5Sr0.8	SiOC-B7Ca5Sr0.8	2	0.36	0.12	0.07	B/Si=0.07, Ca/Si=0.05, Sr/Si=0.008
MK-B7Ca5Sr4	SiOC-B7Ca5Sr4	2	0.36	0.12	0.33	B/Si=0.07, Ca/Si=0.05, Sr/Si=0.04

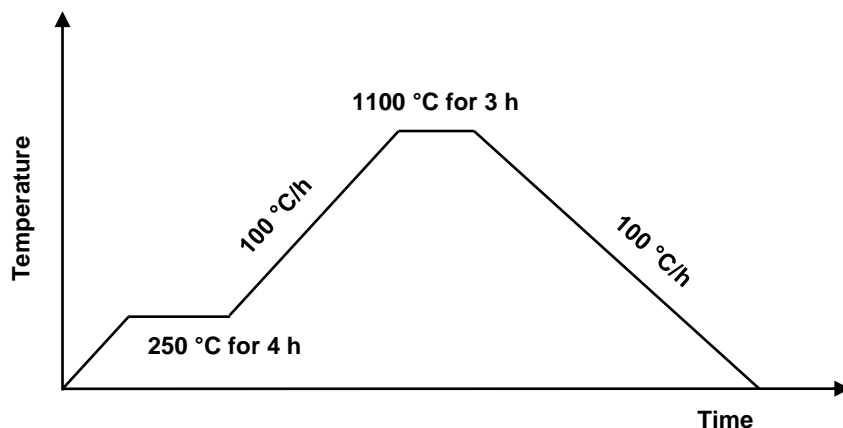


Figure 3-1. Pyrolysis program for PMS derived silicon oxycarbides.

3.1.2. Sol-gel derived silicon oxycarbide

Triethoxymethylsilane ($\text{CH}_3\text{Si}(\text{OC}_2\text{H}_5)_3$, Alfa Aesar, Kandel, Germany) and calcium nitrate tetrahydrate ($\text{Ca}(\text{NO}_3)_2 \cdot 4\text{H}_2\text{O}$, Carl Roth, Karlsruhe, Germany) were mixed with nitric acid solution (0.01 M) and stirred until a homogeneous sol was formed. By adjusting the sol to $\text{pH} \approx 9.0$ with ammonia solution (1 M) titration, the gelation process set in and the obtained gel was aged at 60°C and subsequently dried at 120°C . The complete sol-gel process was depicted in Figure 3-2. By varying the amount of calcium nitrate tetrahydrate, four different xerogels could be prepared with corresponding Ca/Si molar ratios of 0.00, 0.05, 0.12 and 0.50 and they were denoted as SG-Ca0, SG-Ca5, SG-Ca12 and SG-Ca50, respectively, as shown in Table 3-2.

Table 3-2. Amounts of chemicals for sol-gel procedure.

Xerogel	Pyrolyzed sample	Molar ratio (Ca/Si)	Triethoxymethylsilane (g)	0.01M HNO_3 Solution (g)	$\text{Ca}(\text{NO}_3)_2 \cdot 4\text{H}_2\text{O}$ (g)
SG-Ca0	SiCa0	0.00	10	3.0	0.00
SG-Ca5	SiCa5	0.05	10	3.5	0.66
SG-Ca12	SiCa12	0.12	10	4.0	1.59
SG-Ca50	SiCa50	0.50	10	4.5	6.62

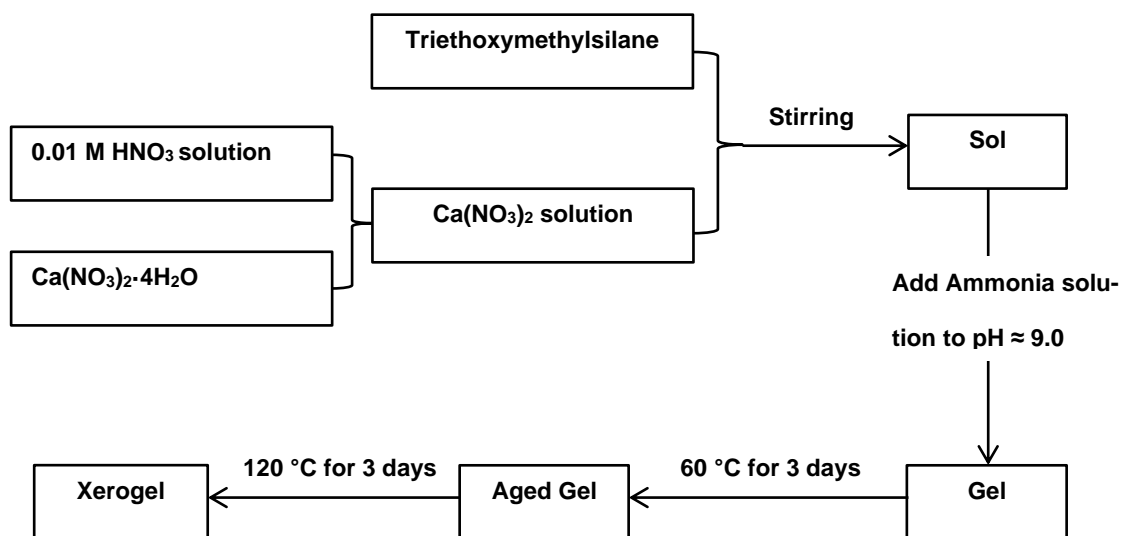


Figure 3-2. Sol-gel procedure for silicon oxycarbide xerogel precursors.

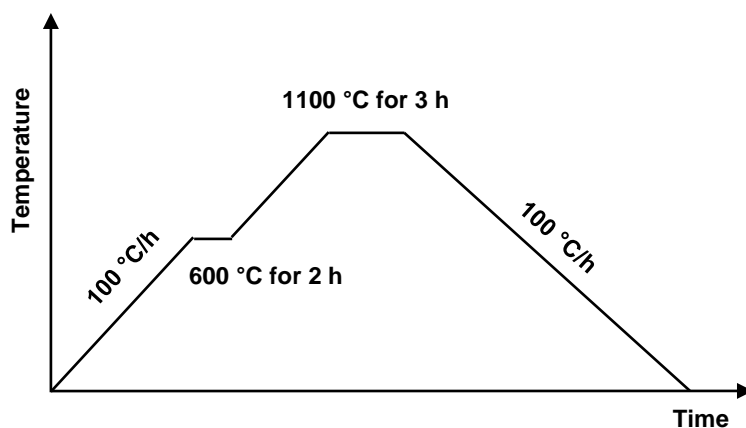


Figure 3-3. Pyrolysis program for sol-gel derived silicon oxycarbides.

The xerogel samples were ground to powder and then pyrolyzed at 1100 °C in argon flow to silicon oxycarbide materials according to the pyrolysis program in Figure 3-3. During the heating stage, a holding time of 2 h at 600 °C was conducted, in order to eliminate the remaining nitrate groups from calcium nitrate. The obtained silicon oxycarbide materials were ground to powder for further analysis and the samples derived from SG-Ca0, SG-Ca5, SG-Ca12 and SG-Ca50 were denoted as SiCa0, SiCa5, SiCa12 and SiCa50, respectively.

3.2. Bioactivity assessment

3.2.1. Simulated body fluid

Acellular bioactivity tests were performed by exposing the powder samples to the simulated body fluid (SBF). The simulated body fluid was prepared according to Kokubo [88]. The preparation procedure was conducted according to ISO 23317: 700 ml deionized water was filled in an 1 L plastic bottle and heated up to 37 °C; the reagents were then added according to the steps listed in Table 3-3; Tris was added in small portions to avoid rapid pH increase; after a pH value of 7.45 was reached, the solution was transferred to an 1 L volumetric flask and diluted with deionized water to 1 L. The precipitation-free SBF solution was then stored in a cool environment. Before use, its pH value was adjusted with 1-2 ml of 1 M HCl solution to be 7.40 at 37°C.

Table 3-3. Reagents for the preparation of SBF solution.

Step	Reagent	Amount for 1 L SBF	Purity and provider
1	NaCl	8.035 g	≥99.0%, Sigma Aldrich
2	NaHCO ₃	0.355 g	≥99.7%, Sigma Aldrich
3	KCl	0.225 g	≥99.0%, Sigma Aldrich
4	K ₂ HPO ₄ ·3H ₂ O	0.231 g	≥99.0%, Merck
5	MgCl ₂ ·6H ₂ O	0.311 g	≥99.0%, Merck
6	1M HCl	38 ml	Diluted from 37% HCl Solution, Sigma Aldrich
7	CaCl ₂ ·2H ₂ O	0.386 g	≥99.0%, Merck
8	Na ₂ SO ₄	0.072 g	≥99.99%, Sigma Aldrich
9	Tris(hydroxymethyl)aminomethane	Ca. 6.0 g	≥99.8%, Sigma Aldrich

3.2.2. TC04 method

The *in vitro* bioactivity tests were done based on the TC04 (Technical Committee on Bioglasses) method reported by Macon *et al* [89]. The solid powder to SBF solution ratio was fixed at 75 mg to 50 ml. After the mixture of solid powders with SBF solution in airtight poly-ethylene (PE) bottles, the incubation was conducted at 37 °C in a drying oven. Different test periods (4 h, 8 h, 24 h, 72 h, 1 week, 2 weeks, 3 weeks, 4 weeks) were chosen for each sample. Additionally, 72 h soaking tests were carried out at 24 °C and 55 °C. At the end of each period, solid powders were separated from SBF solution via filtration.

The filtered powders were washed with deionized water and acetone and subsequently dried at 40 °C. For comparison purposes, a commercially available bioactive glass with 45S5 composition (45 wt.% SiO₂, 24.5 wt.% CaO, 24.5 wt.% Na₂O, 6.0 wt.% P₂O₅) (Vitryxx® Bioactive Glass, Schott, Mainz, Germany) was chosen for the SBF test.

3.3. Material characterization

3.3.1. Elemental analysis

The carbon and oxygen contents of pyrolyzed silicon oxycarbide samples were determined by a carbon analyzer Leco-200 (Leco Corporation, St. Joseph, USA) and a N/O analyzer Leco TC-436 (Leco Corporation, St. Joseph, USA), respectively. Sorarù *et al.* [46] reported the hydrogen contents of silicon oxycarbides pyrolyzed at 1000 °C to be lower than 0.3 wt.%. Hydrogen contents in silicon oxycarbide samples of the present work (pyrolyzed at 1100 °C) were thus considered to be negligible. The calcium and boron contents for SiOC-B7Ca5 and SiOC-B7 samples were measured via inductively coupled plasma – optical emission spectroscopy (ICP-OES) at Mikroanalytisches Labor Pascher (Remagen, Germany). The silicon content was determined by subtracting carbon, oxygen, calcium and boron contents from 100%.

3.3.2. Thermogravimetric analysis with evolved gas analysis

The polymer-to-ceramic transformation of the prepared polymer precursors was investigated with thermogravimetric analysis (TGA, Netzsch 449C Jupiter®, Selb, Germany) coupled with *in situ* evolved gas analysis (EGA), *i.e.*, via mass spectrometry (Netzsch QMS 403C Aeolos®, Selb, Germany) and FTIR spectroscopy (Bruker Tensor 27, Billerica, USA). The investigation was conducted by Dipl.-Ing. Claudia Fasel in the working group of Prof. Ralf Riedel at the Technical University of Darmstadt. The measurements were performed in argon flow (30 ml/min) with a heating rate of 5 °C/min to 1300 °C.

3.3.3. X-ray diffraction

X-ray powder diffraction was performed with a STOE STADI P (STOE, Darmstadt, Germany) equipped with Mo K α X-ray source, Ge(111) monochromator and linear position sensitive detector (PSD) in transmission geometry in a 2 θ range of 5-45° and the diffractograms were analyzed with crystallographic program MATCH!.

3.3.4. Fourier-transform infrared spectroscopy

FTIR spectroscopy measurements were carried out on a Varian IR-670 spectrometer (Agilent, Santa Clara, USA) from 400 to 4000 cm⁻¹. Powder samples were mixed with KBr powder in a concentration of 0.2-1 wt.% (0.2 wt.% for organic materials, 1 wt.% for inorganic materials), and then pressed to transparent or translucent thin pellets (*ca.* 1 mm thick) with a diameter of 12 mm prior measurements.

3.3.5. Transmission electron microscopy

The transmission electron microscopy (TEM) investigation was conducted by M.Sc. Maximilian Trapp in the working group of Prof. Hans-Joachim Kleebe at the Technical University of Darmstadt. For the TEM studies, powder samples were prepared on copper TEM-grids with a supporting holey carbon film (400 mesh, Plano, Wetzlar, Germany). The samples were lightly carbon coated (Med 010, Balzers Union, Balzers, Liechtenstein) to minimize charging effects under the incident electron beam. The TEM investigations were performed on a JEOL JEM 2100F (JEOL, Tokyo, Japan) equipped with a TEM 250 SDD energy dispersive spectroscopy (EDS) system (Oxford Instruments, Wiesbaden, Germany).

3.3.6. Scanning electron microscopy

Powder samples were loaded onto carbon pads on aluminum sample holders and subsequently sputtered lightly with gold. The surface morphologies of the samples were investigated by scanning electron microscopy (SEM) (JEOL JSM-7600F, Tokio, Japan).

3.3.7. Solid state nuclear magnetic resonance

The solid state nuclear magnetic resonance (NMR) measurements were conducted by Dr. Hergen Breitzke in the working group of Prof. Gerd Buntkowsky at the Technical University of Darmstadt. ^{11}B and ^{29}Si MAS solid state NMR measurements were carried out at room temperature on a Bruker AVANCE II+ spectrometer (Bruker, Billerica, USA) at 400 MHz proton resonance frequency, employing a Bruker 4 mm double resonance probe. ^{29}Si spectra were recorded utilizing Bruker ZG sequence at spinning rates of 8 kHz, and pulse angles of 22° , and 120 s relaxation delay. During data acquisition TPPM (Two pulse phase modulation) decoupling with a 15° phase jump was applied [185]. ^{29}Si Spectra were referenced externally to tetramethylsilane (TMS) at 0 ppm. ^{11}B spectra were recorded utilizing the EASY background suppression sequence, applying 30° excitation pulse and 2 s relaxation delay [186]. The EASY sequence was modified with respect to the background suppression part, by including an additional 90° pulse and delay of 10 ms before the background subtraction part of the sequence. ^{11}B spectra were referenced externally to $\text{BF}_3\cdot\text{OEt}_2$ at 0 ppm.

3.3.8. Laser particle size analysis

The particle sizes of the powder samples were analyzed with a Laser Particle Sizer (Fritsch Analysette 22 Compact, Idar-Oberstein, Germany). The powders were dispersed in deionized water using an ultrasonic bath (3 minutes) and then measured in a transparent chamber under continuous circulation.

3.3.9. Zeta potential analysis

Powder samples were dispersed in deionized water ($\text{pH} \approx 5.0$ at room temperature), and the zeta potential of the solid-liquid interface was measured using the Smoluchowski equation [187] (Zetasizer Nano-ZS, Malvern Instruments, Kassel, Germany). As reference, the zeta potential of synthetic hydroxyapatite powder (HA) (Sigma Aldrich, Munich, Germany) was measured in deionized water, too.

3.3.10. Inductively coupled plasma - optical emission spectroscopy analysis

The pH values of the filtered SBF solutions were measured and the solutions were used for inductively coupled plasma - optical emission spectroscopy (ICP-OES) analysis. For the ICP-OES measurements, the solutions were diluted up to 200 times and the Si, Ca, P and Sr concentrations in diluted solutions were analyzed with an Agilent 720 ICP-OES (Agilent, Santa Clara, USA) spectrometer. The ICP-OES measurements were conducted by Dipl.-Geol. Christian Scholz in the working group of Prof. Margot Isenbeck-Schröter at the Heidelberg University.

3.3.11. N₂ sorption analysis

The specific surface area of powder samples was investigated by nitrogen sorption (QuantaChrome Autosorb-3B, Graz, Austria). All samples were degassed at 180-200 °C for 20-24 h to remove surface adsorbates before the analysis. Adsorption curves of obtained isotherms were fitted via 7 points (relative pressures of 0.05-0.3) with the Brunauer-Emmett-Teller (BET) equation [188] to determine their specific surface area. Pore size distributions of the samples were evaluated by BJH method on the desorption part of the isotherms [189].

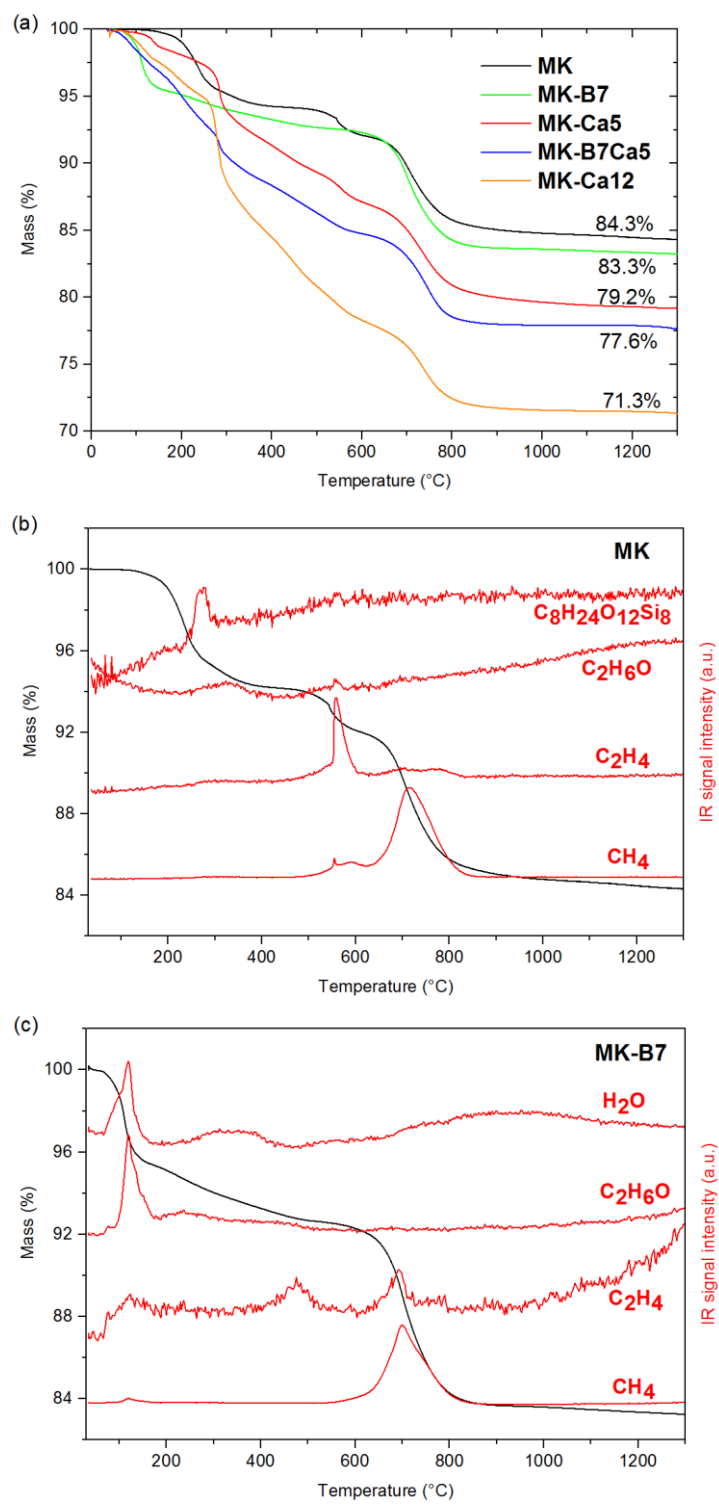
4. Results and Discussion

4.1. PMS derived Si(B,Ca)OC bioactive materials

Si(B,Ca)OC silicon oxycarbide materials were synthesized from polymethylsilsesquioxane (PMS) based precursors which were modified with boric acid and/or calcium acetylacetonate (see Table 3-1). In the following sections, the polymer-to ceramic transformation of the polymer precursors will be discussed according to the thermogravimetric analysis. The microstructure and network architecture of achieved Si(B,Ca)OC samples were analyzed with X-ray diffraction (XRD), Fourier-transform infrared spectroscopy (FTIR), transmission electron microscopy (TEM) and solid state nuclear magnetic resonance (NMR). The bioactivity of Si(B,Ca)OC in simulated body fluid (SBF) is assessed according to their ion release kinetics and apatite forming ability, and compared to that of a commercial bioactive glass with 45S5 composition. The correlation between bioactivity and structural features, especially the network architecture of the Si(B,Ca)OC materials will be discussed at the end.

4.1.1. Polymer-to-ceramic transformation

The polymer to ceramic transformations of MK, MK-B7, MK-Ca5, MK-B7Ca5 and MK-Ca12 (see Table 3-1) were studied with thermogravimetric analysis (TGA) coupled with evolved gas analysis (EGA). The ceramic yields are given in Figure 4-1 (a). The higher weight loss of B and/or Ca-containing precursors as compared to that of the non-modified polymer is due to the decomposition reaction of H_3BO_3 and $\text{Ca}(\text{acac})_2$ during the ceramization. The assignment of IR signals to degassing species was conducted by Dipl.-Ing. Claudia Fasel. Figure 4-1 shows the intensity evolution of specific IR-traces with temperature of different degassing species during ceramization.



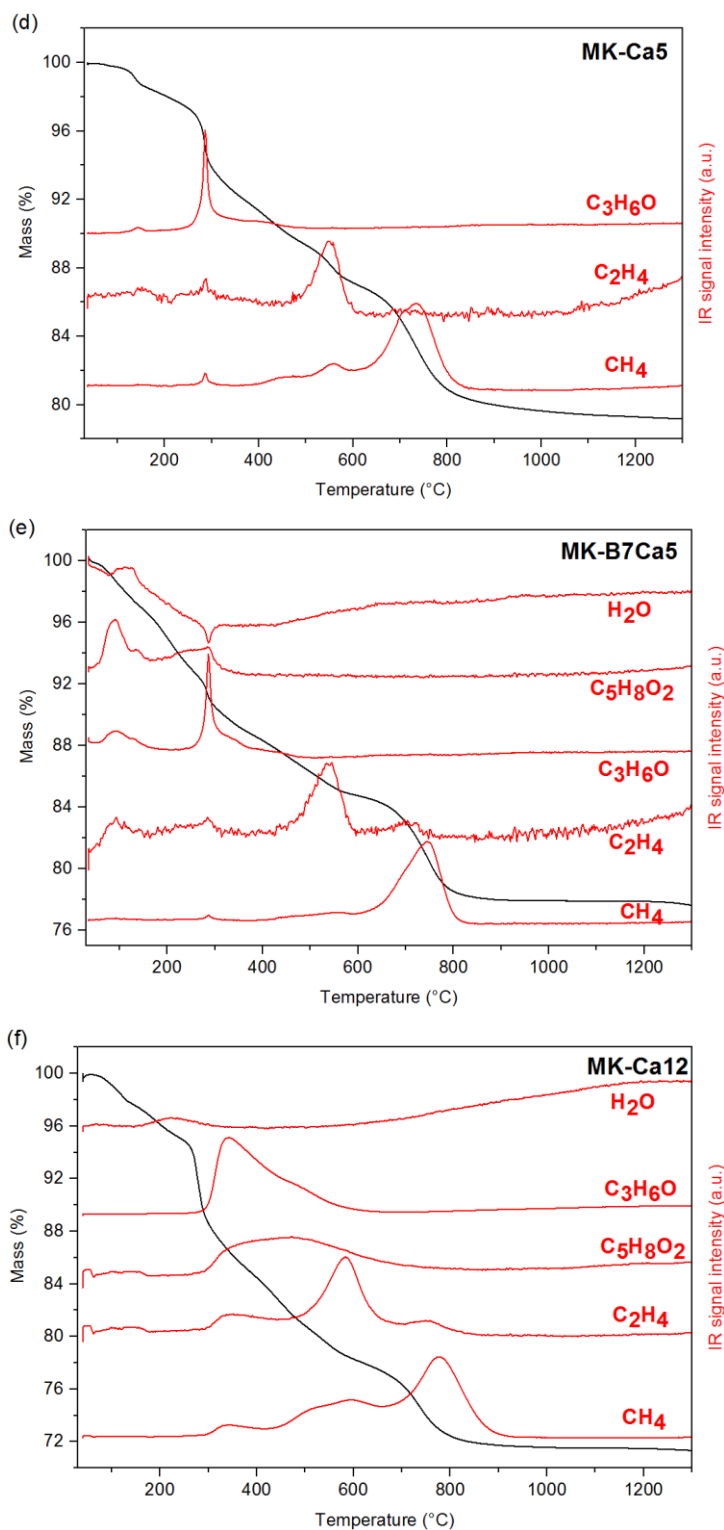


Figure 4-1. (a) Thermogravimetric (TGA) curves for MK (black line), MK-B7 (green line), MK-Ca5 (red line), MK-B7Ca5 (blue line) and MK-Ca12 (orange line). The characteristic peaks of the evolved gas species are determined via in situ FTIR to be located between 758-787 cm^{-1} for $C_8H_{24}O_{12}Si_8$, 3638-3689 cm^{-1} for C_2H_6O , 1709-1763 cm^{-1} for C_3H_6O , 1594-1651 cm^{-1} for $C_5H_8O_2$, 1454-1546 cm^{-1} for H_2O , 948-952 cm^{-1} for C_2H_4 and 3011-3019 cm^{-1} for CH_4 . The individual TG curves and in situ recorded signal intensities of the characteristic IR peaks are shown in (b), (c), (d), (e), and (f), respectively.

At temperatures beyond 400 °C, the main degassing species are CH₄ and C₂H₄ for all investigated precursors. Silres® MK polymer has methyl groups, which are split off from the polymer network at these temperatures.

At temperatures below 400 °C, the nature of the released species depends on the precursor used (*i.e.*, on the chemical modification of the polymethylsilsesquioxane). The evolution of polyhedral oligomeric silsesquioxane (POSS – C₈H₂₄O₁₂Si₈) was observed for pure MK polymer and not for precursors with modifiers, indicating the better stabilization of small polymer molecules via modifying reactions [62]. Ethanol (C₂H₆O) release indicates the reaction between ethoxy groups (in polymer) and hydroxyl groups. In MK-B7, the release of ethanol is more significant than that in MK, and is considered to be a consequence of the modification with H₃BO₃ (see Figure 4-2). In MK-Ca5, MK-B7Ca5 and MK-Ca12, ethanol release is suppressed, whereas acetylacetone (C₅H₈O₂) and acetone (C₃H₆O) outgassing dominates, being correlated to the presence of acetylacetonate groups in the Ca precursor [190-192]. In MK-B7Ca5, the hydroxyl groups in H₃BO₃ lead to the formation and release of acetylacetone at temperatures lower than 200 °C. As the ethoxy groups present in the polymer can react with metal acetylacetonates [193], no ethanol release can be observed during the thermal treatment of MK-Ca5, MK-Ca12 and MK-B7Ca5. Instead, the acetylacetonate groups present in the precursors decompose upon acetone release at temperature beyond 200 °C.

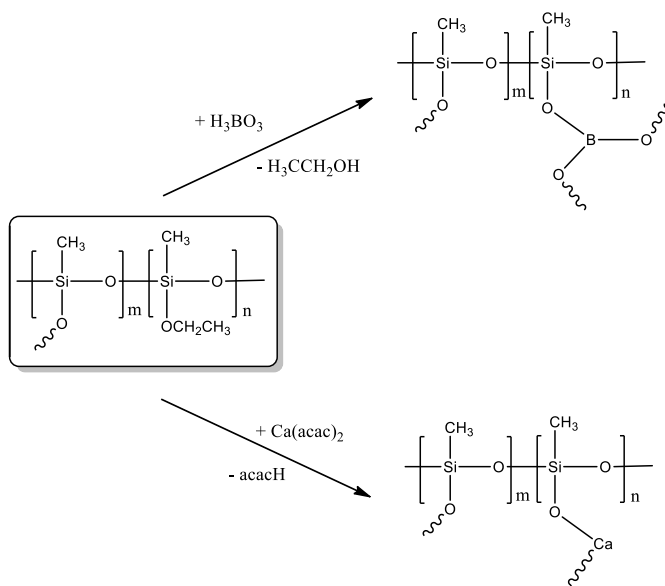


Figure 4-2. Schematic illustration of the chemical modification of the polymethylsilsesquioxane with boric acid and/or calcium acetylacetonate.

4.1.2. Structure characterization

As shown in Figure 4-3, the FTIR spectra of the pyrolyzed silicon oxycarbides are dominated by absorptions at about 460 cm^{-1} , 1083 cm^{-1} and 1220 cm^{-1} , corresponding to the deformation of O-Si-O bond and two asymmetric Si-O-Si stretching modes, respectively. The absorption at 800 cm^{-1} can be attributed to an overlapping of Si-C and bending Si-O-Si vibrations. Additionally, bands at 670 cm^{-1} and 912 cm^{-1} corresponding to $\nu(\text{Si-O-B})$ and at 1400 cm^{-1} assigned to $\nu(\text{B-O})$ are observed in boron-containing samples, *i.e.* SiOC-B7Ca5 and SiOC-B7 [194-196]. The spectra of Ca-containing samples show several small absorption bands in the range from $940\text{--}1040\text{ cm}^{-1}$, indicating the existence of Si-O \cdot sites (*i.e.*, bearing non-bridging-oxygens) [197, 198]. Absorption bands at 564 cm^{-1} and 717 cm^{-1} were reported to be related to pseudowollastonite [199], and their intensities increase with increasing Ca content from SiOC-Ca5 to SiOC-Ca12 as shown in Figure 4-3. Based on the results from the FTIR spectroscopy, one can conclude that the incorporation of Ca and B within silicon oxycarbide occurs upon formation of silicon sites bearing non-bridging-oxygens (*i.e.*, Si-O \cdot), Si-O-B bonds and small amounts of pseudowollastonite.

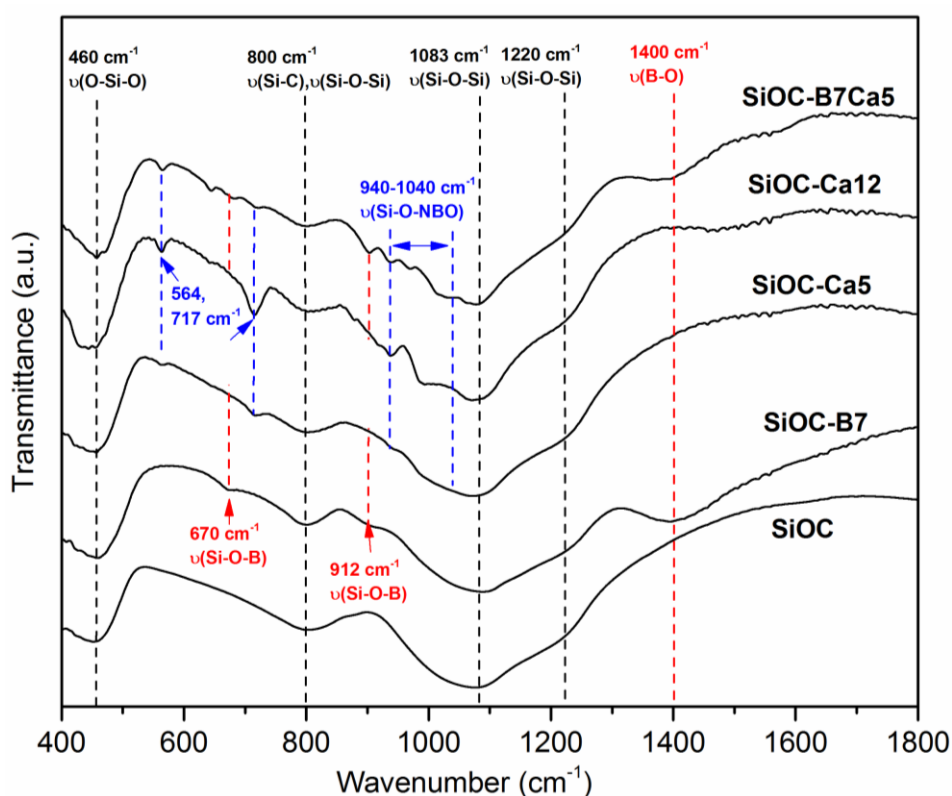


Figure 4-3. FTIR spectra of silicon oxycarbide based samples prepared upon pyrolysis of the polymethylsilsequioxane based precursors at $1100\text{ }^{\circ}\text{C}$.

The pyrolyzed silicon oxycarbides were investigated furthermore by X-ray diffraction. Typically, the pyrolysis of polysiloxanes, polysilsesquioxanes as well as of silicon-alkoxide-based sol-gel systems in inert gas atmosphere leads to the formation of amorphous silicon oxycarbides, as also shown in Figure 4-4 for SiOC. The modification of MK with boron leads upon pyrolysis to a B-containing silicon oxycarbide, which keeps its amorphous nature, as already shown in many studies in literature [60, 200]. The incorporation of Ca into silicon oxycarbide, as for SiOC-Ca5, SiOC-Ca12 and SiOC-B7Ca5, leads also to mainly amorphous materials (see Figure 4-4). Some minor amounts of wollastonite and pseudowollastonite were detected in the Ca-containing samples. The amount of crystalline phases correlates to the amount of incorporated Ca, *i.e.*, the amount of wollastonite / pseudowollastonite in SiOC-Ca12 was higher than that in SiOC-Ca5.

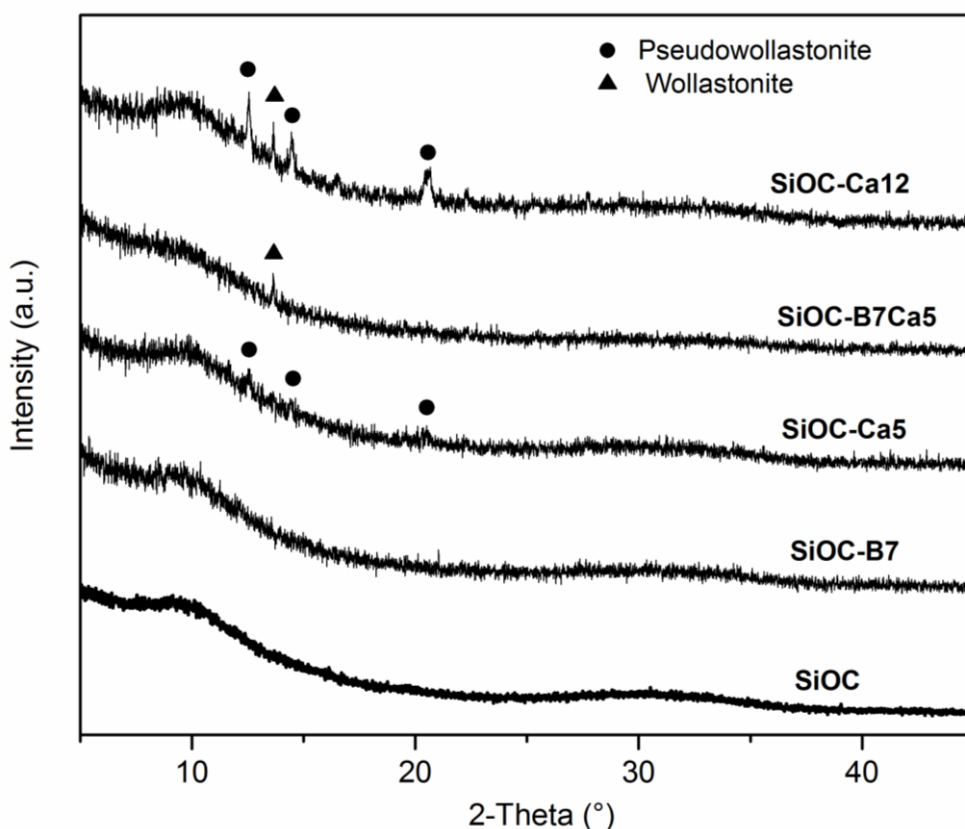


Figure 4-4. XRD pattern of silicon oxycarbide based samples prepared upon pyrolysis of the corresponding precursors at 1100 °C.

In Figure 4-5, bright field and high resolution TEM micrographs of SiOC-Ca5 and SiOC-B7Ca5 are shown. The samples are shown to be mainly amorphous, as indicated also by the XRD data, and contain small amounts of crystalline particles with sizes in the range from 200 to ca. 500 nm. EDS analysis was done by M.Sc. Maximilian Trapp and indicated in both samples in the two regions (*i.e.*, amorphous and

crystalline) very different Ca contents. Thus, the amount of Ca in the amorphous regions of SiOC-Ca5 and SiOC-B7Ca5 was shown to be in the range of 0.5-1 wt.%, whereas the crystalline regions exhibits a significantly higher Ca content of approximately 15-40 wt.%, being similar to the content of Ca in wollastonite / pseudowollastonite (23 wt.%).

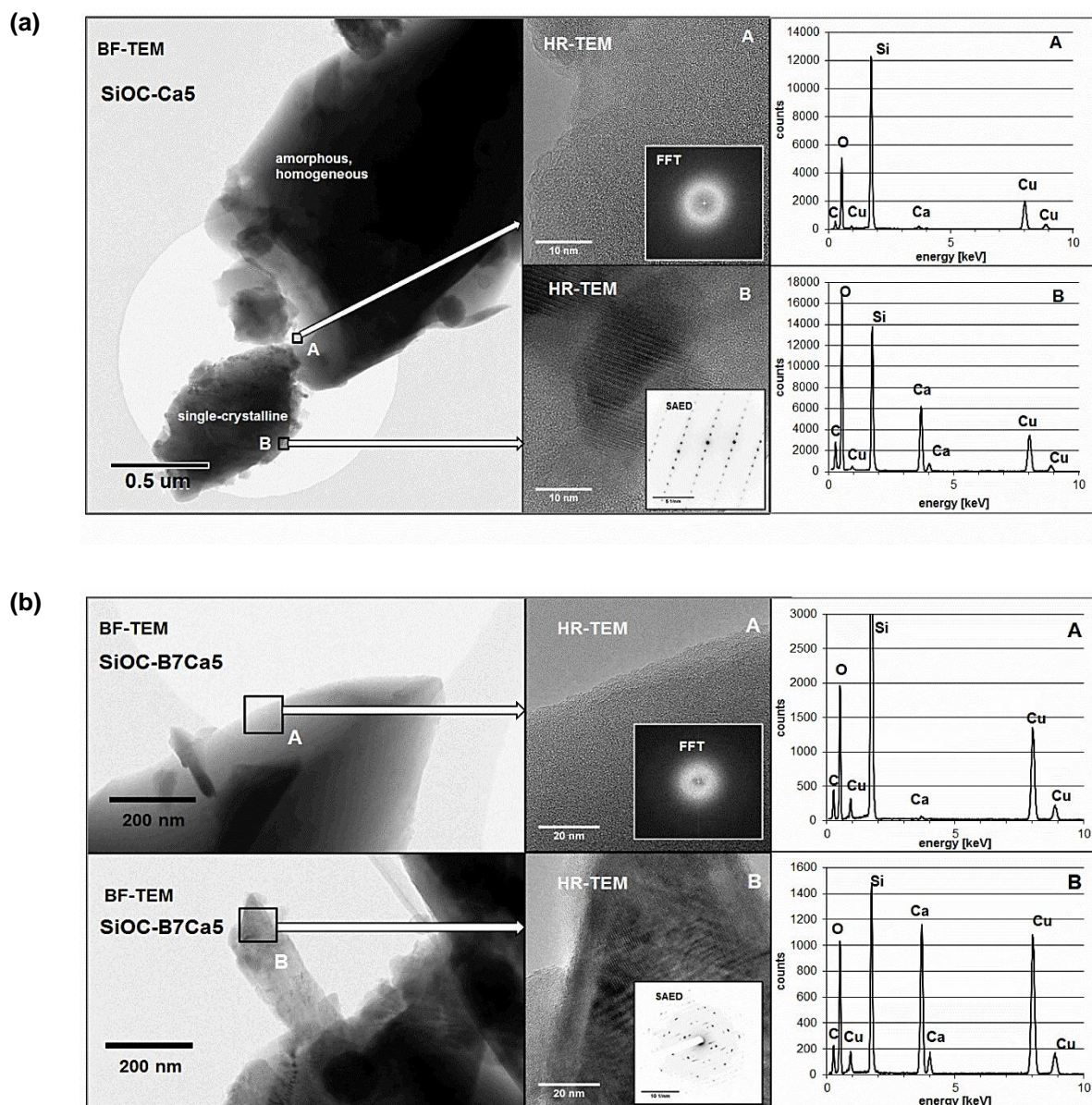


Figure 4-5. Bright field and high resolution TEM micrographs of the samples (a) SiOC-Ca5 and (b) SiOC-B7Ca5. The FFT (Fast Fourier transformation) and SAED (selected area electron diffraction) insets depict the amorphous or crystalline nature of the respective regions. As shown by the EDS measurements, the crystalline regions have a significantly higher Ca content than the Ca-poor amorphous parts, which is indicative for a phase separation process occurring in both samples.

Network architecture evaluation

The effect of Ca incorporation into silicon oxycarbide has been studied by performing a network structure analysis via solid state NMR. ^{29}Si NMR spectra measured for B and/or Ca modified silicon oxycarbides by Dr. Hergen Breitzke are shown in Figure 4-6. The spectra were deconvoluted into Gaussian/Lorentzian peaks centered at -110, -91, -85, -72, -35, +6 and -11 ppm, which were assigned to Q^4 (SiO_4 sites with 4 bridging-oxygens), Q^3 (SiO_4 sites with 3 bridging-oxygens and one non-bridging-oxygen), Q^2 (SiO_4 sites with 2 bridging-oxygens and 2 non-bridging-oxygens), SiO_3C , SiO_2C_2 , SiOC_3 and SiC_4 sites, respectively [66]. The Q^2 peak appears sharper and has a lower width than the other considered peaks, indicating that it does not belong to the oxycarbide amorphous network but rather corresponds to the calcium silicate crystalline phases (wollastonite / pseudowollastonite). Based on the fitted peak intensities, the fractions of different Si species were estimated and are summarized in Table 4-1. It can be concluded that the modification of silicon oxycarbide by B or Ca modification leads to a significant increase of the Q^4 site fractions at the expenses of the mixed-bonds sites such as SiO_3C , SiO_2C_2 , SiOC_3 and SiC_4 . Interestingly, when SiOC is modified with both B and Ca, the increase of the Q^4 site fractions is only moderate.

It has been shown in many studies that boron acts as a network former in silicon oxycarbides. Unlike B, Ca should be considered mainly as network modifier, *i.e.*, being located at silicon sites containing non-bridging oxygens. As the Q^2 sites in the investigate samples have been assigned to wollastonite / pseudowollastonite, it is obvious that Ca is located at the Q^3 sites detected in the Ca modified SiOC samples [65, 66].

SiOC-B7Ca5 and SiOC-Ca5 exhibit similar Ca/Si molar ratio and the fraction of Q^3 units in SiOC-B7Ca5 is slightly higher than that of SiOC-Ca5, indicating a better incorporation of Ca in amorphous silicon oxycarbide network in SiOC-B7Ca5. SiOC-Ca12 has significantly higher Ca/Si molar ratio, which is reflected in a higher Q^2 site fraction, thus SiOC-Ca12 contains larger amount of wollastonite / pseudowollastonite (as also shown in Figure 4-4).

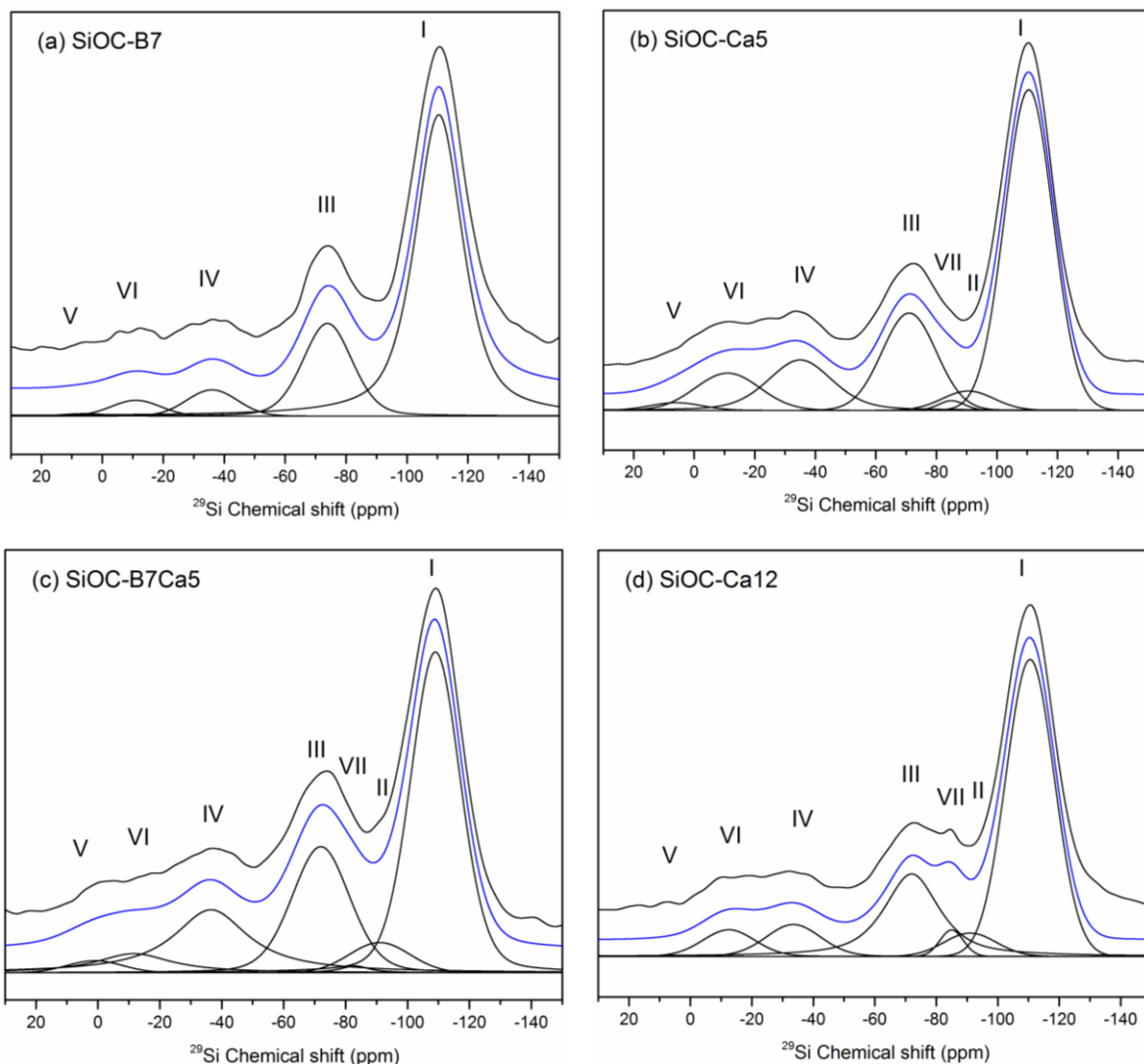


Figure 4-6. ^{29}Si MAS NMR spectra (top black lines) of (a) SiOC-B7, (b) SiOC-Ca5, (c) SiOC-B7Ca5 and (d) SiOC-Ca12. The spectra are fitted to $\text{Q}^4 \text{SiO}_4$ (peak I), $\text{Q}^3 \text{SiO}_4$ (peak II), SiO_3C (peak III), SiO_2C_2 (peak IV), SiOC_3 (peak V), SiC_4 (peak VI) and Q^2 (wollastonite / pseudowollastonite) (peak VII) sites (bottom black lines). The sum of all fitted peaks yields the blue lines in the spectra.

Table 4-1. Silicon site fractions in the prepared silicon oxycarbides determined from ^{29}Si MAS NMR spectra.

Sample	Q^4 (I)	Q^3 (II)	SiO_3C (III)	SiO_2C_2 (IV)	SiOC_3 (V)	SiC_4 (VI)	Q^2 (VII)*
SiOC [51]	44.0	-	30.4	16.1	3.0	6.5	-
SiOC-B7	66.2	-	24.2	5.6	0.4	3.6	-
SiOC-Ca5	54.3	3.5	18.6	12.9	1.4	8.4	0.9
SiOC-B7Ca5	46.7	4.9	21.2	18.9	1.8	5.7	0.8
SiOC-Ca12	55.3	6.0	16.5	10.4	0.2	7.7	3.9

* The Q^2 sites belong to the wollastonite / pseudowollastonite crystalline phases detected in SiOC-Ca5, SiOC-B7Ca5 and SiOC-Ca12.

The ^{11}B NMR spectra of SiOC-B7Ca5 and SiOC-B7 measured by Dr. Hergen Breitzke are shown in Figure 4-7. All spectra show quadrupolar splitting with a quadrupolar coupling constant $C_Q \approx 2.6$ MHz and an asymmetry parameter $\eta \approx 0.2$, which were also reported elsewhere for boron-containing silicon oxycarbides [60]. The spectra can be deconvoluted to three signals centered at 12.5, 29 and 47 ppm, which were assigned to BO_3 , BO_2C and BOC_2 sites, respectively [201]. The $\text{BO}_x\text{C}_{3-x}$ site fractions are summarized in Table 4-2. It is interesting to notice that the Ca modification of boron-containing silicon oxycarbide induces a decrease of the mix-bonded boron site fractions (see Table 4-2).

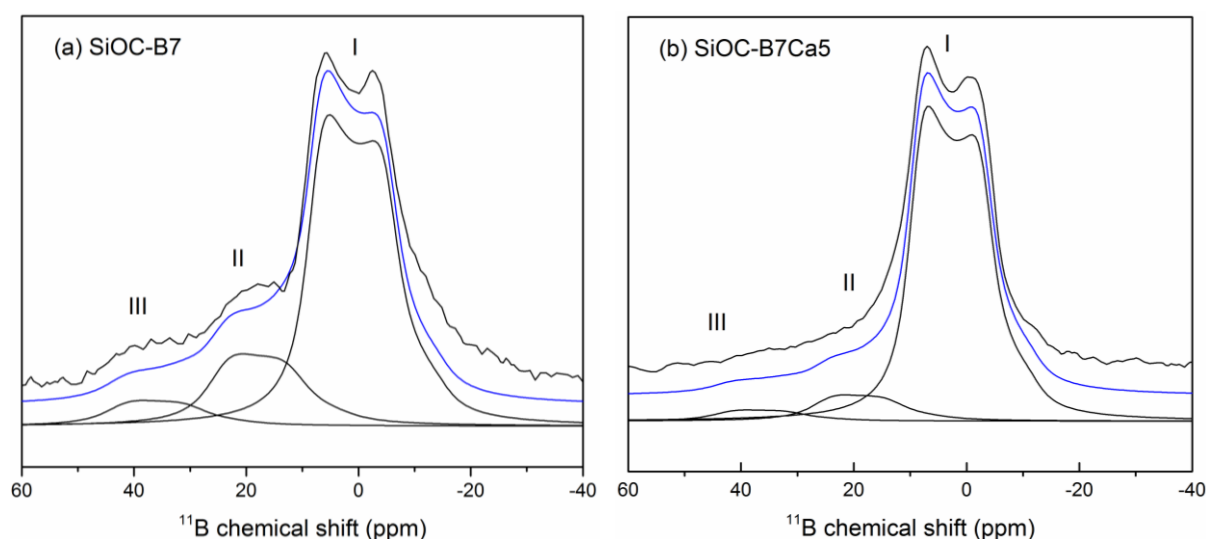


Figure 4-7. ^{11}B MAS NMR spectra (top black lines) of (a) SiOC-B7 and (b) SiOC-B7Ca5. The fitted signals are assigned to BO_3 (I), BO_2C (II) and BOC_2 (III) sites (bottom black lines). The sum of all fitted signals yields the blue lines.

Table 4-2. Boron site fractions in SiOC-B7 and SiOC-B7Ca5 determined from ^{11}B MAS NMR spectra.

	BO_3 (I)	BO_2C (II)	BOC_2 (III)
Sample	$C_Q = 2.6$ MHz	$C_Q = 2.6$ MHz	$C_Q = 2.6$ MHz
	$\eta = 0.15$	$\eta = 0.2$	$\eta = 0.2$
SiOC-B7	75	19	6
SiOC-B7Ca5	88	9	3

Chemical and phase compositions

The pyrolyzed silicon oxycarbides were also investigated concerning their elemental composition. The results of the elemental analysis of the studied samples and the calculated empirical formulae are

summarized in Table 4-4. It is clearly shown that the Ca/Si molar ratios which were set in the precursors are kept upon pyrolysis, leading to the same values in the resulting silicon oxycarbides, whereas the B/Si molar ratios are slightly lower, which can be explained by some vaporization of B-containing species during the pyrolysis process [201, 202]. The chemical and phase compositions of the SiOC-based materials were estimated based on the elemental analysis data, as reported in [42, 54]. The fraction of the CaSiO_3 crystalline phases in the investigated materials was estimated by evaluating the ratio Q^2 (crystalline phase) : Q^3 (amorphous matrix) from the NMR data (see Table 4-1). The estimated phase compositions are listed in Table 4-4.

The chemical compositions show an increase of oxygen in the silicon oxycarbide network upon Ca and/or B modification. The carbon content in silicon oxycarbide seems not to be significantly affected upon Ca modification; while the incorporation of boron seems to “repel” carbon from the network. Interestingly, also the content of the segregated sp^2 -hybridized carbon is affected by the modification of SiOC. Thus, incorporation of boron induces a decrease of the amount of free sp^2 carbon in the samples, whereas the opposite trend is observed for Ca modification, where free carbon can be introduced during the pyrolysis of organic acetylacetonate group in Ca modifier (calcium acetylacetonate).

In all Ca modified Si(B,Ca)OC systems, the fractions of the crystalline phase (*i.e.*, wollastonite, pseudowollastonite) are relatively small. However, an increase of Ca modification from SiOC-Ca5 to SiOC-Ca12 leads to an increase of the content of wollastonite / pseudowollastonite, as shown in Table 4-4, while the amounts of Ca incorporated in silicon oxycarbide amorphous matrix (*i.e.*, Q^3 fraction) are comparable. The phase diagram of the pseudo-binary SiO_2 -CaO system exhibits, similar to many other silica/alkaline-earth-metal-oxide systems, a miscibility gap in the range of Ca/Si ratio from 0.02 and 0.38 [203, 204]. In this compositional range, the CaO-SiO₂ melt partitions into two phases, *i.e.*, one silica-rich and one calcium-rich component. The Ca/Si ratios in the silicon oxycarbide samples prepared in the present study range from 0.05 to 0.12 and thus lie also within the miscibility gap of the pseudo-binary SiO_2 -CaO system. Interestingly, the oxycarbide system seems to behave similarly to the SiO_2 -CaO system, as also shown by the TEM results.

Obviously, the SiOC-Ca5 and SiOC-Ca12 samples undergo a phase separation, leading to a Ca-poor silicon oxycarbide matrix and a calcium silicate (wollastonite / pseudowollastonite) crystalline phase. There are two interesting features of the silicon oxycarbide system which can be emphasized here: (i) the alkaline-earth-metal modified silicon oxycarbide network behaves similarly to the corresponding

silicate system – clearly, the incorporation of carbon into silica does not affect the typical miscibility gap feature of alkaline-earth-metal modified silicate glass networks; (ii) the effect of the carbon incorporation may correlate to the fact that the phase separation in the Ca-containing silicon oxycarbide network occurs in the solid state, whereas the partitioning of SiO₂/alkaline-earth-metal-oxide systems takes place in the molten state.

The network connectivity of magnesium- and magnesium/calcium modified silicon oxycarbides has been calculated in order to compare the influence of network structure on their bioactivity [66]. Based on the solid-state NMR investigation from the present work, the network connectivity of the prepared samples can be calculated using equation (4-1), which considers the incorporated Ca as network modifier and boron as network former:

$$NC = [Si] \times ([4 \times f(Q^4)] + [3 \times f(Q^3)] + [2 \times f(Q^2)] + [1 \times f(Q^1)] + [6 \times f(SiO_3C)] + [8 \times f(SiO_2C_2)] + [10 \times f(SiOC_3)] + [12 \times f(SiC_4)]) + [B] \times ([3 \times f(BO_3)] + [5 \times f(BO_2C)] + [7 \times f(BOC_2)]) \quad (4-1)$$

with [Si] and [B] being the Si and B atomic fractions among total network formers and $f(x)$ the site fraction of the corresponding species x from the experimental NMR data. The calculated network connectivity values are summarized in Table 4-3.

Table 4-3. Network connectivity value NC calculated based on NMR data; the value of vitreous silica SiO₂ is given for the sake of comparison.

Sample	SiO ₂	SiOC	SiOC-B7	SiOC-Ca5	SiOC-B7Ca5	SiOC-Ca12
NC	4.0	5.95	4.95	5.59	5.55	5.24

Table 4-4. Elemental contents, empirical formulae and estimated phase compositions of the prepared Si(B,Ca)OC samples.

Sample	Si (wt.%)	O (wt.%)	C (wt.%)	Ca (wt.%)	B (wt.%)	Empirical Formulae	Estimated Phase Composition
SiOC	46.88	39.18	13.94	-	-	$\text{Si}_{11}\text{O}_{1.47}\text{C}_{0.70}$	$\text{Si}_{11}\text{O}_{1.47}\text{C}_{0.27}$ / 0.43 C
SiOC-B7	45.16	42.34	11.54	-	0.955	$\text{Si}_{11}\text{B}_{0.055}\text{O}_{1.64}\text{C}_{0.60}$	$\text{Si}_{11}\text{B}_{0.055}\text{O}_{1.64}\text{C}_{0.22}$ / 0.38 C
SiOC-Ca5	43.73 ^a	38.63	14.52	3.12 ^a	-	$\text{Si}_{11}\text{Ca}_{0.05}\text{O}_{1.55}\text{C}_{0.77}$	0.983 $\text{Si}_{11}\text{Ca}_{0.034}\text{O}_{1.53}\text{C}_{0.25}$ / 0.017 CaSiO_3 / 0.52 C
SiOC-B7Ca5	42.95	40.61	12.61	2.86	0.975	$\text{Si}_{11}\text{B}_{0.059}\text{Ca}_{0.05}\text{O}_{1.65}\text{C}_{0.69}$	0.988 $\text{Si}_{11}\text{B}_{0.060}\text{Ca}_{0.038}\text{O}_{1.63}\text{C}_{0.24}$ / 0.012 CaSiO_3 / 0.45 C
SiOC-Ca12	40.05 ^a	37.68	15.41	6.86 ^a	-	$\text{Si}_{11}\text{Ca}_{0.12}\text{O}_{1.65}\text{C}_{0.90}$	0.932 $\text{Si}_{11}\text{Ca}_{0.056}\text{O}_{1.56}\text{C}_{0.26}$ / 0.068 CaSiO_3 / 0.66C

^a: Si and Ca contents are calculated from Ca/Si molar ratios given in Table 3-1.

The carbon for oxygen substitution in silicate network leads to an extreme increase of the network connectivity, as carbon is tetravalent and acts as a corner-linking “node” for four $\text{SiO}_x\text{C}_{4-x}$ tetrahedra, whereas bridging oxygens link only two tetrahedra. Thus, the exchange of ca 13.5 at.% oxygen by carbon in the silicate network (which corresponds to the composition $\text{SiO}_{1.47}\text{C}_{0.27}$ in SiOC) leads to an increase of the network connectivity from 4 (as for SiO_2) to 5.95 [51, 66].

The incorporation of boron into the silicon oxycarbide network has been shown to repel carbon from the network, leading to a significant decrease in the network connectivity. Thus, the network connectivity of SiOC-B7 is 4.95. Also, the incorporation of Ca into the silicon oxycarbide network leads to a decrease of the network connectivity. Correspondingly, SiOC-Ca5 and SiOC-Ca12 show network connectivity values of 5.59 and 5.24, respectively. However, the decrease of the network connectivity upon Ca modification is related to both the generation of Q^3 sites (*i.e.*, depolymerization of the network) and the decrease of the carbon content in the network. The increase of Ca amount reduces the network connectivity value further though also increases the amount of crystalline secondary phase (wollastonite / pseudowollastonite) as shown by the increased fraction of Q^2 sites. As discussed above, this effect relies on the partitioning of the Ca-containing silicon oxycarbide systems into a calcium-poor matrix and calcium-rich crystalline phase, similar to the behavior of SiO_2 -CaO systems lying in the compositional miscibility gap.

The results presented here indicate that the network connectivity in silicon oxycarbides can be influenced / finely tuned by using two different tools: (i) changing the carbon content of the network and (ii) introducing network depolymerization, similar to the silicate-based systems. It is expected that the two ways of modifying the network connectivity in amorphous silicon oxycarbides will have different effects on their bioactivity. Additionally, the *in situ* generation of highly bioactive / biodegradable phases (such as wollastonite or pseudowollastonite in the present study) embedded within a bioinert matrix (such as silicon oxycarbide) may be considered as a convenient preparative access to interesting phase compositions with tailored bioactivity. This concept was recently shown, *e.g.*, for silica-bonded calcite prepared from CaCO_3 -filled silicones [205, 206].

4.1.3. Ion release kinetics upon SBF exposure

In vitro SBF assessment results of silicon oxycarbide based samples have been compared to that of the commercial Vitryxx® Bioactive Glass with 45S5 composition, *i.e.*, with the chemical composition of $\text{Si}_1\text{Na}_{1.06}\text{Ca}_{0.58}\text{P}_{0.11}\text{O}_{3.39}$ and a network connectivity value of 2.10 [89]. This glass sample will be denoted as 45S5 in the following work.

As shown in Table 4-5, the mean particle sizes, d_{50} , of the silicon oxycarbide based samples are comparable. N_2 adsorptions isotherms (not shown here) are type II for both 45S5 and the prepared silicon oxycarbide based samples, indicating that they are non-porous or macroporous materials [207]. The BET SSA values and total pore volume calculated for the silicon oxycarbide based samples and 45S5 were shown to be relatively low and comparable (see Table 4-5). As the SSA values are only 10-30 m^2/g , it is assumed that the influence of the SSA on the bioactivity behavior of these materials is negligible. Consequently, differences in the bioactivity of the studied samples can be correlated exclusively to their chemical and phase composition as well as network architecture.

Table 4-5. Mean particle size d_{50} , BET specific surface area (SSA) analysis and total pore volume of silicon oxycarbide based samples and 45S5.

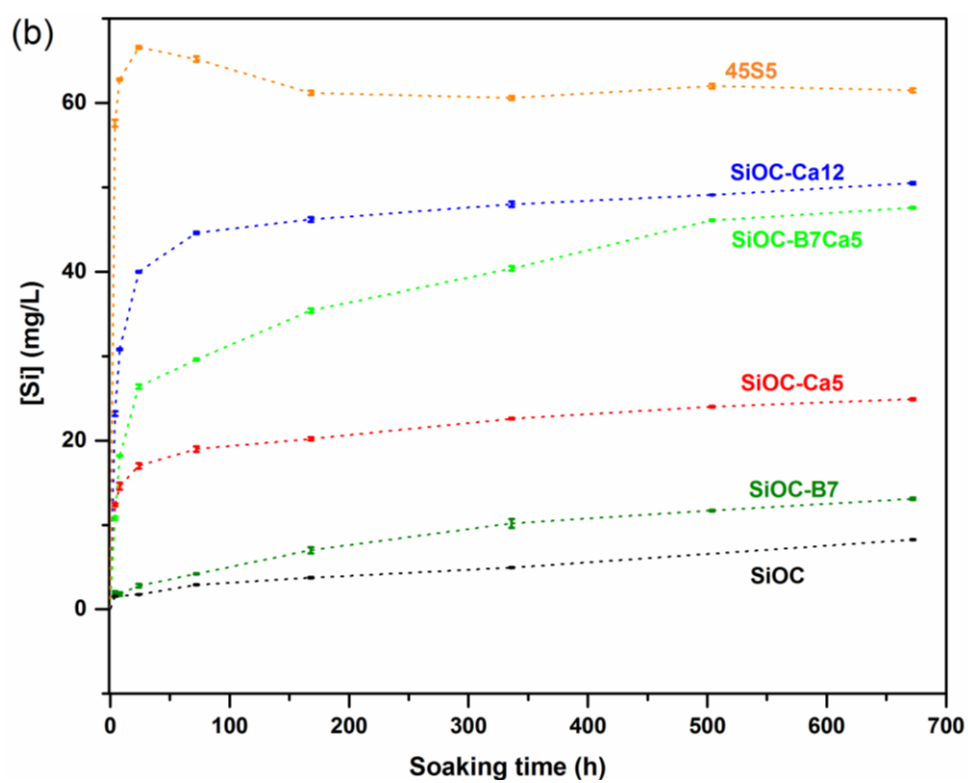
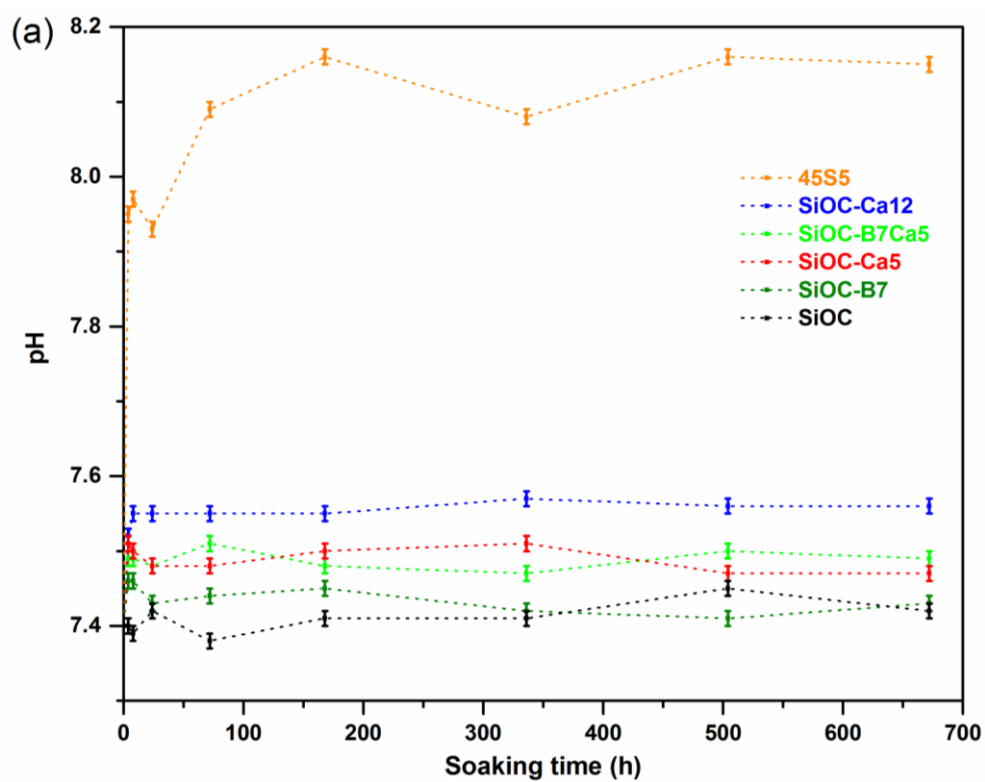
Sample	SiOC	SiOC-B7	SiOC-B7Ca5	SiOC-Ca5	SiOC-Ca12	45S5
d_{50} [μm]	10.0	16.0	20.3	16.5	27.9	6.5
BET SSA [m^2g^{-1}]	19.9	26.7	15.6	10.1	21.0	18.9
Total pore volume [cc/g]	4.2×10^{-2}	6.5×10^{-2}	6.5×10^{-2}	4.6×10^{-2}	4.5×10^{-2}	3.7×10^{-2}

The prepared silicon oxycarbide based samples were exposed to simulated body fluid (SBF) for different soaking time periods. Subsequently, the pH evolution of the SBF solutions with soaking time was assessed. As it is observed in Figure 4-8 (a), the pH value of the SBF solutions increases with soaking time due to the ion exchange at the surface of the samples occurring between the protons in solutions and the cations (*e.g.*, Ca^{2+}) in the samples [208]. The soaking of SiOC does not change the pH value of the SBF solution noticeably, while the SBF solutions for the other investigated samples show pH increases to different extents. The exposure of 45S5 to SBF leads to the highest pH value in the solution, *i.e.*, higher than 8.0. Especially at the early stages of the SBF exposure of 45S5, the increase of the pH value is steep and has been associated with a cytotoxic effect of 45S5 within this time frame [209]. The

silicon oxycarbide samples modified with Ca and/or B lead to only slight increases of the pH values of the SBF solutions. As the SBF is a solution saturated with Ca and P [210], the pH increase in SBF solutions is expected to improve the precipitation of Ca, and thus the formation of calcium phosphate, resulting in an enhanced bioactivity [211]. Even if cytotoxicity studies were not conducted here, the fact that the pH of the medium does not change to critical values (in comparison to 45S5 glass) indicates that the silicon oxycarbide based samples investigated in the present study should not lead to cell death due to alkalization of the medium (as mentioned in section 2.2.1). Indeed, previous reports on Ca- and Mg-containing silicon oxycarbides have revealed their high compatibility with cells such as L-929, HEK-293 or MEF [19, 21]. On the other hand, the bioactivity of the silicon oxycarbide based materials is expected to be lower than that of 45S5 glass.

At the early stages of the SBF exposure, the Ca concentration in SBF solutions increases, as Ca is released from the samples (*i.e.*, as for SiOC-B7Ca5, SiOC-Ca5, SiOC-Ca12, 45S5, see Figure 4-8 (c)). Interestingly, the Ca concentration in the SBF solution of the Ca-containing silicon oxycarbide samples decreases for longer soaking time, while it remains stable for 45S5. The P concentration in the SBF solutions decreases rapidly for all samples, reaching values lower than 5 mg/l for SiOC-B7Ca5, SiOC-Ca5, SiOC-Ca12 and 45S5 after 1 week, as shown in Figure 4-8 (d). This has been attributed to the precipitation of calcium phosphate on the sample surface and thus correlates to its bioactivity.

Arcos *et al.* [212] calculated the activation energy for Si release in melt and sol-gel derived silicate glasses and considered this as a parameter to evaluate their bioactivity. Correspondingly, it was shown that activation energies for Si release with values lower than 0.2 eV correlate to high bioactivity, whereas values larger than 0.5 eV are characteristic for non-bioactive silicate glasses. Intermediate values, *i.e.*, between 0.35 and 0.5 eV, represent the boundary between bioactive and non-bioactive silicate-based glasses [212].



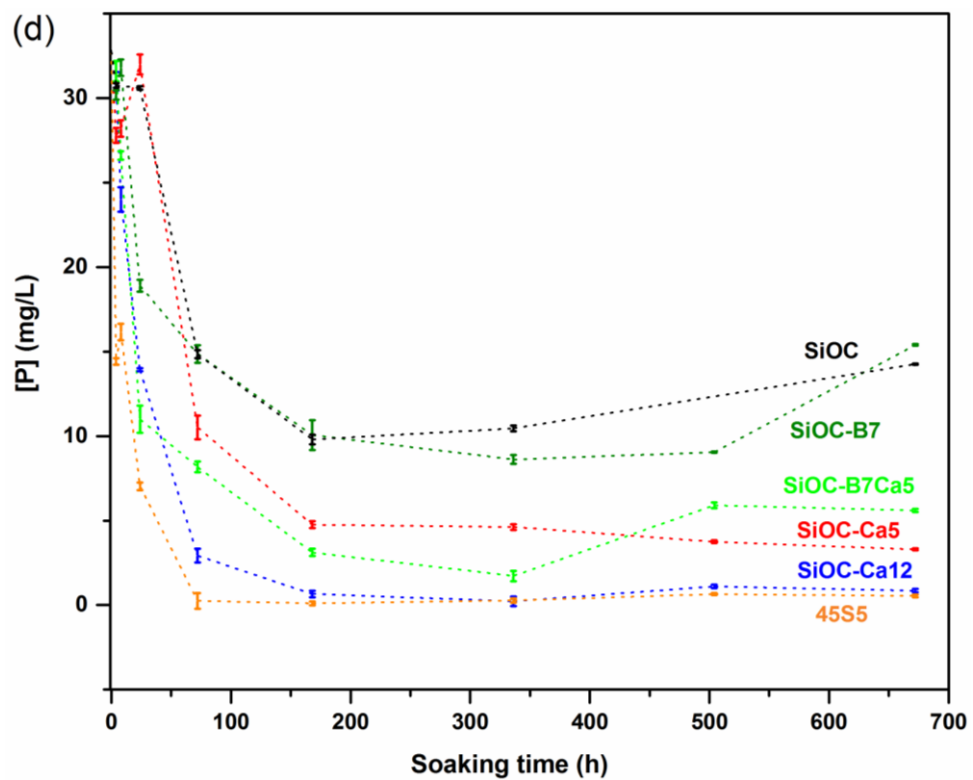
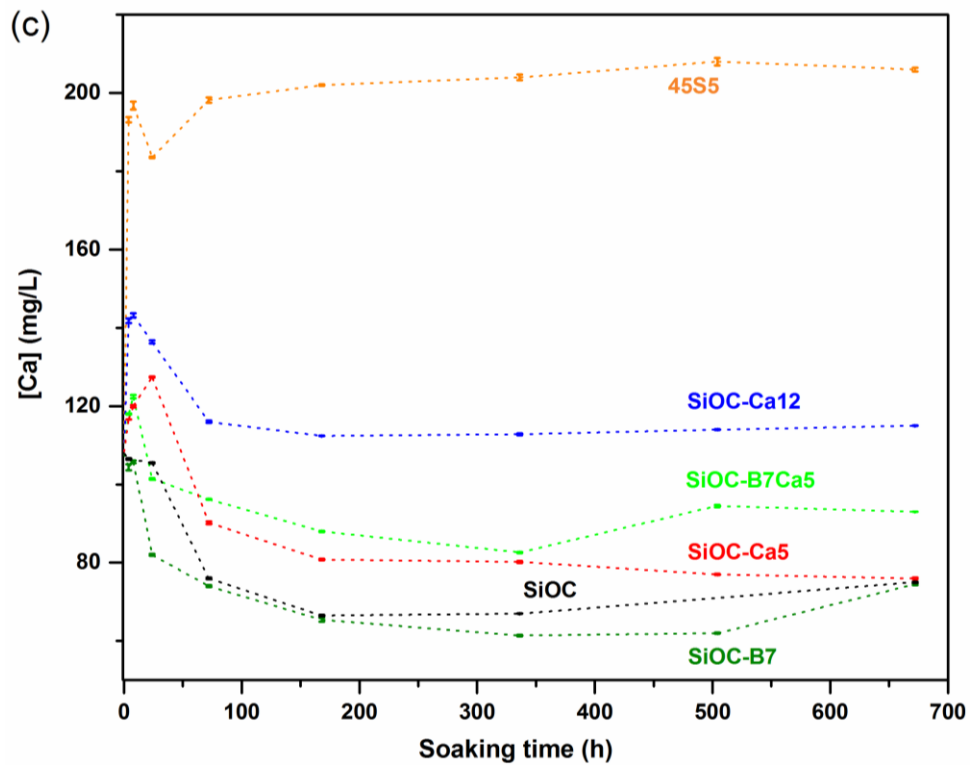


Figure 4-8. Evolution of (a) pH value, (b) Si concentration, (c) Ca concentration, (d) P concentration of the filtered SBF solutions as a function of the soaking time for silicon oxycarbide based and 45S5 samples. (The ion concentrations of Si, Ca and P were measured by Dipl.-Geol. Christian Scholz)

In the present work, the activation energy for the Si release of silicon oxycarbide based and 45S5 samples was assessed upon considering the Si concentration in the SBF solution after 72h exposure to the simulated body fluid at three temperatures, *i.e.*, 24, 37 and 55 °C. The Arrhenius plot of the data according to equation (4-2):

$$\ln([Si]) = C - E_a/RT \quad (4-2)$$

where $[Si]$ is the concentration of Si in the SBF solution, C is a constant, R the universal constant of gas and T the absolute temperature, is shown in Figure 4-9.

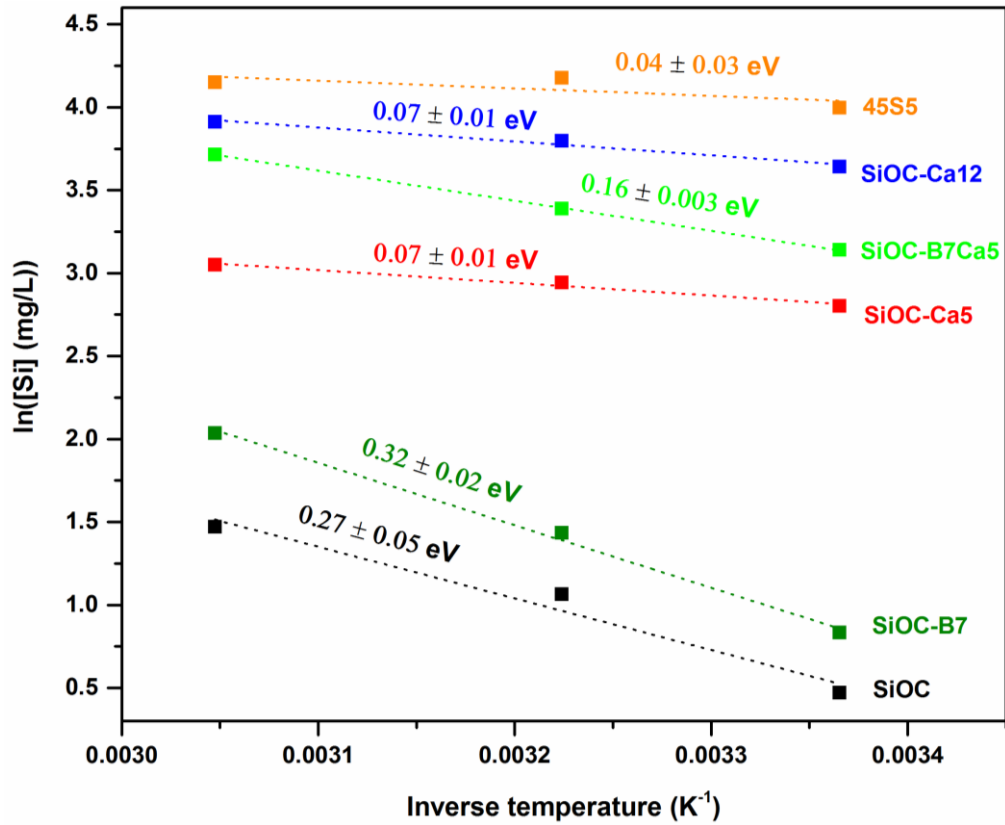


Figure 4-9. Arrhenius plots of silicon release after 3 days SBF testing at 24 °C, 37 °C and 55 °C for the investigated samples.

In Figure 4-9, there are two groups among the assessed samples: firstly, SiOC and SiOC-B7 show relatively large activation energies for Si release, *i.e.*, 0.27 and 0.32 eV, respectively; whereas 45S5 and SiOC-Ca5/SiOC-Ca12 exhibit significantly lower values for E_a , *i.e.*, 0.04 and 0.07 eV, respectively. Sample SiOC-B7Ca5 shows with 0.16 eV an intermediate value for the activation energy. The incorporation of boron into the silicon oxycarbide network is shown to not affect significantly the activation energy for Si release; whereas the Ca modified materials SiOC-Ca5 and SiOC-Ca12 have E_a values which are

similar to that of 45S5. Consequently, it may be expected that SiOC-Ca5 and SiOC-Ca12 exhibit high bioactivity (at least higher than that of SiOC and SiOC-B7). This correlates to the Si and Ca release kinetics of the samples (see Figure 4-8).

4.1.4. Biomineralization upon SBF exposure

The formation of surface charges when the silicon oxycarbide based samples as well as 45S5 glass (before and after 4 h and 8 h SBF test) are dispersed in water ($\text{pH} \approx 5.0$) was estimated by determining their zeta potential. As shown in Figure 4-10 (a), all silicon oxycarbide based samples and 45S5 have negative surface charges, resulting from the dissociation of surface silanol groups (Si-OH) to Si-O^- at pH values higher than the isoelectric point of silica, which is $\text{pH} = 1.6$ as reported by Fisher *et al* [213, 214]. Since SiOC has Si-O, Si-C and C-C bonds, the surface charge of SiOC can be estimated by the surface charges of silica, SiC and graphite, which have zeta potential values of ca. -40 mV, -25 to -40 mV and -45 mV at $\text{pH} = 5.0$, respectively [214-216]. Correspondingly, the zeta potential of SiOC before SBF test was measured to be ca. -38 mV (see Figure 4-10 (a)). Interestingly, 45S5 has zeta potential of -39 mV, close to -40 mV of silica at $\text{pH} = 5.0$, despite of its high content of Ca^{2+} and Na^+ , which could be correlated to the fast formation of silica-based hydrated surface layer during the measurement [217]. In contrary, the as-prepared Ca/B modified silicon oxycarbides have zeta potential values between -28 and -36 mV, showing a positive shift compared to that of SiOC. Ca-containing species such as calcium silicate hydrate have zeta potential values that are less negative than that of silica, and boron carbide with B-C bonds that also exist in B modified silicon oxycarbide, shows positive zeta potential at $\text{pH} = 5.0$, indicating the positive shift to be related to the incorporated Ca and B on particle surfaces [218, 219].

After 4 h and 8 h SBF test, the change of surface charge, *i.e.*, zeta potential, of 45S5 and silicon oxycarbide based samples showed different tendencies. In Figure 4-10 (a), three different groups can be distinguished: (i) SiOC-Ca12 and 45S5, showing a decrease in their absolute zeta potential value and reaching a value similar to that of reference synthetic hydroxyapatite powder upon 8 h SBF exposure, (ii) SiOC-B7, SiOC-B7Ca5 and SiOC-Ca5 with an increase of their absolute zeta potential value, and (iii) SiOC with practically no or little change in the zeta potential. The shifting of zeta potential towards that of hydroxyapatite implies that the formation of calcium phosphate-like substance may have happened on SiOC-Ca12 and 45S5 surface after 8 h test. The shift of zeta potential towards negative value for SiOC-B7, SiOC-B7Ca5 and SiOC-Ca5 suggests the leaching of surface B and Ca ions and the

formation of hydrated silica surface layer, which is beneficial for the nucleation of hydroxyapatite during the SBF exposure, since the more negative the surface of the glass samples, the stronger its tendency to attract Ca^{2+} cations.

Therefore, the evolution of zeta potential with soaking time can be illustrated in Figure 4-10 (b): 45S5 and silicon oxycarbide based samples all experienced a surface activation process, which was followed by the precipitation of hydroxyapatite on the surface. However, the surface activation on 45S5 and SiOC-Ca12 were very fast, so that zeta potential shifted positively due to hydroxyapatite precipitation already after 4 h, while the hydrated silica layer was still forming on the surfaces of SiOC-B7, SiOC-Ca5 and SiOC-B7Ca5 after 8 h, leading to a negative zeta potential shift. Thus, all investigated samples may exhibit the same behavior concerning their surface evolution when exposed to SBF conditions, *i.e.*, firstly generating a silica gel layer upon leaching of species into SBF, followed by hydroxyapatite precipitation. This evolution can be rationalized by considering the evolution of the zeta potential of the samples which in the first step goes towards the value of silica gel (*ca.* -40 mV) and then increases towards the value of HA (*ca.* -21 mV). The difference between the investigated samples relies on the time scale in which the materials go through the mentioned stages: 45S5 and SiOC-Ca12 show very fast formation of silica gel and HA, and consequently their zeta potential measured after 4 and 8 h of SBF test reflects the formation of hydroxyapatite on their surface. Unlike 45S5, the measurements of the zeta potential after 4 and 8 h SBF test indicate that SiOC-B7, SiOC-B7Ca5 and SiOC-Ca5 are still within the stage of silica gel formation (and thus no HA precipitation on the surface yet occurred). Finally, SiOC is found to be the most sluggish sample, with the surface being not significantly altered within the first 8 h of SBF exposure. However, it is expected that SiOC would show same behavior like that of the Ca modified samples, *i.e.*, silica gel formation and HA precipitation, though in a significantly larger time frame. This is in agreement with observations made in literature, which showed the silicon oxycarbide materials with similar chemical compositions were exhibiting HA mineralization upon 5 weeks of SBF exposure [20].

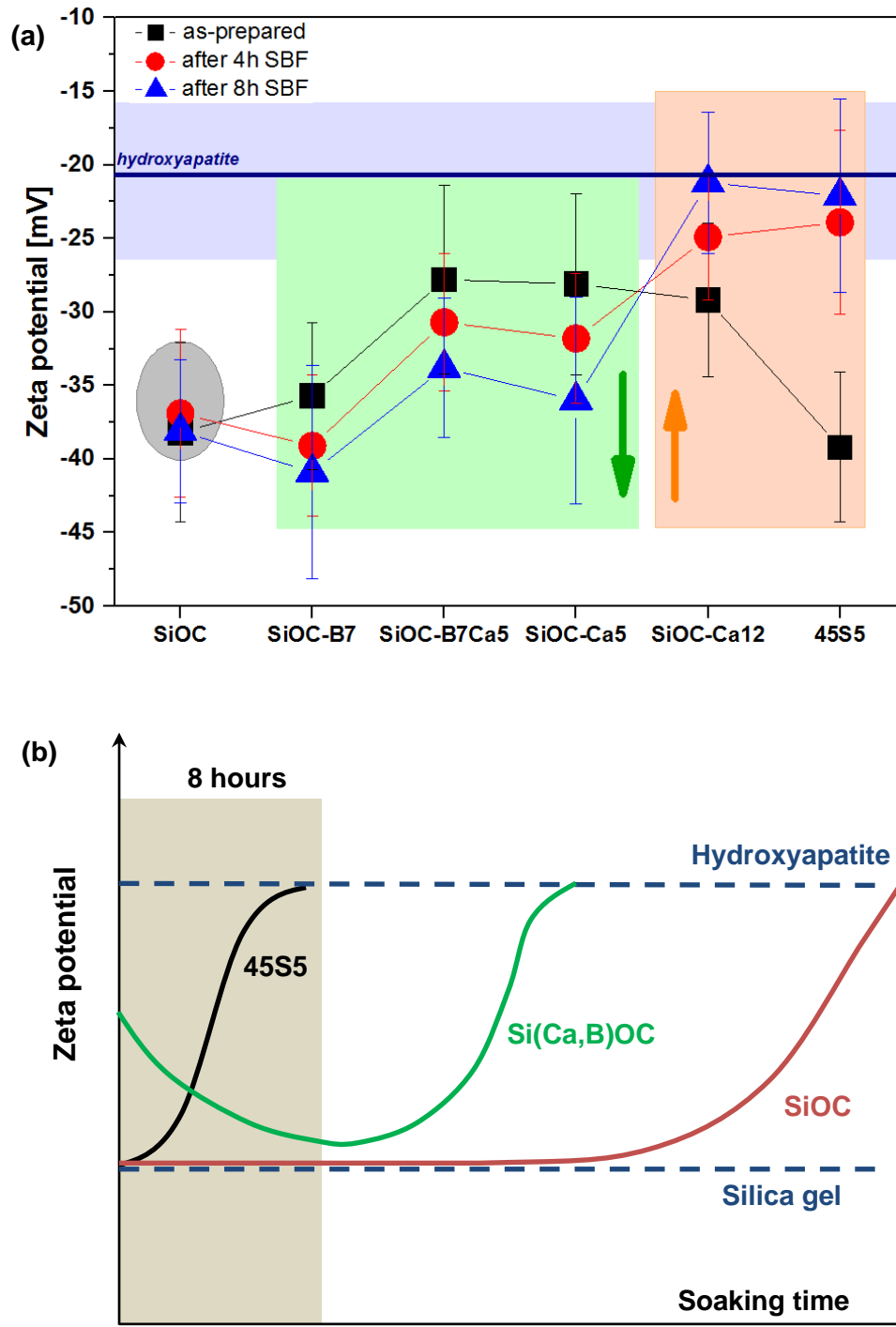


Figure 4-10. (a) Evolution of surface charge during the first 8 h of the SBF test, measured on zeta potential of particles in deionized water (pH ≈ 5.0), for SiOC, SiOC-B7, SiOC-B7Ca5, SiOC-Ca5, SiOC-Ca12 and 45S5; (b) Schematic illustration of zeta potential evolution with soaking time during the SBF test for 45S5, Si(Ca,B)OC and SiOC. Shaded region refers to the first 8 h of soaking, during which the zeta potential was measured in the present study. It is seen, that the samples are assumed to show the same evolution concerning their zeta potential, i.e., approaching in a first step the zeta potential value of silica (gel) and subsequently evolving towards the value of HA. The difference between the samples relies only (and mainly) on the different time needed to develop the HA precipitates on their surface.

The samples exposed to SBF for 4 weeks were characterized by means of X-ray diffraction (see Figure 4-11 (b)). The XRD patterns indicate that all soaked samples are X-ray amorphous, exhibiting a low intensity reflection at a 2-theta value of ca. 14.5° , which was assigned to the (211) reflection of hydroxyapatite (HA) and carbonated hydroxyapatite (HCA) [220, 221]. Interestingly, a comparison with XRD patterns of the samples before SBF soaking (see Figure 4-11 (a)) shows that the small amounts of wollastonite / pseudowollastonite secondary phases present in some samples (e.g., SiOC-Ca5) have disappeared after SBF soaking. The vanishment of wollastonite / pseudowollastonite from the XRD patterns of the samples could be confirmed as early as 3 days of SBF soaking (XRD patterns not shown here). Most probably, the release kinetics of these phases, which consist mainly of Q^2 sites, is relatively fast during the SBF test. The question, whether and to which extent the presence and fast dissolution of wollastonite / pseudowollastonite influence the bioactivity of the investigated Si(B,Ca)OC samples, will be critically considered in the present study.

FTIR spectra in Figure 4-12 (a) for samples before SBF soaking show Si-O-Si vibrations at 470, 1083 and 1220 cm^{-1} for silicon oxycarbides, and at 500 cm^{-1} and 1035 cm^{-1} for 45S5. The shifting of Si-O-Si absorption in 45S5 is related to Na^+ and Ca^{2+} presence in glass network. And a strong absorption of Si- O_{NBO} (non-bridging-oxygen) can be observed in 45S5 [222, 223]. Additionally, B-O vibration at 1415 cm^{-1} can be observed for the B modified silicon oxycarbides SiOC-B7, SiOC-B7Ca5 [196].

After 4 weeks SBF test, absorption bands of tetrahedral PO_4^{3-} groups at 605, 565 and 1030 cm^{-1} can be identified in Figure 4-12 (b), which demonstrates calcium phosphate mineralization [89]. These absorption bands are most significant for 45S5, followed by SiOC-Ca12. The other silicon oxycarbide samples, *i.e.*, SiOC, SiOC-Ca5, SiOC-B7Ca5 and SiOC-B7, show similar FTIR spectra after 4 weeks of SBF test, in which the existence of PO_4^{3-} is verified mainly by the absorption band at 1030 cm^{-1} . It is also interesting to notice that after 4 weeks of SBF exposure, CO_3^{2-} vibrations at 875, 1420 and 1460 cm^{-1} can be observed for 45S5 [224], though not for the silicon oxycarbide based samples. Thus, calcium phosphate precipitation on 45S5 can be assigned to carbonated hydroxyapatite (HCA); whereas the precipitation on all silicon oxycarbide based samples seems to be rather hydroxyapatite (HA). This difference can be explained by the much higher pH increase during the SBF exposure of 45S5 as compared to that of silicon oxycarbides, since high pH value favors the carbonate precipitation [225].

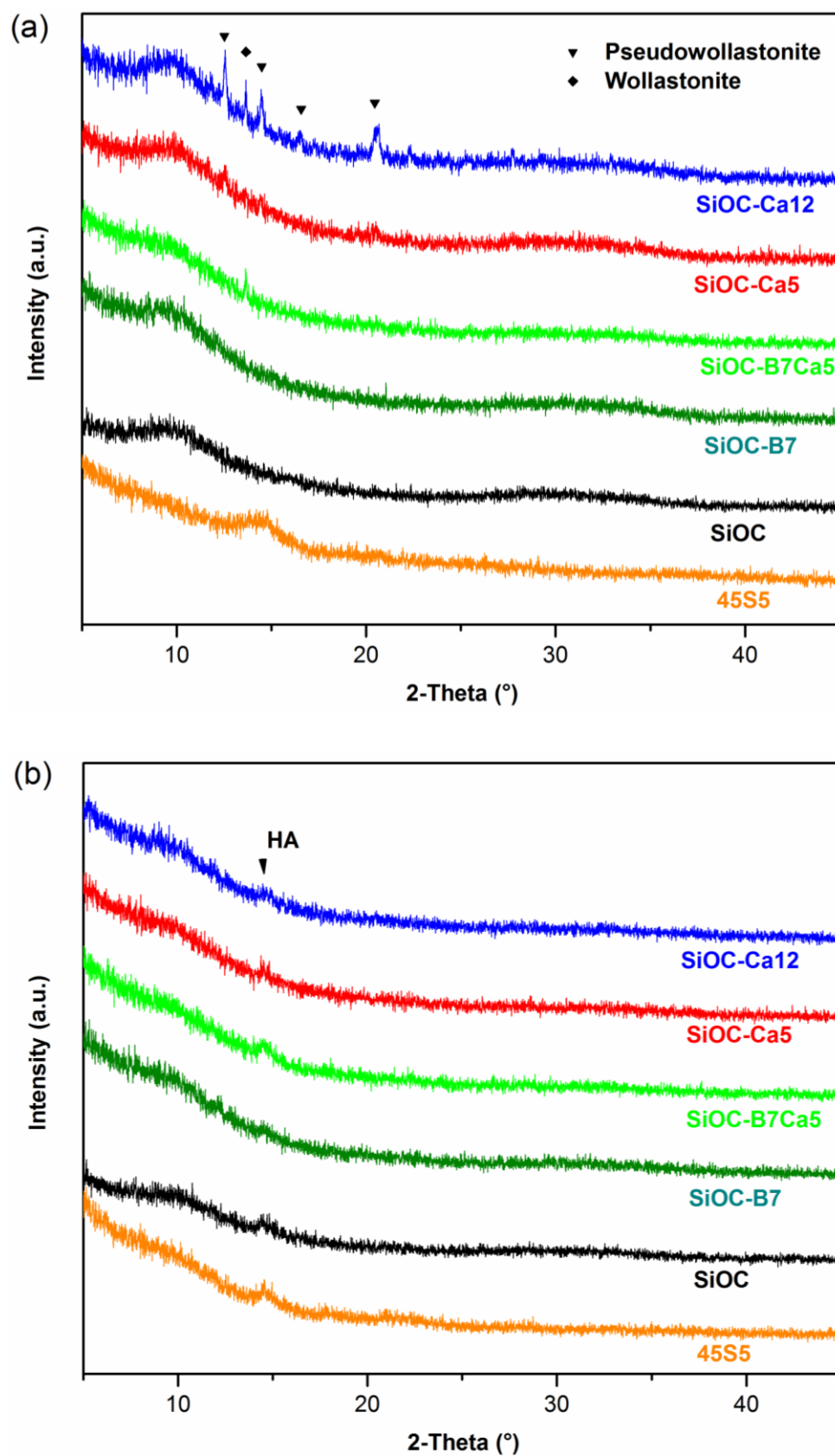


Figure 4-11. XRD diffractograms of silicon oxycarbide based and 45S5 samples (a) before SBF soaking and (b) after 4 weeks soaking in SBF.

A comparison between the FTIR spectra of SiOC-B7 and SiOC-B7Ca5 before and after SBF exposure (see Figure 4-12) reveals furthermore that the absorption band for B-O vibration is significantly weakened after the SBF test, indicating the release of B into the SBF solution. However, the investigation of the possible angiogenesis effect of such B release, as mentioned in 2.2.2, is not included in the present study.

The observation from XRD and FTIR analysis proves the formation of (carbonated) hydroxyapatite (HCA/HA) on all investigated systems after 4 weeks SBF test, and this formation is responsible for the decrease of P and Ca concentrations during SBF tests as shown in Figure 4-8. Therefore, the prepared silicon oxycarbide systems are considered to be bioactive. However, the observed XRD and FTIR signals for HA or HCA on silicon oxycarbide samples are significantly lower than that of 45S5 and other silicate based bioactive glasses [222, 226]. This is related to the limited amount of phosphate available for the investigated silicon oxycarbides, as shown by the rapid decrease of P concentration in the SBF solution (see Figure 4-8 (d)); while 45S5 contains itself phosphate, in addition to that provided by the SBF solution. Under static SBF test condition, which means that SBF solution is not circulated with an external reservoir to keep Ca and P concentration stable [210], the phosphate deposition on the investigated silicon oxycarbides is limited, while the P release from 45S5 can continuously support this process. Therefore, XRD and FTIR techniques may not be sensitive enough to reveal the onset of the hydroxyapatite deposition on the surface of the silicon oxycarbide based samples.

The hydroxyapatite formation on the surface of the studied silicon oxycarbide based samples was also assessed by using scanning electron microscopy (SEM). As shown in Figure 4-13, the precipitation of HA on 45S5 can be observed after one day, which is in good agreement with results reported in literature [89], while the biomineralization process on SiOC needs significantly longer time, *i.e.*, *ca.* 4 weeks. The modification of the silicon oxycarbide network with boron (as for SiOC-B7) leads to a decrease of the HA formation onset time from 4 weeks to 3 weeks; whereas, the incorporation of Ca is shown to significantly accelerate the HA mineralization. Correspondingly, HA was detected by SEM on SiOC-Ca5 and SiOC-Ca12 after one week and three days of SBF exposure, respectively (see Figure 4-13), in agreement with the ion release kinetics shown in Figure 4-8.

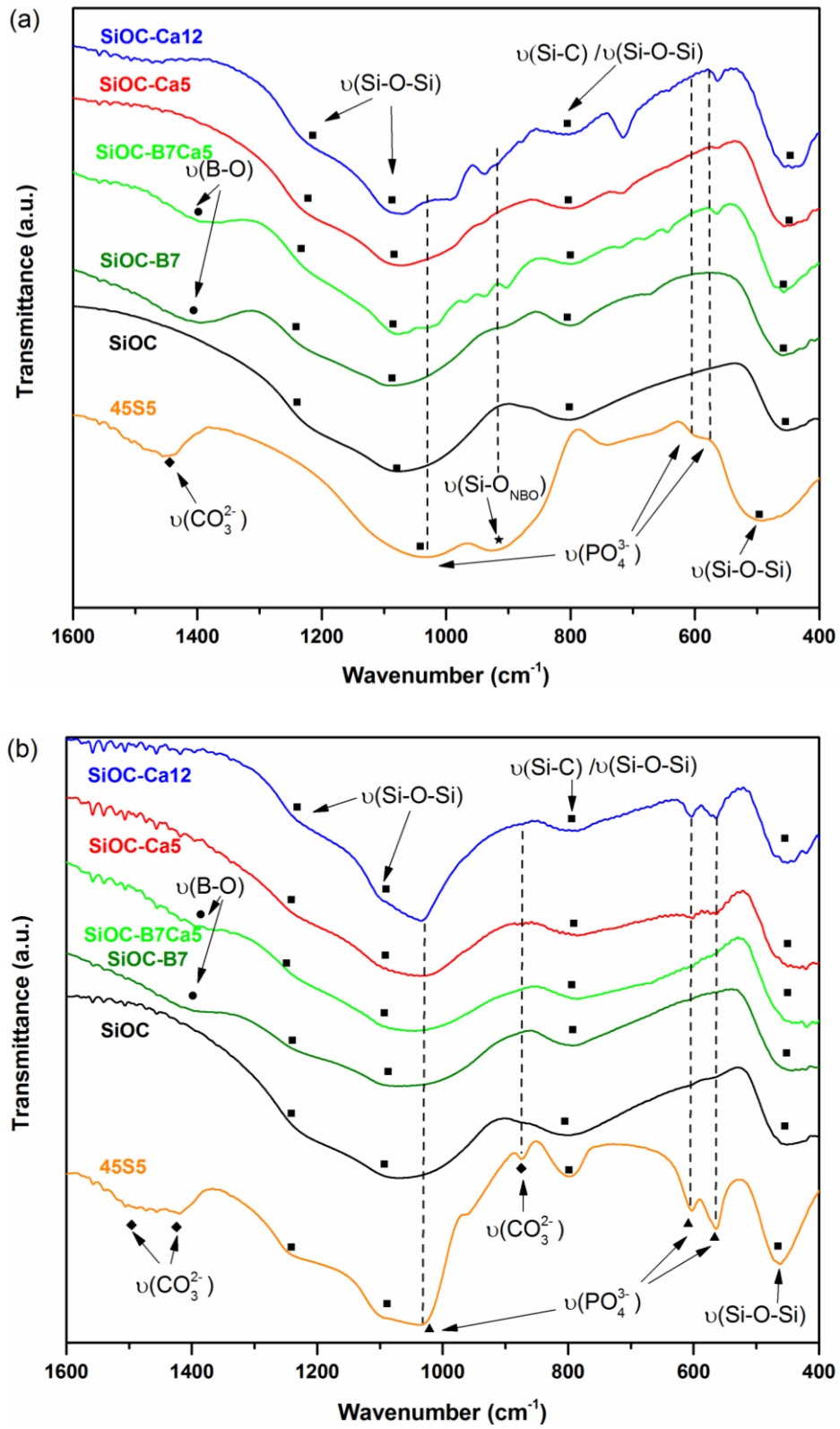


Figure 4-12. FTIR spectra of silicon oxycarbide based and 45S5 samples (a) before SBF soaking and (b) after 4 weeks soaking in SBF.

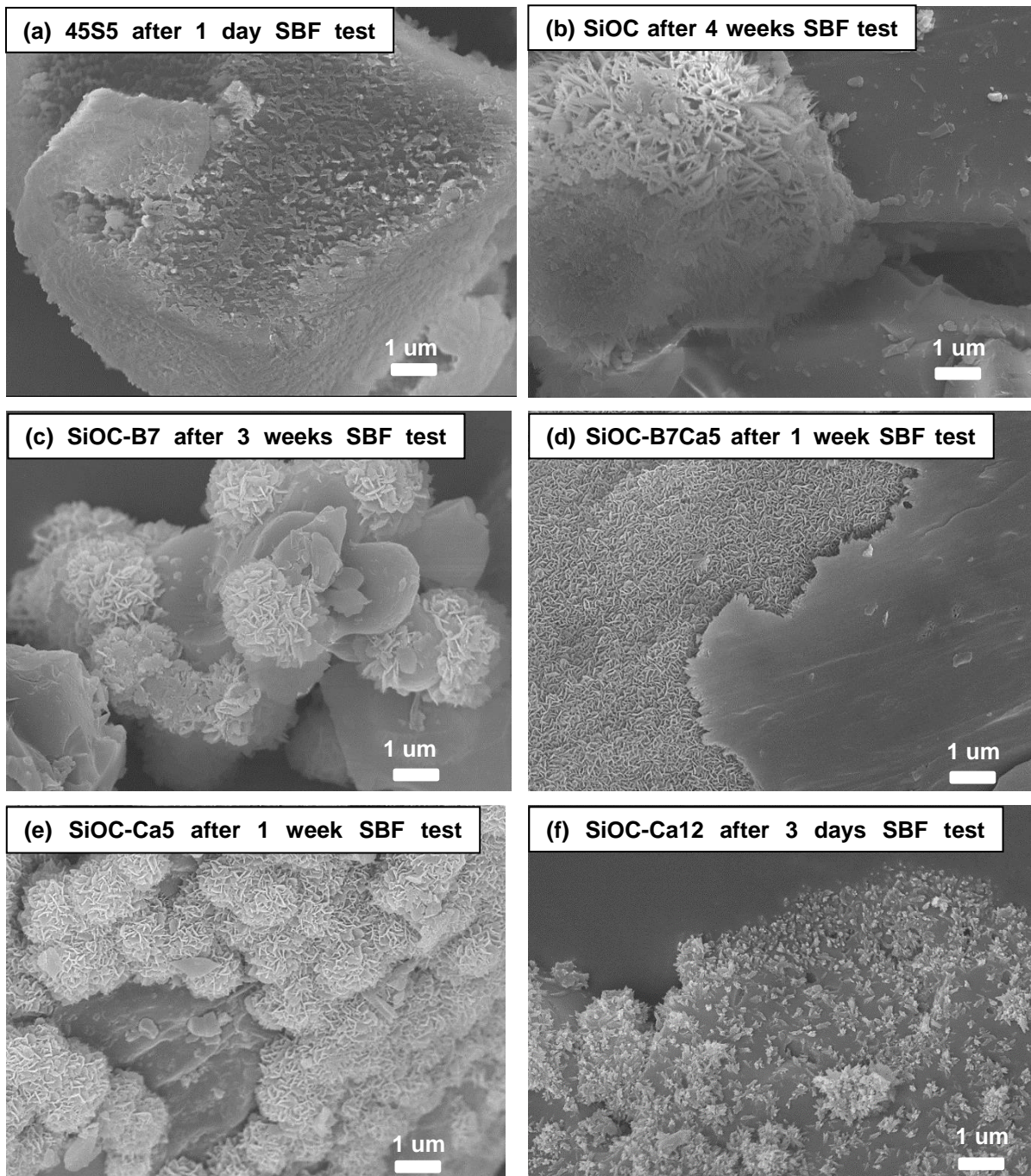


Figure 4-13. SEM micrographs obtained at the earliest time points of the individual samples to visually detect hydroxyapatite formation after SBF exposure.

4.1.5. Structure-bioactivity correlation

It is obvious that the network connectivity of all silicon oxycarbide based samples is significantly higher than that of 45S5 glass, due to the incorporation of sp^3 bonded carbon in the glass network, as mentioned above. Moreover, various Raman spectroscopic studies have confirmed carbon D and G vibration modes in polymer derived silicon oxycarbides, and these vibrations are correlated to sp^2 bonded carbon with defects [40, 52]. The fractions of this so-called “free” sp^2 carbon in silicon oxycarbide based samples in the present study have been estimated in Table 4-4. Since carbon materials are bioinert [227], the influence of the “free” carbon content in silicon oxycarbide based samples on bioactivity behavior will not be considered in the present study.

The prepared silicon oxycarbide based samples (SiOC and Si(B,Ca)OC) were found to be mainly X-ray amorphous, as shown in Figure 4-4. Only small amounts of wollastonite and/or pseudowollastonite were detected in the Ca-containing samples, mainly in SiOC-Ca12. It can be seen in Table 4-4, that the amount of secondary silicate phase (wollastonite / pseudowollastonite) in the prepared samples is relatively low. For instance, the molar ratio $\text{Si}_{\text{wollastonite/pseudowollastonite}} : \text{Si}_{\text{silicon oxycarbide glass}}$ in SiOC-Ca5 and SiOC-Ca12 was 1.73 : 100 and 7.30 : 100, respectively.

The *in vitro* bioactivity assessment results showed that ternary silicon oxycarbide (SiOC) is a bioactive material. Ca incorporation increases the bioactivity of SiOC significantly, as shown for SiOC-B7Ca5, SiOC-Ca5 and SiOC-Ca12. This Ca effect on bioactivity is related to the unique microstructure and phase compositions of the Ca modified silicon oxycarbides. The incorporation of Ca in silicon oxycarbide reduces the network connectivity of the silicon oxycarbide network on the one hand (see Table 4-3), and leads to the formation of small amounts of calcium silicate (pseudowollastonite / wollastonite) on the other hand.

In order to separate these two effects, SiOC-B7Ca5 and SiOC-Ca5/SiOC-Ca12 are compared. SiOC-B7Ca5 has a higher Si release activation energy (*i.e.*, 0.16 eV) than that of SiOC-Ca5/SiOC-Ca12 (*i.e.*, 0.07 eV, see Figure 4-9); however, the amount of released Si in the case of SiOC-B7Ca5 is higher than that of SiOC-Ca5 (see Figure 4-8 (b)). This inconsistency reveals different contributions of two possible release paths for Si in SiOC-B7Ca5, either from the secondary calcium silicate phase (wollastonite / pseudowollastonite) or from the amorphous silicon oxycarbide network. Since the activation energy for silicon release of SiOC-Ca5/SiOC-Ca12 (0.07 eV) is similar to that of calcium silicate (0.09 eV, as for α - and β -calcium silicate in Tris buffer solution [14]), the Si release in SiOC-Ca5/SiOC-Ca12 is shown to

be dictated by the crystalline calcium silicate phase; while in the case of SiOC-B7Ca5 the Si release is mainly determined by the silicon oxycarbide glass network. Therefore, crystalline calcium silicate phase has stronger influence on bioactivity for SiOC-Ca5/SiOC-Ca12, *i.e.*, silicon oxycarbide with only Ca modification, than for SiOC-B7Ca5, *i.e.*, silicon oxycarbide with both Ca and B modification.

Table 4-6. Average Si release rates (values normalized to Si content in amorphous silicon oxycarbide network) between 3 days and 4 weeks soaking time.

Sample	SiOC	SiOC-B7	SiOC-B7Ca5	SiOC-Ca5	SiOC-Ca12
Si average release rate (%/h)	0.0013	0.0022	0.0047	0.0015	0.0017

Meanwhile, the Si release for Ca modified Si(B,Ca)OC samples in Figure 4-8 (b) shows a strong increase in the first 3 soaking days, but slows down and has a linear-like behavior from 3 days to 4 weeks. Due to the fact that crystalline calcium silicate was not detectable anymore after 3 days of SBF soaking, the rapid increase of the Si concentration in the SBF solution at the beginning of the SBF test is related to the dissolution of crystalline calcium silicate phase, and is corroborated by the low Si release activation energies for SiOC-Ca5/SiOC-Ca12. The average Si release rates from silicon oxycarbide network between 3 days and 4 weeks can be compared by normalizing the released Si amounts in this time period to the total Si amounts in the amorphous network, which were calculated from the chemical and phase compositions in Table 4-4. The results are summarized in Table 4-6.

The average Si release rates show a clear correlation with the calculated network connectivity values (see Table 4-3). With decreased network connectivity, higher Si release rate from the amorphous network could be achieved. The decrease of network connectivity in silicon oxycarbide results from both the depolymerization of the network via Ca incorporation at non-bridging-oxygen sites and the removal of network carbon. Consequently, SiOC-Ca5/SiOC-Ca12 with depolymerized silicon oxycarbide network has higher Si release rate than SiOC; SiOC-B7 has less network carbon than SiOC, also resulting in higher Si release (see Table 4-6). However, it is interesting to observe, that although SiOC-B7Ca5 has higher network connectivity than that of SiOC-B7 (5.55 compared to 4.95), its Si release rate is two times higher than that of SiOC-B7. As shown in Table 4-4, SiOC-B7Ca5 has incorporated Ca in silicon oxycarbide network, forming non-bridging-oxygens, while SiOC-B7 has reduced network carbon compared to SiOC. From equation (4-1), it is to know, that the removal of network carbon has stronger effect on reducing network connectivity than network depolymerization via non-bridging-oxygens.

Nevertheless, the network Si release implies a stronger influence from the depolymerized network, namely the network depolymerization improves the Si release and thus the bioactivity significantly.

Therefore, in Si(B,Ca)OC silicon oxycarbide systems, both minor calcium silicate secondary phase (wollastonite / pseudowollastonite) and network connectivity decrease in silicon oxycarbide amorphous matrix have contributions to the improvement of apatite forming ability upon SBF exposure of Si(B,Ca)OC compared to SiOC. While crystalline phases determine the early soaking stages (up to 3 days) during SBF test, the decrease of network connectivity improves Si release and thus bioactivity continuously.

4.2. PMS derived Si(B,Ca,Sr)OC bioactive materials

The study on Si(B,Ca)OC materials indicates the influence of B on enhancing the incorporation of Ca into amorphous SiOC network and the formation of Q³ units, as shown by the high Si release of SiOC-B7Ca5 sample from amorphous network after 3 days soaking (see Figure 4-8). It is well known, that the release of Sr from bioactive materials may heal osteoporosis (as mentioned in section 2.2.2). Therefore, two Sr modified SiOC-B7Ca5 samples, *i.e.*, SiOC-B7Ca5Sr0.8 and SiOC-B7Ca5Sr4 with Sr/Si molar ratio of 0.008 and 0.04 respectively, were prepared in the same way from PMS based precursors according to Table 3-1. In the following sections, the influence of strontium modification on the ion release and apatite forming ability of Si(B,Ca,Sr)OC materials upon SBF immersion is discussed and compared with the behavior of SiOC-B7Ca5.

4.2.1. Structure characterization

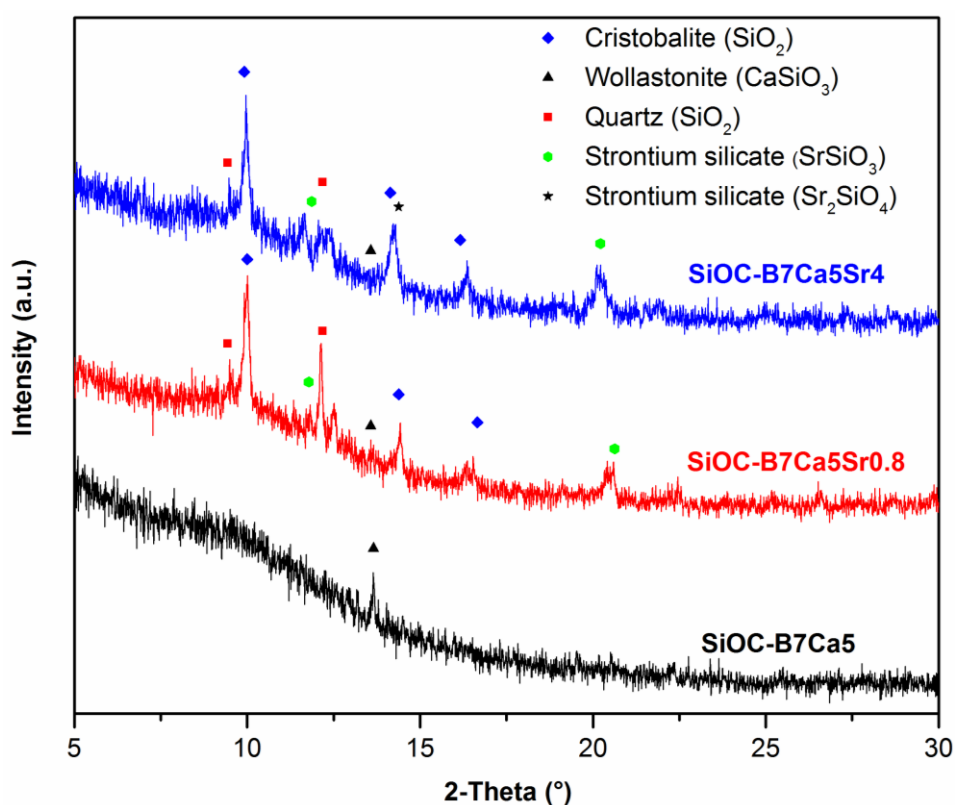


Figure 4-14. XRD patterns of Si(B,Ca,Sr)OC samples and SiOC-B7Ca5.

As shown in Figure 4-14, even at a very low Sr loading (Sr/Si = 0.008), SiOC-B7Ca5Sr0.8 has much stronger crystallization than SiOC-B7Ca5. As mentioned in section 2.1.2, the crystallization of SiO₂ in ternary silicon oxycarbide is suppressed by “free carbon” and nano-domain structure that prevent nuclei

growth. However, both SiOC-B7Ca5Sr0.8 and SiOC-B7Ca5Sr4 have high amounts of cristobalite and quartz. The incorporation of network modifiers into silicate glasses has been reported to increase the SiO₄ tetrahedron mobility and thus its crystallization tendency [228]. SiOC-B7Ca5Sr0.8 and SiOC-B7Ca5Sr4 have high fractions of network modifiers (both Sr and Ca). Since Sr²⁺ is slightly larger than Ca²⁺, the network loosening and thus pro-crystallization effect of Sr is stronger than that of Ca; at a Ca/Sr molar ratio of 4/5 (close to 1) in the case of SiOC-B7Ca5Sr4, metasilicate eutectic systems can form, which favors the crystallization [229]. Both factors may have promoted the crystallization of SiO₂ in SiOC-B7Ca5Sr0.8 and SiOC-B7Ca5Sr4. Furthermore, Sr has a strong tendency to form strontium silicate phases in silicon oxycarbide systems, *i.e.*, SrSiO₃ at Sr/Si = 0.008 and additionally Sr₂SiO₃ at Sr/Si = 0.04. Thus, Si(B,Ca,Sr)OC samples show complex crystalline structure (*i.e.*, cristobalite, quartz, strontium silicates, calcium silicate).

4.2.2. Ion release kinetics upon SBF exposure

The BET specific surface area values, calculated for SiOC-B7Ca5Sr0.8 and SiOC-B7Ca5Sr4, are comparable to that of SiOC-B7Ca5 (see Table 4-7). Therefore, in the following comparison of their ion release kinetics and biomineralization upon SBF immersion, the influence of specific surface area will be considered as negligible.

Table 4-7. BET specific surface area (SSA) analysis and total pore volume of Si(B,Ca,Sr)OC samples, with comparison to that of SiOC-B7Ca5.

Sample	SiOC-B7Ca5	SiOC-B7Ca5Sr0.8	SiOC-B7Ca5Sr4
BET SSA [m²g⁻¹]	15.6	23.5	20.2
Total pore volume [cc/g]	6.5x10 ⁻²	7.4x10 ⁻²	5.9x10 ⁻²

The pH evolutions with soaking time upon SBF immersion for SiOC-B7Ca5Sr0.8 and SiOC-B7Ca5Sr4 were compared with that of SiOC-B7Ca5 in Figure 4-15. Additional Sr incorporation has increased the pH value in test fluids slightly compared to SiOC-B7Ca5. The ion exchange of network modifier cations Ca and Sr with protons in SBF solution is responsible for such pH increase according to Hench [2]. Thus, SiOC-B7Ca5Sr4 with the highest content of network modifier has the highest pH increase among the investigated samples (see Figure 4-15). It is also worthy to mention, that even in the case of SiOC-B7Ca5Sr4, the highest pH value (*ca.* 7.6) is still significantly lower than that (*ca.* 8.2) induced by the

bioactive glass with 45S5 composition (see Figure 4-8). Thus, pH increase related cytotoxic effects are expected to be absent for the investigated materials. However, high pH value is beneficial for calcium phosphate precipitation [211]. SiOC-B7Ca5Sr0.8 and SiOC-B7Ca5Sr4 are thus expected to have higher apatite forming ability than SiOC-B7Ca5.

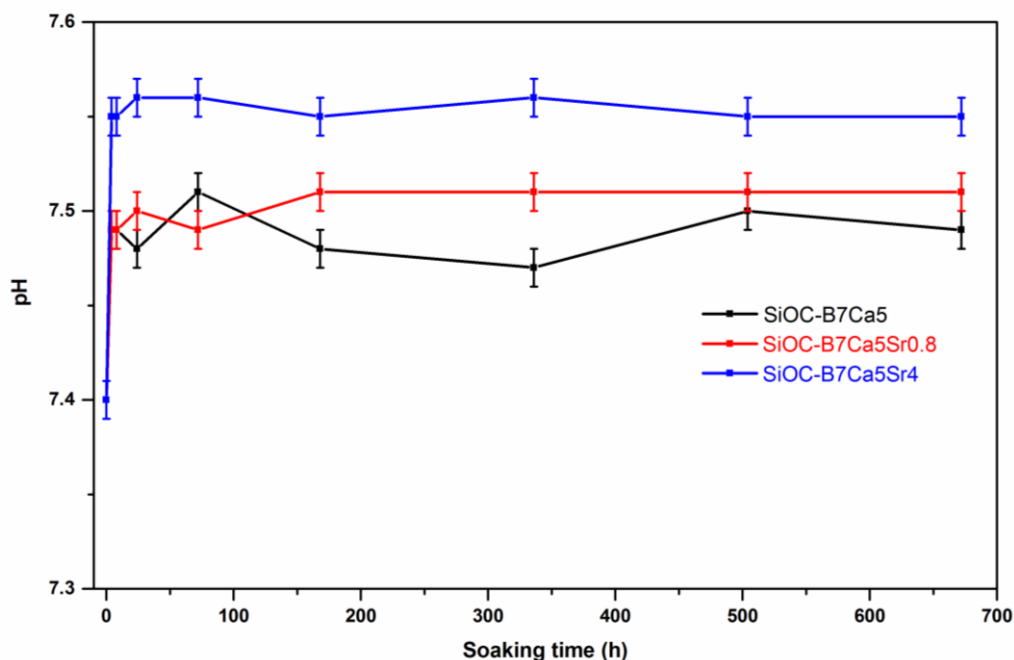
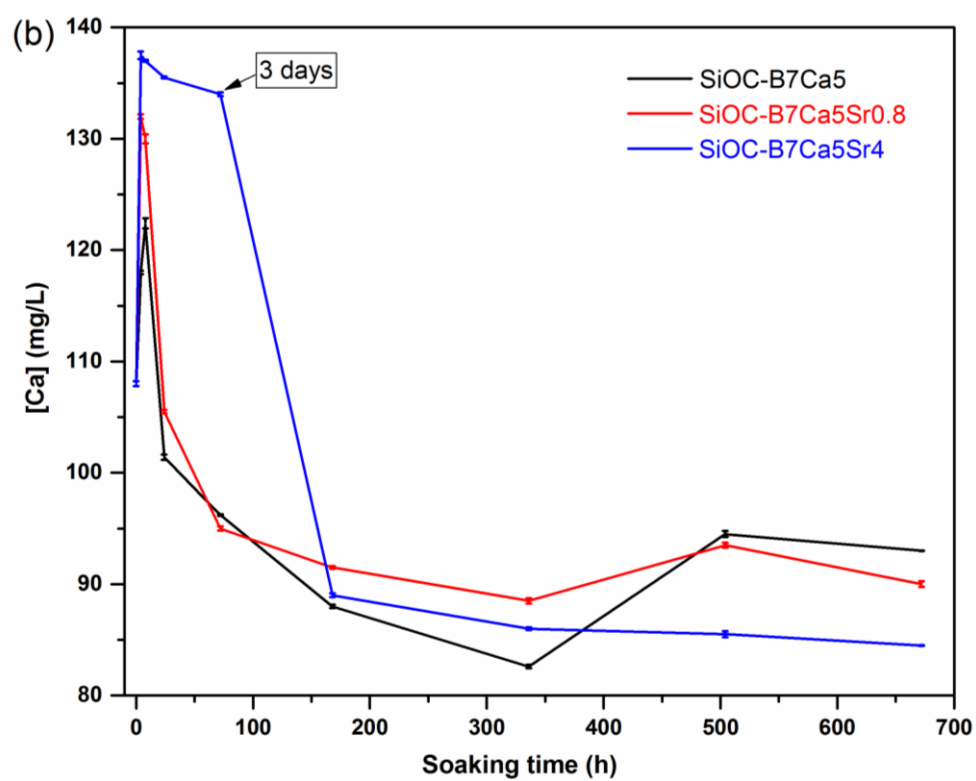
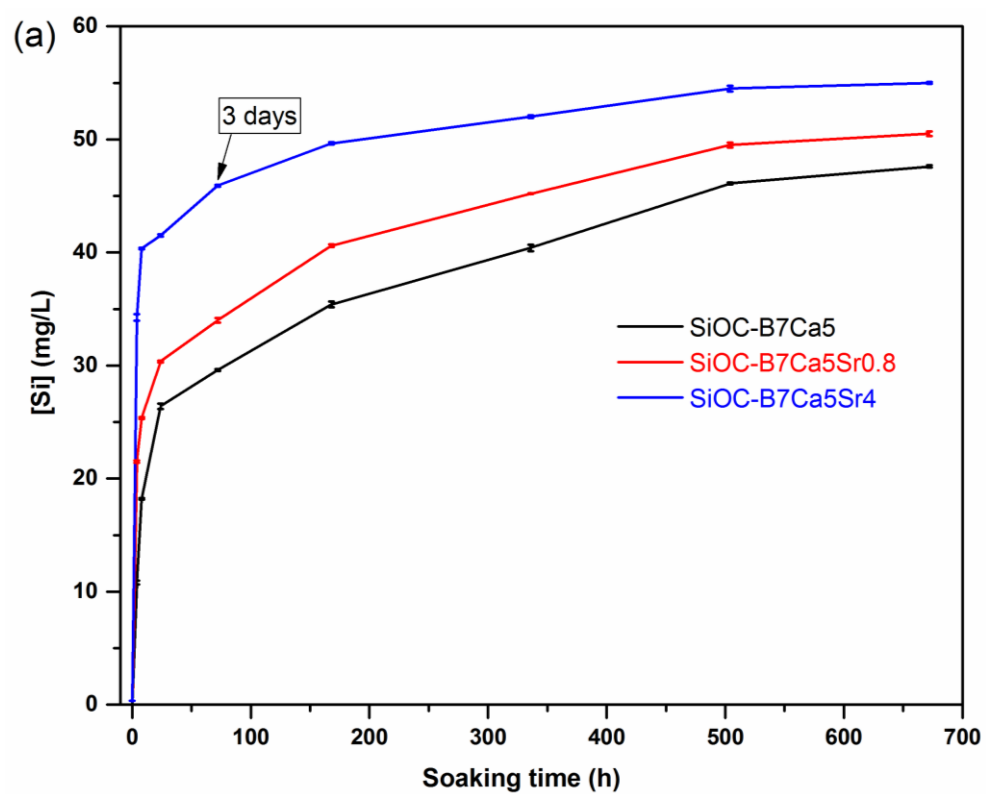


Figure 4-15. Evolution of pH value of the filtered SBF solutions as a function of the soaking time for Si(B,Ca,Sr)OC samples and SiOC-B7Ca5.

SiOC-B7Ca5Sr0.8 and SiOC-B7Ca5Sr4 show fast Si release within the first 3 days, similar to that of SiOC-B7Ca5 (see Figure 4-16 (a)). XRD investigation on Si(B,Ca,Sr)OC samples after 3 days SBF test confirms a complete dissolution of calcium silicate and strontium silicate phases (see Figure 4-17 (a)). Therefore, the fast initial Si release is rather related to the dissolution of silicate phases. A similar behavior was observed for Sr release. Interestingly, the ratio of Sr concentration in SBF solutions between SiOC-B7Ca5Sr0.8 and SiOC-B7Ca5Sr4 after 3 days is ca. 1:5, corresponding to the ratio of their Sr content (0.008:0.04). Thus, the released amount of Sr is proportional to the initial content of Sr in the material, implying a controllable Sr release by adjusting the material composition. However, Sr concentration is rather stable after the initial bursting. Thus, Sr in material was either depleted after 3 days or certain equilibrium between Sr release and consumption was reached.



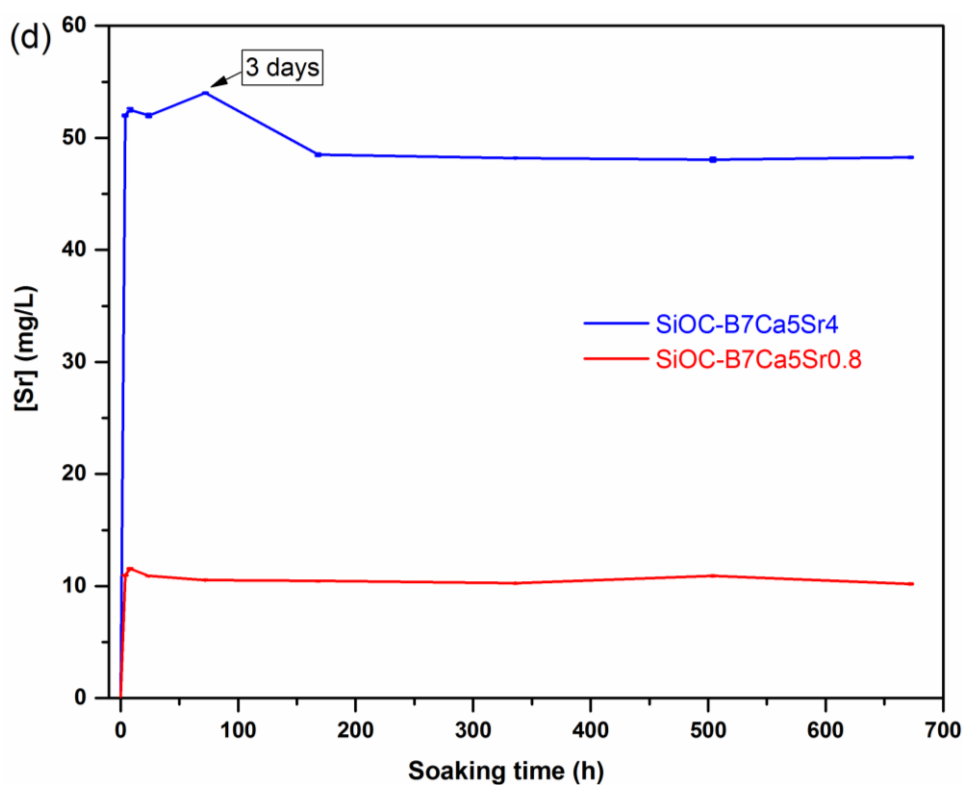
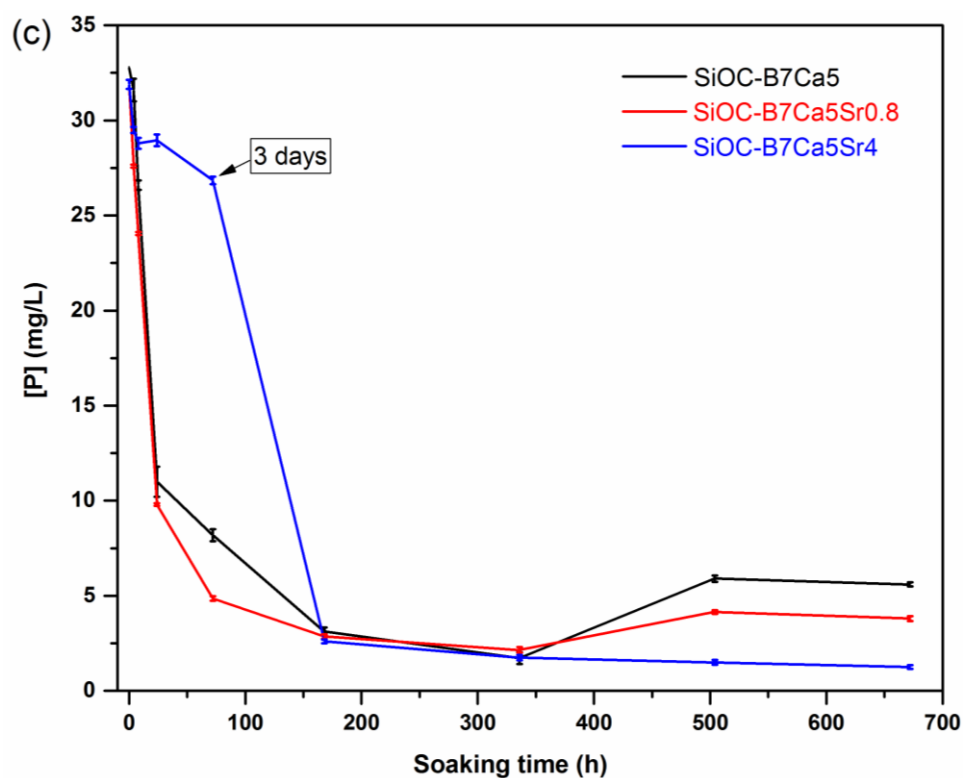


Figure 4-16. Evolution of (a) Si concentration, (b) Ca concentration, (c) P concentration and (d) Sr concentration of the filtered SBF solutions as a function of the soaking time for Si(B,Ca,Sr)OC samples and SiOC-B7Ca5. (The ion concentrations of Si, Ca, P and Sr were measured by Dipl.-Geol. Christian Scholz)

Higher pH increase in case of SiOC-B7Ca5Sr4 implies higher calcium phosphate precipitation. However, the evolutions of Ca and P concentration with soaking time (see Figure 4-16 (b) and (c)) show a slightly delayed consumption of Ca and P for SiOC-B7Ca5Sr4. The reason may lie in the reached high Sr concentration (ca. 50 mg/L) in SBF solution for SiOC-B7Ca5Sr4, which can inhibit calcium phosphate deposition, as reported by Koutsoukos *et al* [230]. Furthermore, a simultaneous decrease of Sr, Ca and P concentrations after 3 days was observed. The consumption of Sr is probably related to the formation of Sr substituted hydroxyapatite [231, 232]. Moreover, SiOC-B7Ca5 and SiOC-B7Ca5Sr0.8 show certain redissolution of precipitated calcium phosphate or hydroxyapatite, as being indicated by the slight increase of Ca and P concentrations after 2 weeks (see Figure 4-16 (b) and (c)). Such redissolution behavior is absent for SiOC-B7Ca5Sr4, implying that the Sr presence in solution suppresses hydroxyapatite redissolution, as also reported elsewhere [233].

4.2.3. Biomineralization upon SBF exposure

Although the formation of hydroxyapatite is not obvious in XRD analysis (see Figure 4-17 (a)), SEM surface analysis shows hydroxyapatite-like morphology on SiOC-B7Ca5Sr0.8 and SiOC-B7Ca5Sr4 already after 3 days SBF soaking (see Figure 4-18 (b) and (e)) [234, 235]. For SiOC-B7Ca5, the hydroxyapatite formation can be observed only after 7 days soaking (see Figure 4-13 (d)), although the faster decrease of Ca and P in SBF solution indicates faster calcium phosphate formation on SiOC-B7Ca5 than on SiOC-B7Ca5Sr4. This discrepancy can be explained by a retarded transformation of amorphous calcium phosphate into hydroxyapatite due to the lower pH increase upon SBF immersion of SiOC-B7Ca5 (see Figure 4-15 and Figure 4-16 (b)) [236]. Furthermore, the precipitation after 3 days on SiOC-B7Ca5Sr4 shows less defined hydroxyapatite-like shape than that on SiOC-B7Ca5Sr0.8 (see Figure 4-18). This is in good agreement with the observation of the faster Ca and P consumption for SiOC-B7Ca5Sr0.8. Moreover, a small diffraction peak, corresponding to hydroxyapatite, can be observed for Sr-containing samples after 7 days soaking, while this peak is almost negligible for SiOC-B7Ca5 (see Figure 4-17 (b)).

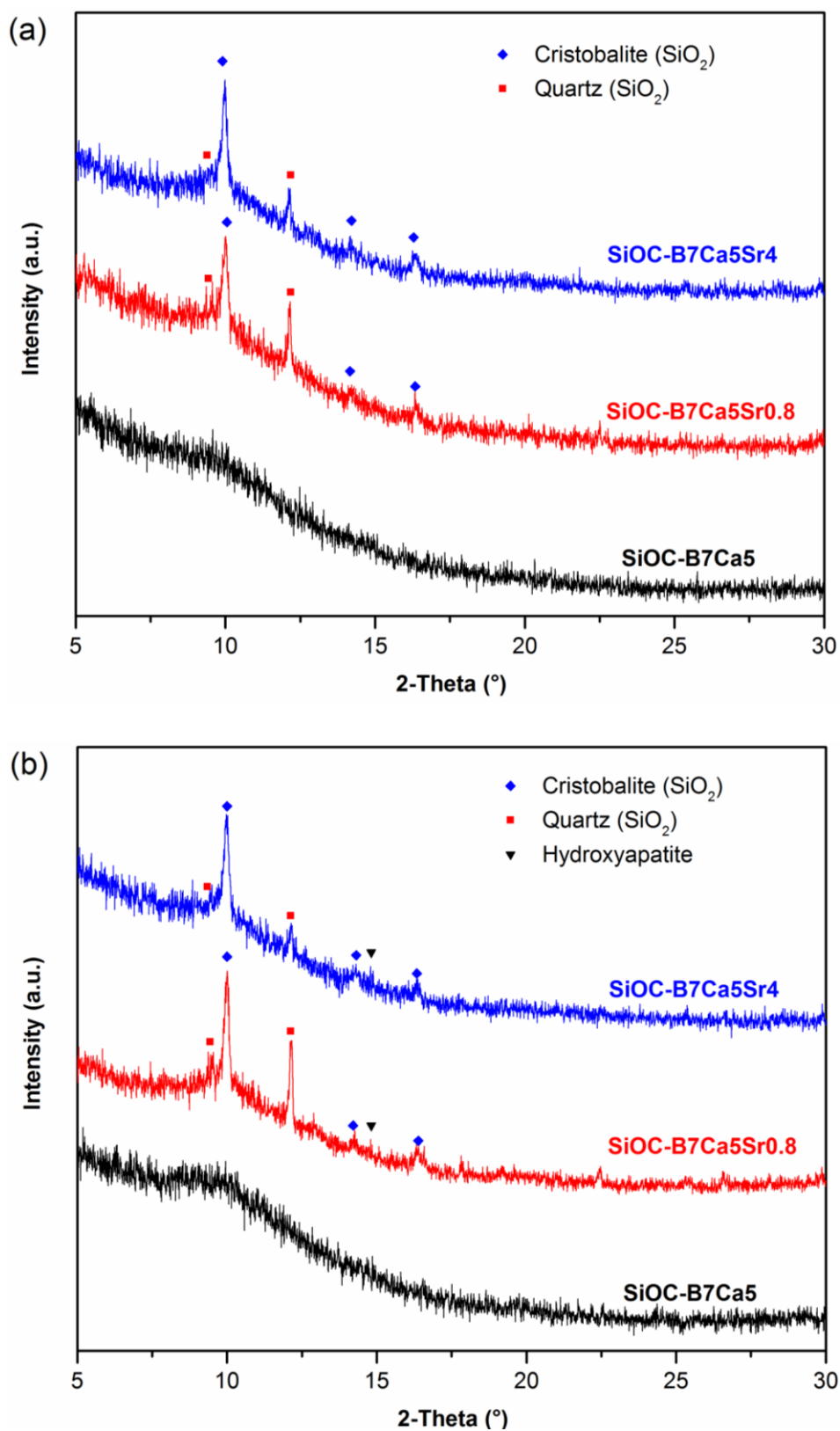


Figure 4-17. XRD patterns of $\text{Si}(\text{B,Ca,Sr})\text{OC}$ samples and SiOC-B7Ca5 (a) after 3 days SBF soaking and (b) after 7 days SBF soaking.

Therefore, Sr addition into Ca and B modified silicon oxycarbide has certain influences on their hydroxyapatite forming ability. However, this effect is more obvious for low Sr loading ($\text{Sr/Si} = 0.008$) than for high Sr loading ($\text{Sr/Si} = 0.04$). At the same time, Sr incorporation induces strong devitrification in silicon oxycarbide. Thus, the mechanism behind such bioactivity adjustment is complex. Both the formation of dissolvable strontium silicate phases and the formation of quartz and cristobalite phases may be responsible for the increased Si release, and thus improved bioactivity. Additionally, Sr presence in SBF solutions seems to result in the formation of Sr-substituted hydroxyapatite and suppress the hydroxyapatite redissolution. Thus, the influence of released Sr in SBF solutions on apatite formation should also be taken into consideration.

On the other hand, Sr release from Sr-containing samples is very fast and correlated directly to its initial content in test materials. In the present study, the Sr concentration in SBF solution reaches 10-50 mg/L after only 3 days, which may be beneficial for achieving osteoporosis-healing effects [120, 229]. However, a more controllable, *i.e.*, slower and continuous, Sr release was absent, which is probably related to the strong presence of Sr in crystalline strontium silicate and the suppressed incorporation of Sr into silicon oxycarbide amorphous matrix. Thus, silicon oxycarbide systems with a high capacity to incorporate Sr in amorphous matrix should be investigated in the future.

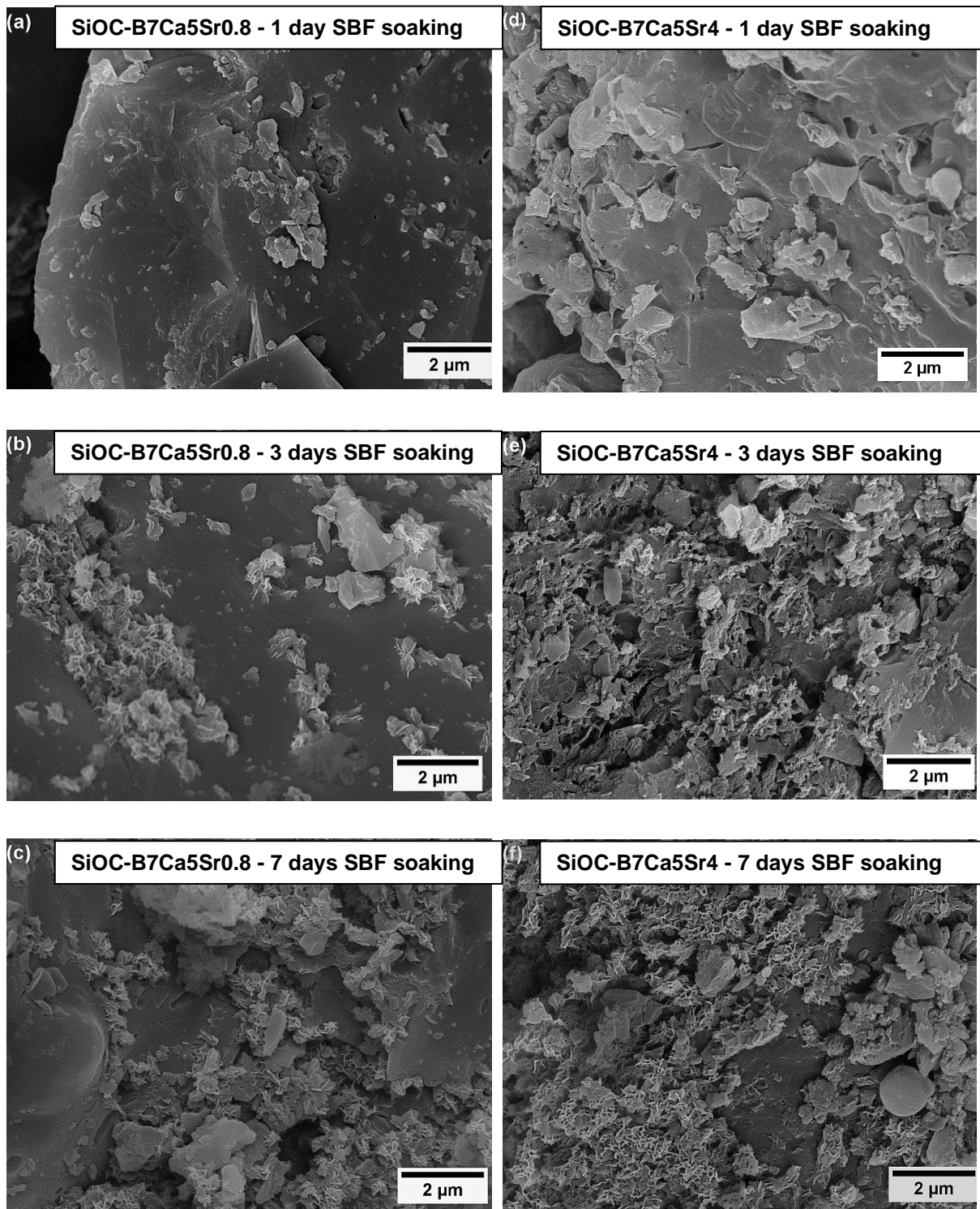


Figure 4-18. SEM surface morphology of SiOC-B7Ca5Sr0.8 and SiOC-B7Ca5Sr4 after 1 day, 3 days and 7 days SBF soaking.

4.3. Sol-gel derived Si(Ca)OC bioactive materials

High specific surface area is beneficial for achieving high bioactivity in the case of bioactive silicate glasses (see section 2.2.1) and is related to mesoporous structure of the materials. Moreover, mesoporosity can provide some added medical functions, such as the delivery of growth factors or antibiotics (see section 2.3.3). Mesoporous bioactive silicon oxycarbide materials can thus be promising candidates for potential bone tissue engineering applications.

Mesoporous silicon oxycarbide have been achieved by applying sol-gel synthesized precursors [176, 237], using mesoporous templates [238] or applying post-synthesis treatments of HF etching or air calcination [239]. Particularly, the versatility of the sol-gel approach is beneficial for preparing SiOC with tunable porosity, and the achieved porous SiOC materials have been reported to possess high specific surface areas (*i.e.*, > 500 m²/g) [237, 240, 241]. However, typical sol-gel process for metal modified silicon oxycarbides is realized via co-polymerization between alkoxysilanes and metal alkoxides [242, 243] and organic metal alkoxides are costly and also difficult to handle due to their high tendency to hydrolyze with moisture in air [104]. Furthermore, the use of metal alkoxides requires the usage of (possibly toxic) organic solvents, which is not recommendable from environmental aspects. A clean (water-based) process to prepare metal-containing silicon oxycarbide is necessary, as it has been used for the synthesis of silicate based bioactive glasses [204, 244]. In following sections, the feasibility of inorganic metal source (calcium nitrate) for modifying silicon oxycarbides and its influence on the material porosity will be investigated.

For this purpose, Ca-containing silicon oxycarbides (Si(Ca)OC) were thermally converted from xerogels derived from sol-gel synthesis of triethoxymethylsilane and calcium nitrate in inert gas atmosphere. The porous structure and specific surface area of prepared silicon oxycarbide samples were analyzed with N₂ sorption method, accompanied with SEM surface morphology analysis. A correlation between the final porosity of silicon oxycarbide samples and the influence of calcium nitrate loading will be discussed. Furthermore, *in vitro* SBF bioactivity assessment has been conducted, in order to investigate the effects of Ca loading and porosity on bioactive behavior.

4.3.1. Structure characterization

The xerogels prepared according to Figure 3-2 were investigated by means of FTIR spectroscopy. As evident from Figure 4-19 (a), the spectra of all prepared xerogels exhibit O-Si-O, Si-C, Si-O-Si, Si-CH₃ vibrations [17, 196, 245]. Moreover, the Ca-containing xerogels, SG-Ca5, SG-Ca12 and SG-Ca50, show the presence of NO₃⁻ vibration (ca. 1380 cm⁻¹) and OH/H₂O vibration (ca. 1630 cm⁻¹) indicating the presence of residual nitrate and hydroxy groups after drying [204, 244]. The peak intensity ratio of $\nu(\text{NO}_3^-)/\nu(\text{Si-O-Si})$ is shown to increase from SG-Ca5 to SG-Ca50, correlating to the increasing calcium nitrate loading from SG-Ca5 to SG-Ca50. The XRD patterns of the prepared xerogels (see Figure 4-19 (b)) indicate that SG-Ca0, SG-Ca5 and SG-Ca12 are X-ray amorphous; whereas, crystalline calcium nitrate (hydrate) phases were observed in SG-Ca50. As reported in various case studies (e.g., Lin *et al.* [246]), calcium nitrate is still dissolved in pore liquids after gelation occurs during the sol-gel processing; thus, at this stage calcium nitrate is not incorporated into the sol-gel silicon-oxygen network. Consequently, the thermal treatment used to dry the gels resulted in the case of SG-Ca50 in the precipitation of crystalline calcium nitrate within the pores. This has not been observed for SG-Ca5 and SG-Ca12, most probably due to the significantly lower loading of calcium nitrate (Ca/Si = 0.05 and 0.12).

The xerogels were converted thermally into silicon oxycarbide based materials via pyrolysis in inert gas atmosphere. In Figure 4-20 (a), the FTIR spectra indicate that the methyl groups were completely removed after pyrolysis. Typical O-Si-O, Si-C and Si-O-Si vibration bands were identified for SiCa0, SiCa5 and SiCa12; whereas in the case of SiCa50 the observed bands were mainly assigned to calcium silicate (pseudowollastonite) [199]. The crystallization of pseudowollastonite along with small amounts of wollastonite in SiCa50 was confirmed by XRD analysis (see Figure 4-20 (b)). The crystallization of calcium silicates in SiCa50 was probably induced by the high amount of segregated calcium nitrate in the xerogel, which reacted with the silicon-oxygen network to form crystalline calcium silicate during the pyrolysis.

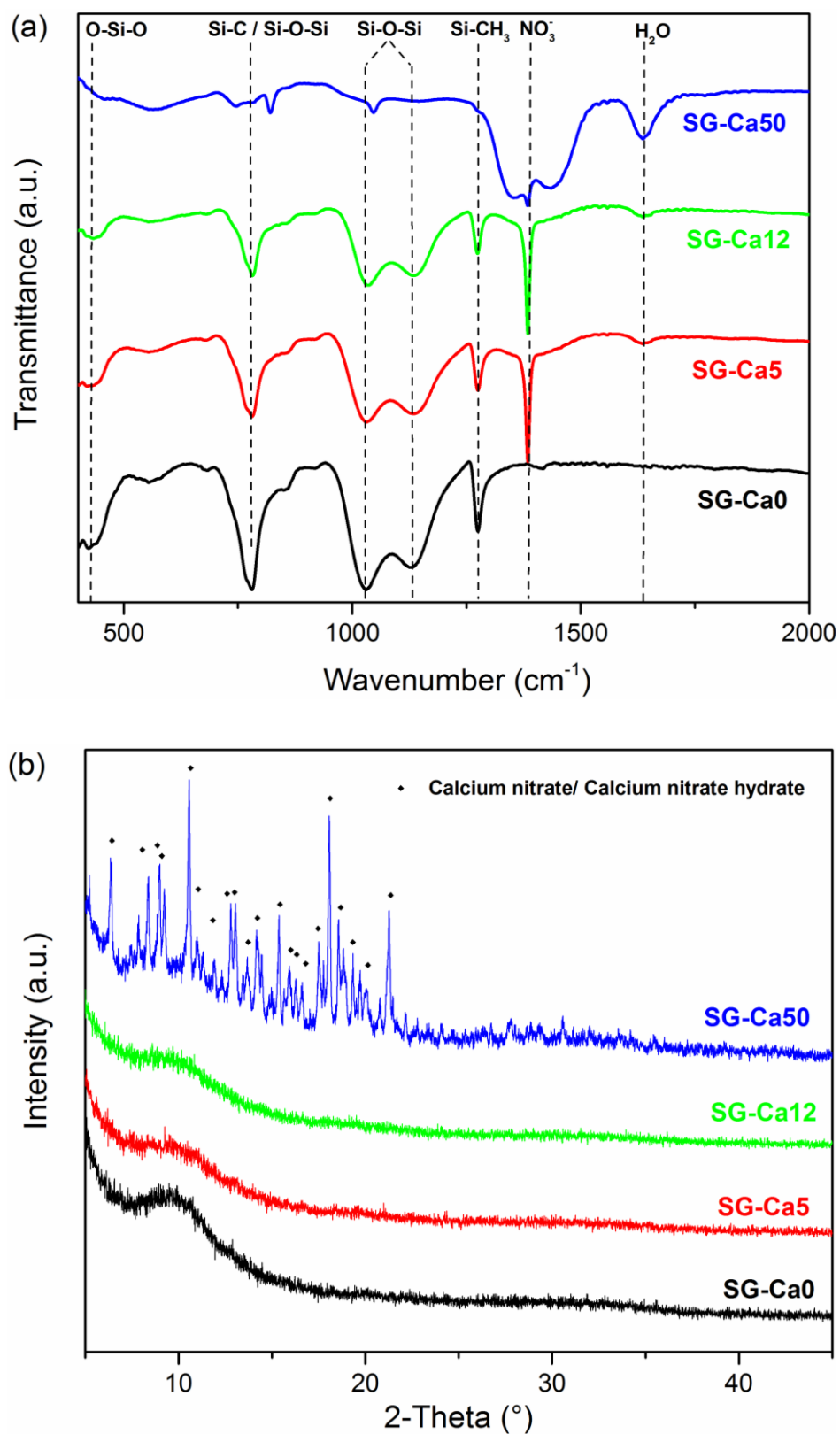


Figure 4-19. (a) FTIR spectra and (b) XRD diffractograms of xerogels SG-Ca0, SG-Ca5, SG-Ca12 and SG-Ca50.

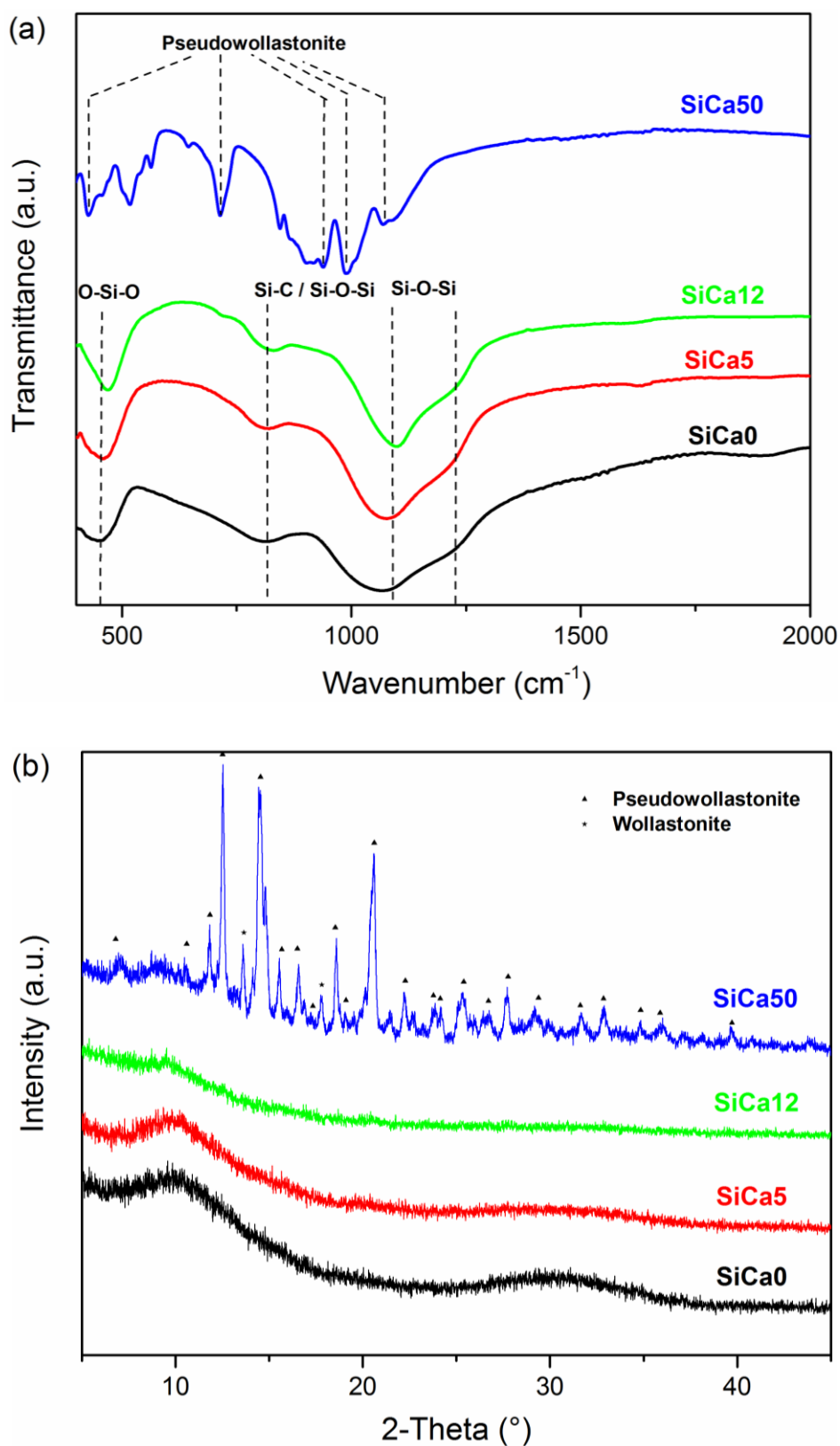


Figure 4-20. (a) FTIR spectra and (b) XRD diffractograms of silicon oxycarbide samples SiCa0, SiCa5, SiCa12, SiCa50 (samples obtained from corresponding xerogel precursors via pyrolysis at 1100 °C in Ar atmosphere).

For the amorphous oxycarbides SiCa0, SiCa5 and SiCa12, FTIR spectroscopic data were used in order to assess their network architecture. As shown in Figure 4-21, four vibration bands have been fitted by Voigt functions: (i) band centered at 1190-1220 cm^{-1} , corresponding to the longitudinal-optic (LO) Si-O-Si asymmetric stretching [173, 247]; (ii) band centered at 1040-1090 cm^{-1} , corresponding to the transverse-optic (TO) Si-O-Si asymmetric stretching [173, 247]; (iii) band centered at 800-815 cm^{-1} , corresponding to the overlapping (denoted as OV) of symmetric Si-O-Si stretching, bending Si-O-Si vibration and Si-C vibration [173, 196, 222, 247]; (iv) band centered at 900-970 cm^{-1} , corresponding to SiO_4 tetrahedral units containing one non-bridging-oxygen (Q^3) [198, 222]. As shown in Figure 4-21, the Q^3 component is found only in the fitted spectra of Ca-containing silicon oxycarbides, *i.e.*, SiCa5 and SiCa12, clearly demonstrating the effect of Ca as network modifier in the silicon oxycarbide network. This is in agreement with the results from ^{29}Si NMR analysis on Ca-containing silicon oxycarbides prepared from Ca-acetylacetonate-modified polysilsesquioxane (see section 4.1.2).

Since the band OV at $\sim 800 \text{ cm}^{-1}$ comprises both contributions from Si-O-Si and Si-C vibrations, the Q^3/OV area ratio can be used to estimate the fraction of Q^3 sites among the total Si species contained in the silicon oxycarbide network. As shown in Table 4-8, a significant increase of Q^3/OV ratio from SiCa5 to SiCa12 is observed, corresponding to the increased Ca amount incorporated in the network of SiCa12 (as compared to that of SiCa5). Additionally, since Si-C vibration only appears in the OV band, the $\text{OV}/(\text{LO}+\text{TO})$ area ratio may be used to assess the fraction of Si species with Si-C bond in the silicon oxycarbide network. Interestingly, the $\text{OV}/(\text{LO}+\text{TO})$ ratio shows a decreasing tendency from SiCa0 to SiCa12, implying the decrease of network carbon content with increasing Ca^{2+} incorporation in amorphous network. This was also reported in previous studies related to the modification of silicon oxycarbide networks with earth alkaline network modifiers [66].

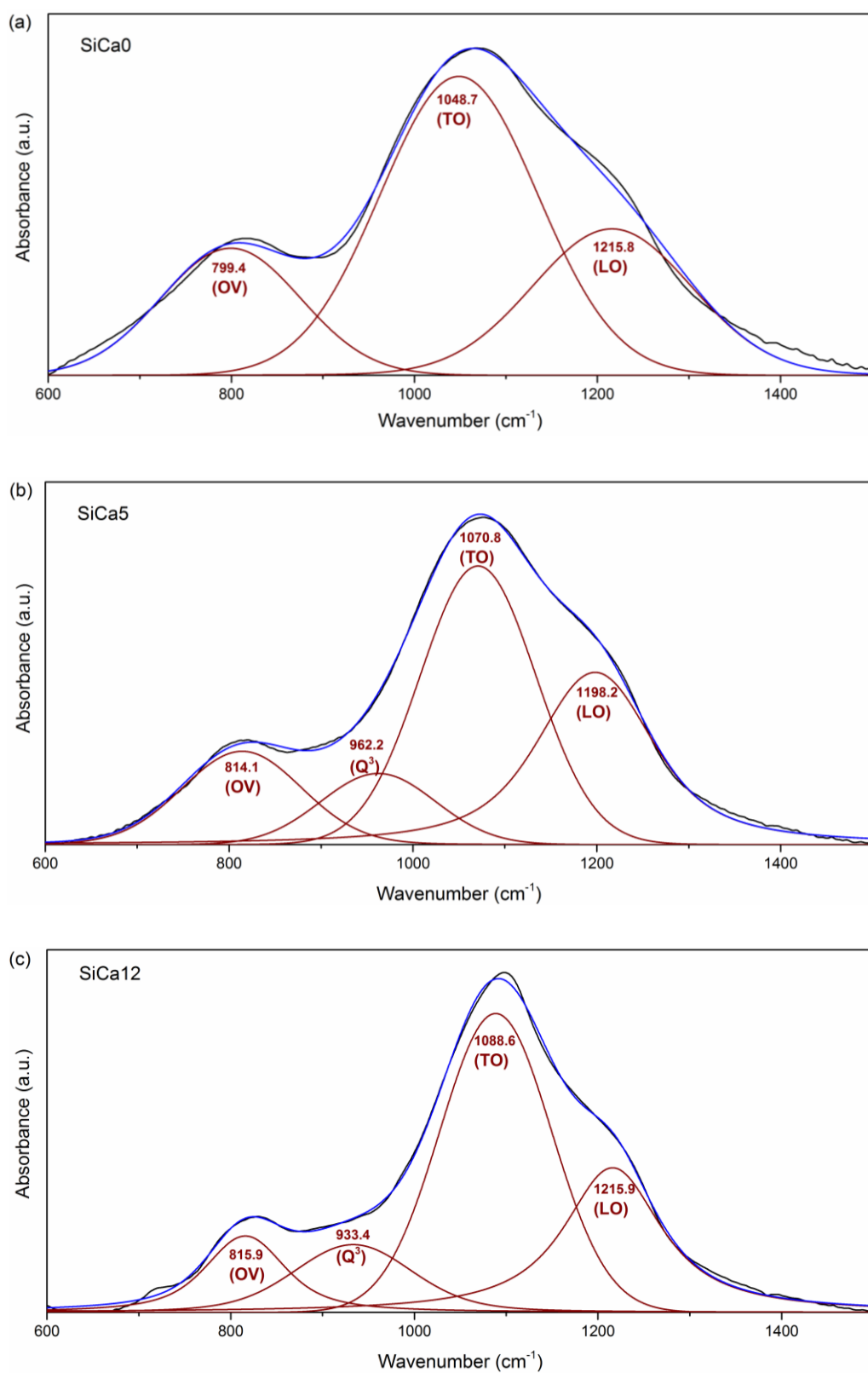


Figure 4-21. Deconvolution of FTIR spectra (black lines) between 600 cm^{-1} and 1500 cm^{-1} for (a) SiCa0, (b) SiCa5 and (c) SiCa12 into LO $\nu(\text{Si-O-Si})$, TO $\nu(\text{Si-O-Si})$, overlapping $\nu(\text{Si-O-Si})/\nu(\text{Si-C})$ (OV) and Q^3 components (red lines). The sum of all fitted peaks yields the blue lines in spectra.

Fidalgo *et al.* [247] ascribed the LO-TO splitting in silicate glass networks to long-range coulomb interactions and found out that a reduced LO-TO splitting may be related to the presence of high porosity, which disturbs the long-range coulomb interaction. As shown in Table 4-8, SiCa5 and SiCa12 show much lower LO-TO splitting than SiCa0, thus it is concluded that the prepared Ca-containing silicon oxycarbides possess significantly larger porosity than that of the ternary silicon oxycarbide SiCa0. The elemental compositions of the silicon oxycarbide samples prepared in this study can be estimated from their C and O contents and by assuming that Ca is present as calcium silicate in SiCa50 and as network modifier at the Q³ sites in SiCa5 and SiCa12 (see Table 4-9). All prepared silicon oxycarbide samples are shown to contain certain amount of segregated carbon, so-called “free carbon” [52]. Moreover, the decrease of the content of network carbon with increasing Ca²⁺ incorporation which was concluded based on the evaluation of the OV/(LO+TO) ratio in the FTIR spectra is clearly confirmed. The decrease of the carbon content in the oxycarbide network as well as its slight depolymerization due to the network modifier effect of Ca are considered to lead to decreased network connectivity in the series from SiCa0, to SiCa5 and to SiCa12.

Table 4-8. Percentual peak area to the total fitting area and area ratios of fitted components and the calculated LO-TO splitting from LO and TO peak centers for SiCa0, SiCa5 and SiCa12.

Sample	LO	TO	OV	Q ³ (%)	Q ³ /OV	OV/(LO+TO)	LO-TO splitting (cm ⁻¹)
	Si-O-Si (%)	Si-O-Si (%)	Si-O-Si and Si-C (%)				
SiCa0	26.8	53.1	20.1	-	-	0.25	167.1
SiCa5	33.3	41.6	14.6	10.5	0.7	0.20	127.4
SiCa12	28.8	47.3	11.1	12.8	1.1	0.15	127.3

Table 4-9. Elemental contents, empirical formulae and estimated phase compositions of prepared silicon oxycarbide samples.

Sample	Si (wt.%)	O (wt.%)	C (wt.%)	Ca (wt.%)	Empirical Formulae	Estimated phase compositions
SiCa0	47.92 ^a	40.18	11.90	-	Si ₁ O _{1.47} C _{0.58}	Si ₁ O _{1.47} C _{0.27} + 0.31 C
SiCa5	44.49 ^a	41.65	10.68	3.18 ^a	Si ₁ Ca _{0.05} O _{1.64} C _{0.56}	Si ₁ Ca _{0.05} O _{1.64} C _{0.21} + 0.35 C
SiCa12	40.93 ^a	42.64	9.41	7.02 ^a	Si ₁ Ca _{0.12} O _{1.82} C _{0.54}	Si ₁ Ca _{0.12} O _{1.82} C _{0.15} + 0.39 C
SiCa50	30.79 ^a	41.10	6.11	22.00 ^a	Si ₁ Ca _{0.50} O _{2.34} C _{0.46}	0.50 Si₁O_{1.68}C_{0.16} + 0.50 CaSiO₃ + 0.38 C

^a: Si and Ca contents are calculated from the difference to 100 wt.% and the Ca/Si molar ratios given in Table 3-2.

Porosity evaluation

The porosity of the xerogels as well as of the silicon oxycarbide samples was analyzed with N₂ sorption. As shown in Figure 4-22, SG-Ca0 has an isotherm with mixed features of type I and type IV, while SG-Ca5 has a type IV isotherm [207]. BJH pore size distribution of SG-Ca0 confirms the presence of high content of micropores (< 2 nm) and also a substantial amount of mesopores at 3.7 nm (see Figure 4-22 (c)); whereas, SG-Ca5 contains a dominating part of mesopores around 25 nm (see Figure 4-22 (d)). Thus, SG-Ca0 shows significantly smaller pore size as compared to SG-Ca5, which corresponds to the significant shrinkage observed during gel drying for SG-Ca0 compared to SG-Ca5 (see Figure 4-23). Since capillary pressure induces pore shrinkage during drying [248], calcium nitrate precipitation from pore liquid (as mentioned before) during drying in SG-Ca5 may have probably stabilized pore walls, preserving the mesoporous gel structure in SG-Ca5 xerogel. On the other hand, although SG-Ca12 and SG-Ca50 are almost shrinkage-free (see Figure 4-23), their isotherms are mainly microporous type I (see Figure 4-24), indicating a pore-filling effect of calcium nitrate. Thus, calcium nitrate loading shows two effects on the porosity of xerogels: (i) at a low amount (Ca/Si = 0.05) calcium nitrate precipitation during gel drying stabilizes mesopores; (ii) at high amounts (Ca/Si = 0.12 and 0.50) precipitated calcium nitrate fills up pores, reducing the pore size, as illustrated in Figure 4-25.

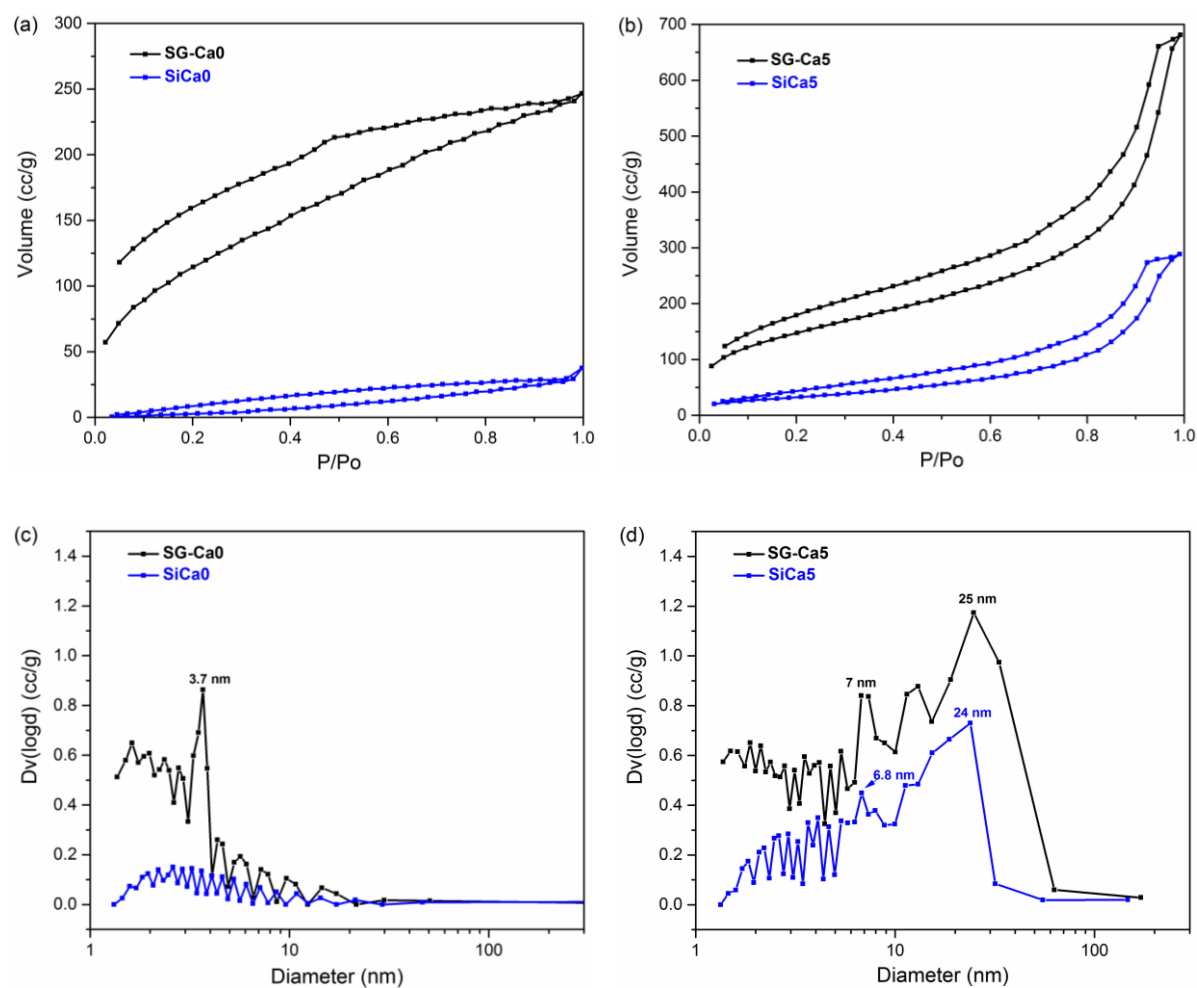


Figure 4-22. N_2 sorption isotherms of SG-Ca0 and SiCa0 in (a), SG-Ca5 and SiCa5 in (b) and the BJH desorption particle size distribution calculated for SG-Ca0 and SiCa0 in (c) and SG-Ca5 and SiCa5 in (d).

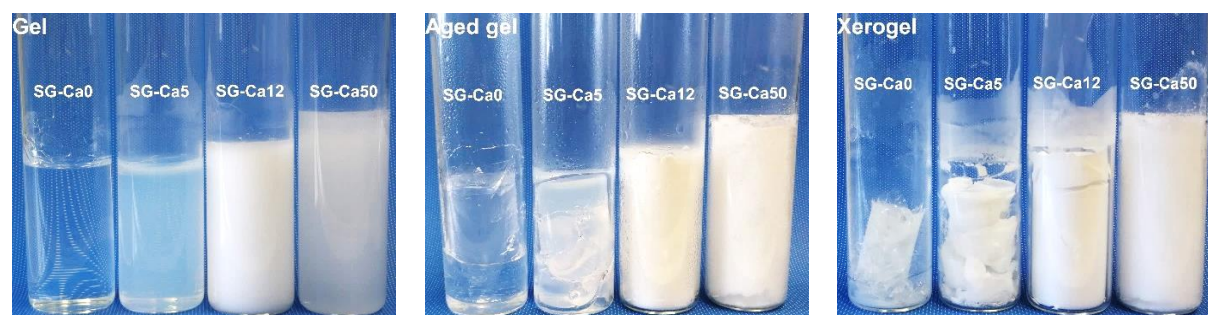


Figure 4-23. Optical pictures of gels, aged gels and xerogels prepared in sol-gel process (see Figure 3-2).

Interestingly, after pyrolysis at 1100 °C, the achieved SiCa5 has preserved its mesoporous structure (see Figure 4-22 (d)), while SiCa0 lost almost all of the micropores and mesopores observed in SG-Ca0 (see Figure 4-22 (c)). The collapse of micropores was also observed on SiCa12 and SiCa50 (see Figure 4-24). Since small pores contribute at the most to specific surface area [240], a significant decrease of BET specific surface area was observed for all samples after pyrolysis (see Table 4-10). The collapse and closure of micropores during the polymer-to-ceramic transformation of PDC ceramics have been investigated in various studies and were found to occur mainly at relatively high temperatures (> 600 °C), where the gas evolution from thermal decomposition of residual organic groups ceased [240, 249, 250]. In contrary, mesopores have been found to be more resistant against temperature [237] and show only a slight decrease of pore size after pyrolysis in the present study (see Figure 4-22 (d)).

Furthermore, SEM surface morphology confirms the mesoporous structure of SiCa5 (see Figure 4-26 (b)), while SiCa12 shows macroporosity (see Figure 4-26 (c)). The observed high porosity of SiCa5 and SiCa12 shows a good agreement with their low LO-TO splitting (see Table 4-8). Since SG-Ca12 is microporous, the macropores in SiCa12 must have been formed during the pyrolysis, namely via gas evolution during the removal of either residual organic groups or calcium nitrate, which decomposes at 500-700 °C by outgassing NO₂, O₂, and N₂ [251]. At a relatively high amount (Ca/Si = 0.12), precipitated calcium nitrate could have reached certain crystal/cluster size in SG-Ca12. Compared to nonporous SiCa0 (see Figure 4-26 (a)), the decomposition of such crystals/clusters would leave voids, which are able to grow to macropores with ongoing gas evolution. On the other hand, SiCa50 is mainly nonporous with surface morphology similarly to that of pseudowollastonite (see Figure 4-26 (d)) [252, 253]. Pseudowollastonite has good sinterability at 1100 °C [254, 255], and the sintering effect is considered to be responsible for the closure of pores left by calcium nitrate decomposition. Thus, calcium nitrate has different effects on the porosity of pyrolyzed silicon oxycarbide materials depending on its content: (i) at a low content (Ca/Si = 0.05), calcium nitrate decomposition does not influence the obtained mesoporosity noticeably; (ii) at a relatively high content (Ca/Si = 0.12), calcium nitrate decomposition induces the formation of macropores; (iii) at a significantly high content (Ca/Si = 0.50), calcium nitrate reacts with the Si-O gel network to form crystalline calcium silicate, which sinters at 1100 °C and thus induces the elimination of pores, as illustrated in Figure 4-25.

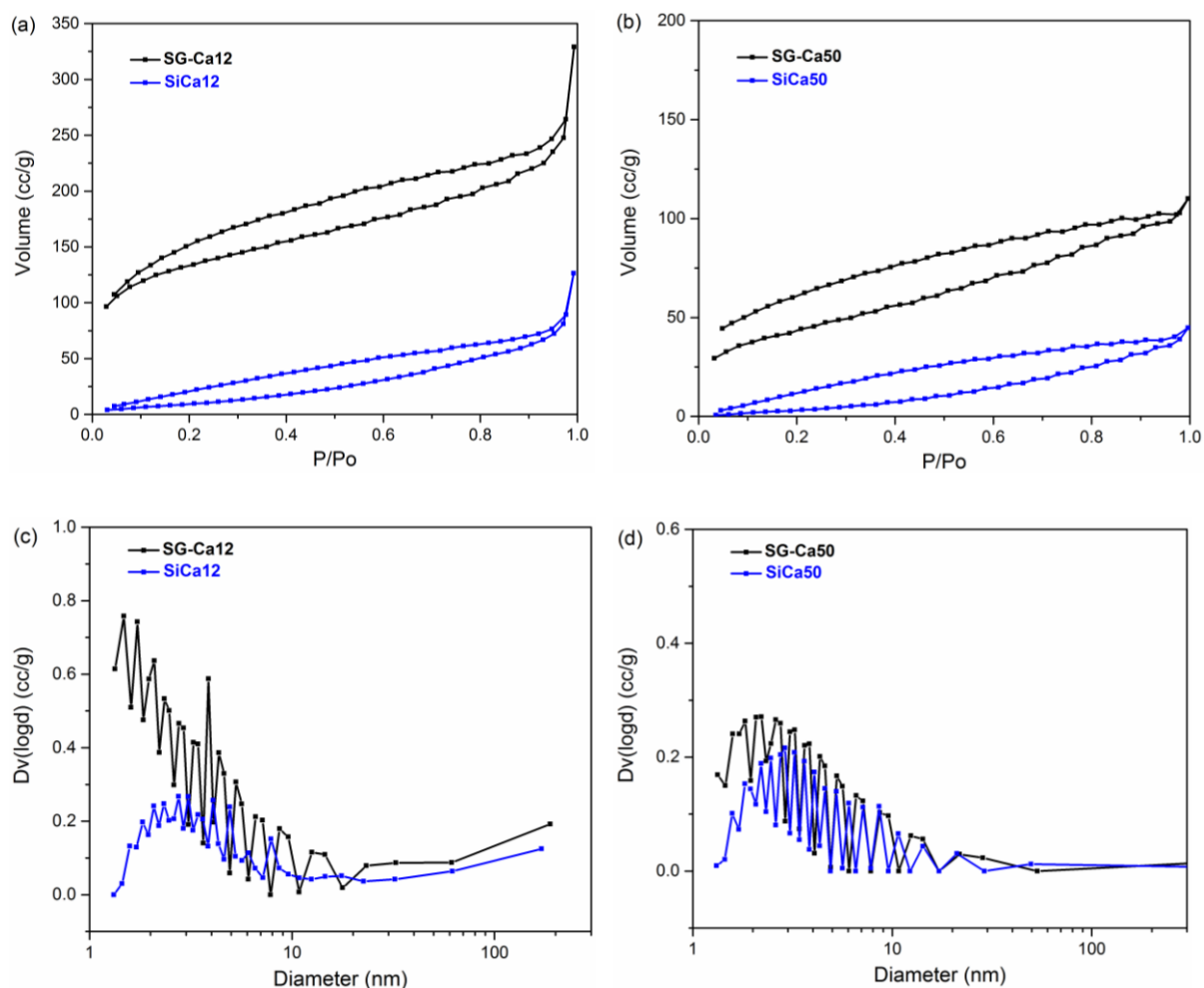


Figure 4-24. N₂ sorption isotherms of SG-Ca12 and SiCa12 in (a), SG-Ca50 and SiCa50 in (b) and the BJH desorption particle size distribution calculated for SG-Ca12 and SiCa12 in (c) and SG-Ca50 and SiCa50 in (d).

Table 4-10. BET specific surface area (SSA) values calculated for xerogel samples and silicon oxycarbide samples from N₂ sorption isotherms.

BET Specific surface area	Ca/Si molar ratio	Ca/Si molar ratio	Ca/Si molar ratio	Ca/Si molar ratio
SSA (m ² /g)	= 0.00	= 0.05	= 0.12	= 0.50
Xerogel	435.4	534.6	493.0	157.8
Silicon oxycarbide	22.5	123.4	39.5	23.9

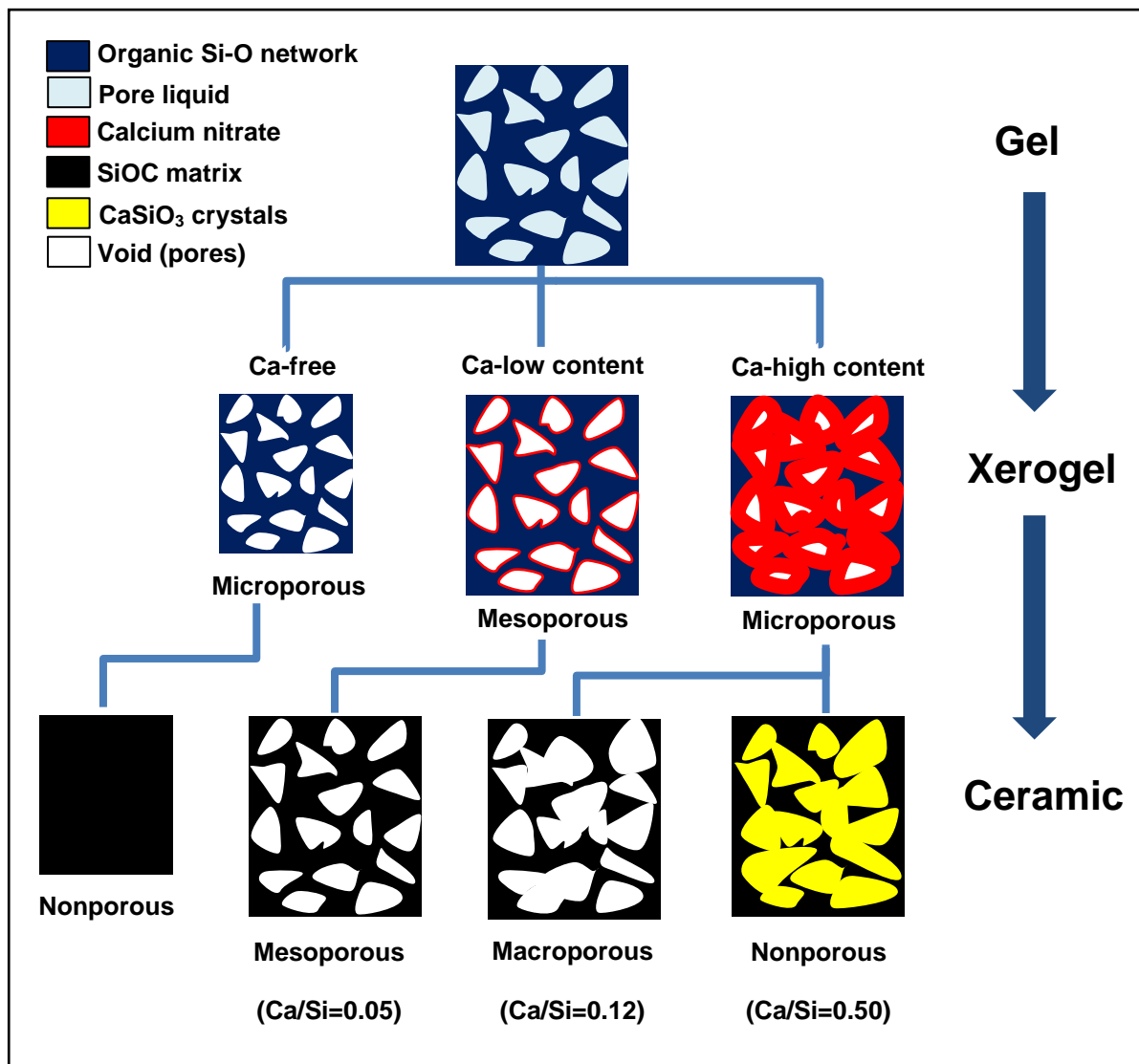


Figure 4-25. Schematic illustration of the porosity evolution from gels to xerogels and then to silicon oxycarbide materials and the porosity dependency on the designed Ca/Si molar ratio.

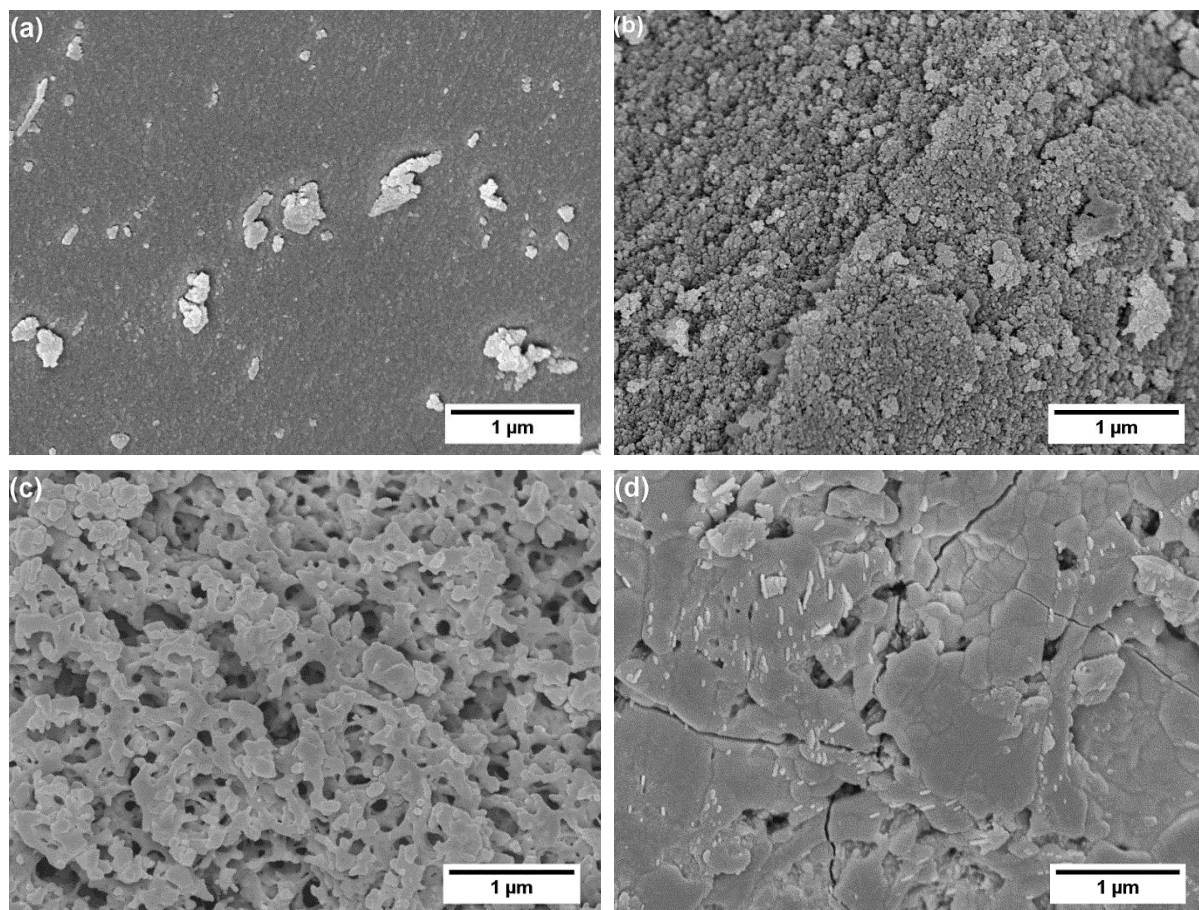


Figure 4-26. SEM surface morphology analysis of (a) SiCa0, (b) SiCa5, (c) SiCa12 and (d) SiCa50.

4.3.2. Biomineralization upon SBF exposure

In order to verify and compare the bioactivity of Ca-containing silicon oxycarbides, their apatite forming ability upon exposure to SBF solution was evaluated. FTIR spectra of SiCa5-T and SiCa50-T, *i.e.*, SiCa5 and SiCa50 after 7 days of SBF test, show typical PO_4^{3-} vibrations at 565 cm^{-1} , 605 cm^{-1} and 1047 cm^{-1} (see Figure 4-27 (a)), referring to the formation of hydroxyapatite-like calcium phosphate [147, 256, 257]. In the case of SiCa12-T, only two small absorption notches at 565 cm^{-1} , 605 cm^{-1} were observed, and the 1047 cm^{-1} vibration disappears under Si-O-Si vibration band. The precipitation of calcium phosphate on SiCa12-T is thus considered to be very limited. For SiCa0-T, no noticeable phosphate vibration is observable. XRD analysis (see Figure 4-27 (b)) confirms besides the formation of crystalline hydroxyapatite also the formation of calcite (CaCO_3) on SiCa50-T. It has been reported, that the formation of calcite is induced by a high concentration of Ca^{2+} in SBF solution [258]. By taking into consideration the high Ca/Si molar ratio (0.50) in SiCa50-T, which leads to the formation of soluble calcium silicate (pseudowollastonite) phase [259], a high Ca^{2+} release is expected to have induced the calcite formation. Additionally, SiCa5-T and SiCa12-T are shown to be X-ray amorphous. The FTIR detectable calcium phosphate on their surfaces is thus either not crystallized or the amount of crystallized hydroxyapatite is still not significant to be detected by XRD.

SEM analysis of SiCa5-T, SiCa12-T and SiCa50-T confirms the typical cauliflower-like morphology of hydroxyapatite on their surface (see Figure 4-28) [234, 235]. Interestingly, although no hydroxyapatite-like precipitation was observed on SiCa0-T (see Figure 4-28 (a)), as also suggested by FTIR and XRD results, its surface shows a sort of coarsening compared to the surface before SBF soaking (see Figure 4-26 (a)), indicating the occurrence of certain surface dissolution or leaching processes during SBF exposure. Indeed, Si release from ternary silicon oxycarbide takes place even though at a slow rate, according to our study of PMS derived ternary silicon oxycarbide (see section 4.1.3). The different shape and surface coverage of hydroxyapatite (HA) in Figure 4-28 shows clearly that SiCa50-T, with an almost complete HA surface covering, has the highest apatite forming ability among the investigated silicon oxycarbide samples.

A comparison between SiCa5-T and SiCa12-T shows more active apatite formation on SiCa5-T than on SiCa12-T: hydroxyapatite grows on SiCa5-T to a size of several micrometers; whereas, hydroxyapatite clusters on SiCa12-T are much smaller ($\sim 0.5\text{ }\mu\text{m}$). Furthermore, the higher HA formation on SiCa5-T is also confirmed by FTIR results (see Figure 4-27 (a)).

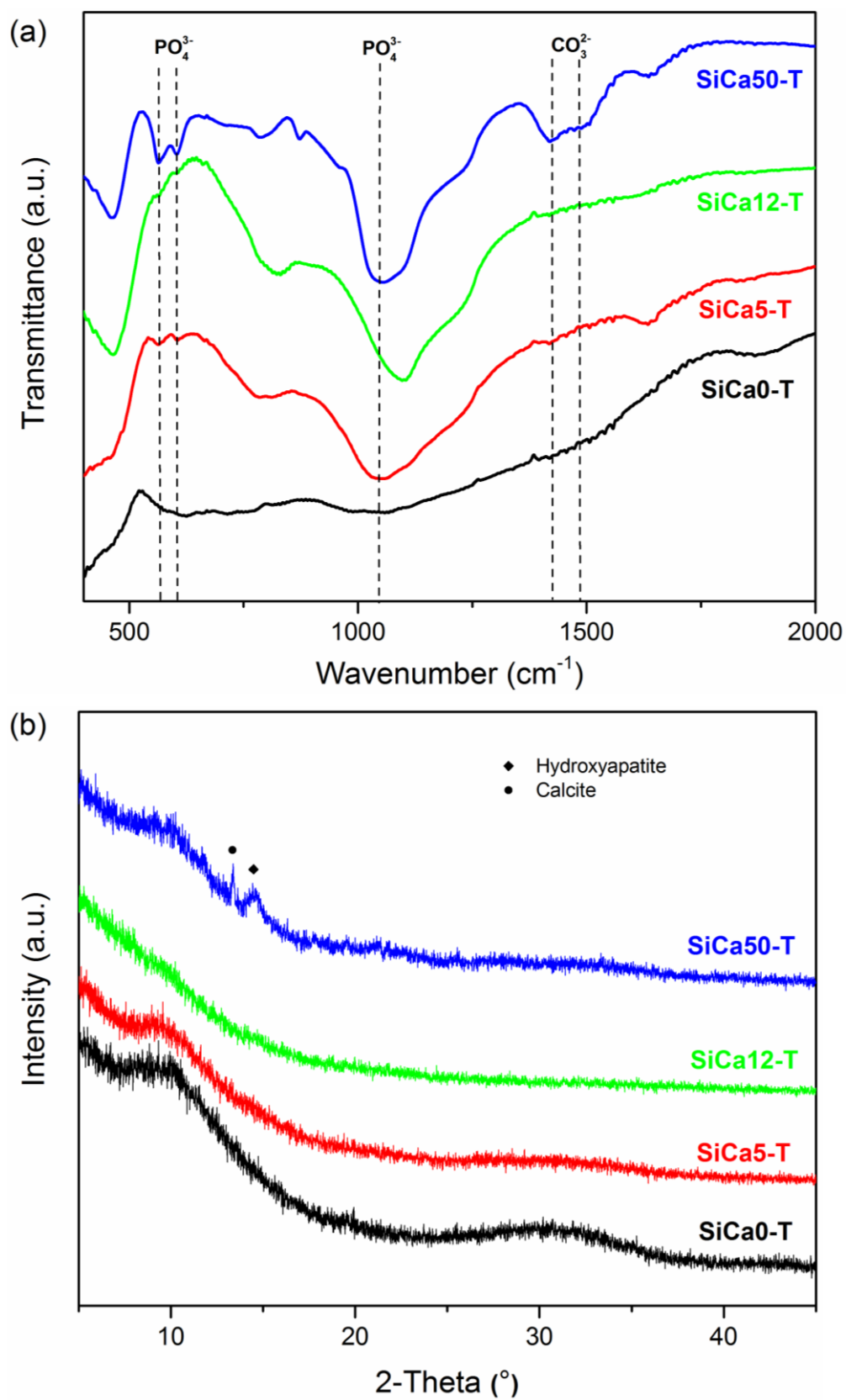


Figure 4-27. (a) FTIR spectra and (b) XRD diffractograms of silicon oxycarbide samples after 7 days SBF test.

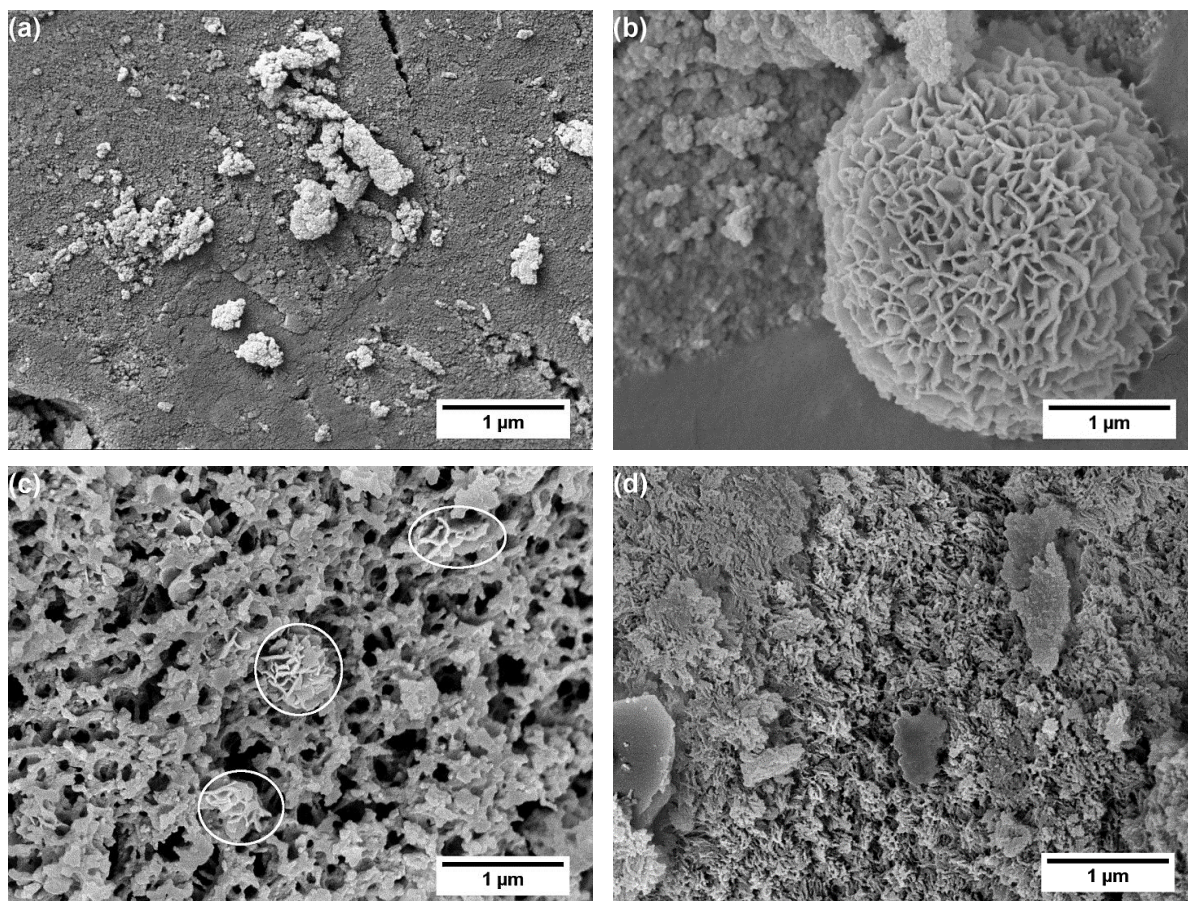


Figure 4-28. SEM surface morphology analysis of silicon oxycarbide samples after 7 days SBF test: (a) SiCa0-T, (b) SiCa5-T, (c) SiCa12-T and (d) SiCa50-T. The hydroxyapatite precipitation is marked in white circles for SiCa12-T.

4.3.3. Structure-property correlation

Therefore, although SiCa12 with higher Ca content (Q^3 fraction) and lower network carbon (see Table 4-9) is expected to have lower network connectivity than SiCa5, the apatite forming ability, *i.e.*, bioactivity, is higher in SiCa5. It is well known, that low network connectivity leads to high dissolution of bioactive glasses and thus high bioactivity [3]. However, the process to show bioactivity is also influenced by surface kinetics, as sol-gel derived bioactive glasses with high specific surface area could extend the range of SiO_2 content for showing bioactivity [2, 212]. Thus, the observed discrepancy between network connectivity and apatite forming ability in the present study is probably influenced by the specific surface area or porosity in the same way. Mesoporosity in SiCa5 provides nearly three times higher specific surface area than that of macroporous SiCa12 (see Table 4-10). Correspondingly, SiCa5 shows higher apatite forming ability. Therefore, the introduction of mesoporosity to silicon oxycarbide proves to be an effective method to improve the apatite forming ability, *i.e.*, bioactivity. Furthermore, mesoporosity is beneficial for obtaining additional functionalities, such as drug delivery ability or angiogenic effects. With limited Ca loading ($Ca/Si = 0.05$), SiCa5 is amorphous after 1100 °C pyrolysis. This high crystallization resistance is desirable if thermal processing of the material is anticipated [12, 150].

5. Conclusion and Outlook

The present work has investigated the structure-bioactivity correlation in SiOC based materials. On one hand, the SiOC network architecture and phase composition have been modulated upon incorporation of additional elements. On the other hand, sol-gel method has been applied to synthesize SiOC materials with tunable specific surface area / porosity. The bioactivity of SiOC, assessed upon immersion in SBF solution, has been correlated to these structural features, *i.e.*, network architecture, phase composition and porosity.

The network architecture of SiOC can be modified in two ways: (i) network depolymerization by forming non-bridging-oxygens; (ii) tuning of the network carbon to network oxygen ratio. SiOC network can be depolymerized by incorporating alkaline earth metals (*e.g.*, Ca), which act as network modifier. A slight depolymerization of SiOC network has a significant effect on improving the SiOC bioactivity upon SBF immersion. Furthermore, the network carbon to network oxygen ratio can be effectively decreased via incorporation of a small amount of boron, which acts as network former. Since the network carbon is tetravalent and the network oxygen is bivalent, a slight decrease of the network carbon to network oxygen ratio leads to a significant reduction of SiOC network connectivity. However, a decrease of network connectivity related to the change of the network carbon to network oxygen ratio only has a slight effect on tuning SiOC bioactivity.

Secondary crystalline silicate phases can be introduced to SiOC upon its modification with alkaline earth metals (*e.g.*, Ca, Sr). Thus, a partition of alkaline earth metals into amorphous SiOC network and crystalline silicate phases has taken place, which is similar to the phase separation of silica/alkaline-earth-metal-oxide melts at their immiscibility gap. Furthermore, the tendency to form crystalline silicate phases increases with increasing metal ion radius. Thus, while Ca modification induces negligible amount of wollastonite / pseudowollastonite (calcium silicate) phases, strontium silicate crystallization dominates upon Sr modification. The dissolution of secondary silicate phases in SBF solution modifies the local chemical environment to be beneficial for apatite formation. Thus, the bioactivity of SiOC materials is improved by the formation of secondary silicate phases. However, due to their rapid dissolution and consumption, the influence of secondary silicate phases on the bioactivity of prepared SiOC materials is considered to be a short-term effect.

The porosity of SiOC can be tuned by Ca modification via sol-gel process. The introduction of a Ca modifier (e.g., calcium nitrate) modifies the porosity of the xerogel precursors. Additionally, the decomposition of the Ca modifier and the formation of secondary calcium silicate phases influence the porosity of the resulting SiOC materials. Thus, at low content of Ca modifier, the xerogel porosity determines the porosity of the resulting SiOC. In this way, mesoporous SiOC possessing high specific surface area can be achieved. With increasing Ca content, gas evolution upon the decomposition of Ca modifier plays an important role on increasing the pore size in the resulting SiOC and macroporous SiOC can be obtained. At very high Ca content, calcium silicate crystallization dominates and its sintering at pyrolysis temperature closes pores and leads to nonporous SiOC based glass-ceramic. The porosity of SiOC materials is correlated to their varying specific surface area, which influences their bioactivity upon SBF immersion. Since the interaction between biomaterials and SBF solution occurs at the material surface, high specific surface area is beneficial for achieving high bioactivity. Correspondingly, the investigated mesoporous SiOC shows higher bioactivity than macroporous SiOC.

In conclusion, tailor-made network architecture, phase composition and porosity in SiOC glasses and glass-ceramics have been shown to provide improved bioactivity. However, the present work has only assessed apatite forming ability of SiOC materials. Besides the influence on apatite forming ability, the depolymerization of SiOC network can tune Si release kinetics; a phase composition design with therapeutic ions will induce therapeutic ion release; the porosity of SiOC can be utilized for drug delivery or transport of growth factors. All these aspects should be assessed in a cellular environment in the future, in order to achieve a more comprehensive understanding of the structure-bioactivity correlation for SiOC materials.

Thus, the future study should be focused on the investigation of cellular responses to released ions, particularly Si, Sr and B, from SiOC materials. A correlation of osteogenic and angiogenic effects to material structure would be crucial for designing clinically applicable bioactive SiOC materials. Furthermore, the high processability of SiOC precursors should be made use of to synthesize bioactive structures, such as 3D scaffolds or coatings. Particularly, wet-chemically based coating techniques, such as dip-coating or spin-coating, should be taken into consideration, since sol-gel method proves to be suitable for synthesizing Ca modified SiOC materials.

6. References

1. Damien, C.J.; Parsons, J.R. Bone graft and bone graft substitutes: A review of current technology and applications. *J. Appl. Biomater.* **1991**, *2*, 187–208.
2. Hench, L.L. The story of Bioglass®. *J. Mater. Sci. Mater. Med.* **2006**, *17*, 967–978.
3. Jones, J.R. Review of bioactive glass: From Hench to hybrids. *Acta Biomater.* **2013**, *9*, 4457–4486.
4. Hoppe, A.; Güldal, N.S.; Boccaccini, A.R. A review of the biological response to ionic dissolution products from bioactive glasses and glass-ceramics. *Biomaterials* **2011**, *32*, 2757–2774.
5. Fernandes, H.R.; Gaddam, A.; Rebelo, A.; Brazete, D.; Stan, G.E.; Ferreira, J.M.F. Bioactive Glasses and Glass-Ceramics for Healthcare Applications in Bone Regeneration and Tissue Engineering. *Mater. Basel Switz.* **2018**, *11*.
6. Gerhardt, L.-C.; Boccaccini, A.R. Bioactive Glass and Glass-Ceramic Scaffolds for Bone Tissue Engineering. *Materials* **2010**, *3*, 3867–3910.
7. Chen, Q.Z.; Efthymiou, A.; Salih, V.; Boccaccini, A.R. Bioglass®-derived glass–ceramic scaffolds: Study of cell proliferation and scaffold degradation in vitro. *J. Biomed. Mater. Res. A* **2008**, *84A*, 1049–1060.
8. Vogel, M.; Voigt, C.; Gross, U.M.; Müller-Mai, C.M. In vivo comparison of bioactive glass particles in rabbits. *Biomaterials* **2001**, *22*, 357–362.
9. Kapoor, S.; Goel, A.; Tilocca, A.; Dhuna, V.; Bhatia, G.; Dhuna, K.; Ferreira, J.M.F. Role of glass structure in defining the chemical dissolution behavior, bioactivity and antioxidant properties of zinc and strontium co-doped alkali-free phosphosilicate glasses. *Acta Biomater.* **2014**, *10*, 3264–3278.
10. Brito, A.F.; Antunes, B.; Santos, F. dos; Fernandes, H.R.; Ferreira, J.M.F. Osteogenic capacity of alkali-free bioactive glasses. In vitro studies. *J. Biomed. Mater. Res. B Appl. Biomater.* **2017**, *105*, 2360–2365.
11. Groh, D.; Döhler, F.; Brauer, D.S. Bioactive glasses with improved processing. Part 1. Thermal properties, ion release and apatite formation. *Acta Biomater.* **2014**, *10*, 4465–4473.
12. Fu, Q.; Saiz, E.; Rahaman, M.N.; Tomsia, A.P. Bioactive glass scaffolds for bone tissue engineering: state of the art and future perspectives. *Mater. Sci. Eng. C* **2011**, *31*, 1245–1256.
13. Hench, L.L. Bioceramics. *J. Am. Ceram. Soc.* **1998**, *81*, 1705–1728.
14. Ni, S.; Chang, J. In vitro Degradation, Bioactivity, and Cytocompatibility of Calcium Silicate, Dimagnesium Silicate, and Tricalcium Phosphate Bioceramics. *J. Biomater. Appl.* **2009**, *24*, 139–158.
15. Kokubo, T.; Ito, S.; Huang, Z.T.; Hayashi, T.; Sakka, S.; Kitsugi, T.; Yamamuro, T. Ca, P-rich layer formed on high-strength bioactive glass-ceramic A-W. *J. Biomed. Mater. Res.* **1990**, *24*, 331–343.
16. Bréquel, H.; Parmentier, J.; Walter, S.; Badheka, R.; Trimmel, G.; Masse, S.; Latournerie, J.; Dempsey, P.; Turquat, C.; Desmartin-Chomel, A.; et al. Systematic Structural Characterization of the High-Temperature Behavior of Nearly Stoichiometric Silicon Oxycarbide Glasses. *Chem. Mater.* **2004**, *16*, 2585–2598.
17. Ionescu, E.; Terzioglu, C.; Linck, C.; Kaspar, J.; Navrotsky, A.; Riedel, R. Thermodynamic Control of Phase Composition and Crystallization of Metal-Modified Silicon Oxycarbides. *J. Am. Ceram. Soc.* **2013**, *96*, 1899–1903.
18. Lagonegro, P.; Rossi, F.; Galli, C.; Smerieri, A.; Alinovi, R.; Pinelli, S.; Rimoldi, T.; Attolini, G.; Macaluso, G.; Macaluso, C.; et al. A cytotoxicity study of silicon oxycarbide nanowires as cell scaffold for biomedical applications. *Mater. Sci. Eng. C* **2017**, *73*, 465–471.
19. Perale, G.; Giordano, C.; Daniele, F.; Masi, M.; Colombo, P.; Gottardo, L.; Maccagnan, S. A Novel Process for the Manufacture of Ceramic Microelectrodes for Biomedical Applications. *Int. J. Appl. Ceram. Technol.* **2008**, *5*, 37–43.
20. Gawęda, M.; Jeleń, P.; Długoń, E.; Wajda, A.; Leśniak, M.; Simka, W.; Sowa, M.; Detsch, R.; Boccaccini, A.R.; Sitarz, M. Bioactive layers based on black glasses on titanium substrates. *J. Am. Ceram. Soc.* **2018**, *101*, 590–601.
21. Gonzalo-Juan, I.; Detsch, R.; Mathur, S.; Ionescu, E.; Boccaccini, A.R.; Riedel, R. Synthesis and In Vitro Activity Assessment of Novel Silicon Oxycarbide-Based Bioactive Glasses. *Materials* **2016**, *9*, 959.
22. Tucker, S.A.; Lowy, A. The Preparation, Properties and Composition of Silundum. *J. Ind. Eng. Chem.* **1915**, *7*, 565–571.

23. Pantano, C.G.; Singh, A.K.; Zhang, H. Silicon Oxycarbide Glasses. *J. Sol-Gel Sci. Technol.* **1999**, *14*, 7–25.
24. Parmentier, J.; Patarin, J.; Dentzer, J.; Vix-Guterl, C. Formation of SiC via carbothermal reduction of a carbon-containing mesoporous MCM-48 silica phase: a new route to produce high surface area SiC. *Ceram. Int.* **2002**, *28*, 1–7.
25. Vix-Guterl, C.; McEnaney, B.; Ehrburger, P. SiC material produced by carbothermal reduction of a freeze gel silica-carbon artefact. *J. Eur. Ceram. Soc.* **1999**, *19*, 427–432.
26. Pola, J.; Pokorná, D.; Bastl, Z.; Šubrt, J. IR laser-induced chemical vapour deposition of silicon oxycarbide phases from 1,1,3,3-tetramethyldisiloxane. *J. Anal. Appl. Pyrolysis* **1996**, *38*, 153–159.
27. Gallis, S.; Nikas, V.; Suhag, H.; Huang, M.; Kaloyeros, A.E. White light emission from amorphous silicon oxycarbide (a-SiC_xO_y) thin films: Role of composition and postdeposition annealing. *Appl. Phys. Lett.* **2010**, *97*, 081905.
28. Ryan, J.V.; Pantano, C.G. Synthesis and characterization of inorganic silicon oxycarbide glass thin films by reactive rf-magnetron sputtering. *J. Vac. Sci. Technol. A* **2007**, *25*, 153–159.
29. Miyazaki, H. Structure and Optical Properties of Silicon Oxycarbide Films Deposited by Reactive RF Magnetron Sputtering Using a SiC Target. *Jpn. J. Appl. Phys.* **2008**, *47*, 8287.
30. Renlund, G.M.; Prochazka, S.; Doremus, R.H. Silicon oxycarbide glasses: Part I. Preparation and chemistry. *J. Mater. Res.* **1991**, *6*, 2716–2722.
31. Riedel R.; Mera G.; Hauser R.; Klonczynski A. Silicon-Based Polymer-Derived Ceramics: Synthesis Properties and Applications-A Review. *J. Ceram. Soc. Jpn.* **2006**, *114*, 425–444.
32. Stabler, C.; Ionescu, E.; Graczyk-Zajac, M.; Gonzalo-Juan, I.; Riedel, R. Silicon oxycarbide glasses and glass-ceramics: “All-Rounder” materials for advanced structural and functional applications. *J. Am. Ceram. Soc.* **2018**, *101*, 4817–4856.
33. Renlund, G.M.; Prochazka, S.; Doremus, R.H. Silicon oxycarbide glasses: Part II. Structure and properties. *J. Mater. Res.* **1991**, *6*, 2723–2734.
34. Stabler, C.; Schliephake, D.; Heilmaier, M.; Rouxel, T.; Kleebe, H.-J.; Narisawa, M.; Riedel, R.; Ionescu, E. Influence of SiC/Silica and Carbon/Silica Interfaces on the High-Temperature Creep of Silicon Oxycarbide-Based Glass Ceramics: A Case Study. *Adv. Eng. Mater.* **2019**, *21*, 1800596.
35. Xu, T.; Ma, Q.; Chen, Z. High-temperature behavior of silicon oxycarbide glasses in air environment. *Ceram. Int.* **2011**, *37*, 2555–2559.
36. Saha, A.; Raj, R.; Williamson, D.L. A Model for the Nanodomains in Polymer-Derived SiCO. *J. Am. Ceram. Soc.* **2006**, *89*, 2188–2195.
37. Ionescu, E.; Kleebe, H.-J.; Riedel, R. Silicon-containing polymer-derived ceramic nanocomposites (PDC-NCs): preparative approaches and properties. *Chem. Soc. Rev.* **2012**, *41*, 5032–5052.
38. Colombo, P.; Mera, G.; Riedel, R.; Sorarù, G.D. Polymer-Derived Ceramics: 40 Years of Research and Innovation in Advanced Ceramics. *J. Am. Ceram. Soc.* **2010**, *93*, 1805–1837.
39. Eom, J.-H.; Kim, Y.-W.; Kim, K.J.; Seo, W.-S. Improved electrical and thermal conductivities of polysiloxane-derived silicon oxycarbide ceramics by barium addition. *J. Eur. Ceram. Soc.* **2018**, *38*, 487–493.
40. Krüner, B.; Odenwald, C.; Jäckel, N.; Tolosa, A.; Kickelbick, G.; Presser, V. Silicon Oxycarbide Beads from Continuously Produced Polysilsesquioxane as Stable Anode Material for Lithium-Ion Batteries. *ACS Appl. Energy Mater.* **2018**, *1*, 2961–2970.
41. Kaur, S.; Cherkashinin, G.; Fasel, C.; Kleebe, H.-J.; Ionescu, E.; Riedel, R. Single-source-precursor synthesis of novel V8C7/SiC(O)-based ceramic nanocomposites. *J. Eur. Ceram. Soc.* **2016**, *36*, 3553–3563.
42. Ionescu, E.; Papendorf, B.; Kleebe, H.-J.; Poli, F.; Müller, K.; Riedel, R. Polymer-Derived Silicon Oxycarbide/Hafnia Ceramic Nanocomposites. Part I: Phase and Microstructure Evolution During the Ceramization Process. *J. Am. Ceram. Soc.* **2010**, *93*, 1774–1782.
43. Narisawa, M.; Terauds, K.; Raj, R.; Kawamoto, Y.; Matsui, T.; Iwase, A. Oxidation process of white Si–O–C(–H) ceramics with various hydrogen contents. *Scr. Mater.* **2013**, *69*, 602–605.
44. Radovanovic, E.; Gozzi, M.F.; Gonçalves, M.C.; Yoshida, I.V.P. Silicon oxycarbide glasses from silicone networks. *J. Non-Cryst. Solids* **1999**, *248*, 37–48.
45. Blum, Y.D.; MacQueen, D.B.; Kleebe, H.-J. Synthesis and characterization of carbon-enriched silicon oxycarbides. *J. Eur. Ceram. Soc.* **2005**, *25*, 143–149.
46. Sorarù, G.D.; D’Andrea, G.; Campostrini, R.; Babonneau, F.; Mariotto, G. Structural Characterization and High-Temperature Behavior of Silicon Oxycarbide Glasses Prepared from Sol-Gel Precursors Containing Si-H Bonds. *J. Am. Ceram. Soc.* **1995**, *78*, 379–387.

47. Sorarù, G.D.; Kundanati, L.; Santhosh, B.; Pugno, N. Influence of free carbon on the Young's modulus and hardness of polymer-derived silicon oxycarbide glasses. *J. Am. Ceram. Soc.* **2019**, *102*, 907–913.
48. Latournerie, J.; Dempsey, P.; Hourlier-Bahloul, D.; Bonnet, J.-P. Silicon Oxycarbide Glasses: Part 1—Thermochemical Stability. *J. Am. Ceram. Soc.* **2006**, *89*, 1485–1491.
49. Kleebe, H.-J.; Turquat, C.; Sorarù, G.D. Phase Separation in an SiCO Glass Studied by Transmission Electron Microscopy and Electron Energy-Loss Spectroscopy. *J. Am. Ceram. Soc.* **2001**, *84*, 1073–1080.
50. Saha, A.; Raj, R. Crystallization Maps for SiCO Amorphous Ceramics. *J. Am. Ceram. Soc.* **2007**, *90*, 578–583.
51. Widgeon, S.J.; Sen, S.; Mera, G.; Ionescu, E.; Riedel, R.; Navrotsky, A. ²⁹Si and ¹³C Solid-State NMR Spectroscopic Study of Nanometer-Scale Structure and Mass Fractal Characteristics of Amorphous Polymer Derived Silicon Oxycarbide Ceramics. *Chem. Mater.* **2010**, *22*, 6221–6228.
52. Roth, F.; Waleska, P.; Hess, C.; Ionescu, E.; Nicoloso, N. UV Raman spectroscopy of segregated carbon in silicon oxycarbides. *J. Ceram. Soc. Jpn.* **2016**, *124*, 1042–1045.
53. Breval, E.; Hammond, M.; Pantano, C.G. Nanostructural Characterization of Silicon Oxycarbide Glasses and Glass-Ceramics. *J. Am. Ceram. Soc.* **1994**, *77*, 3012–3018.
54. Martínez-Crespiera, S.; Ionescu, E.; Kleebe, H.-J.; Riedel, R. Pressureless synthesis of fully dense and crack-free SiOC bulk ceramics via photo-crosslinking and pyrolysis of a polysiloxane. *J. Eur. Ceram. Soc.* **2011**, *31*, 913–919.
55. Rosenberg, F.; Ionescu, E.; Nicoloso, N.; Riedel, R. High-Temperature Raman Spectroscopy of Nano-Crystalline Carbon in Silicon Oxycarbide. *Materials* **2018**, *11*, 93.
56. Nguyen, V.L.; Laidani, N.B.; Sorarù, G.D. N-doped polymer-derived Si(N)OC: The role of the N-containing precursor. *J. Mater. Res.* **2015**, *30*, 770–781.
57. Nguyen, V.L.; Zanella, C.; Bettotti, P.; Sorarù, G.D. Electrical Conductivity of SiOCN Ceramics by the Powder-Solution-Composite Technique. *J. Am. Ceram. Soc.* **2014**, *97*, 2525–2530.
58. Chollon, G. Oxidation behaviour of ceramic fibres from the Si–C–N–O system and related sub-systems. *J. Eur. Ceram. Soc.* **2000**, *20*, 1959–1974.
59. Peña-Alonso, R.; Mariotto, G.; Gervais, C.; Babonneau, F.; Soraru, G.D. New Insights on the High-Temperature Nanostructure Evolution of SiOC and B-Doped SiBOC Polymer-Derived Glasses. *Chem. Mater.* **2007**, *19*, 5694–5702.
60. Schiavon, M.A.; Gervais, C.; Babonneau, F.; Soraru, G.D. Crystallization Behavior of Novel Silicon Boron Oxycarbide Glasses. *J. Am. Ceram. Soc.* **2008**, *87*, 203–208.
61. Ionescu, E.; Papendorf, B.; Kleebe, H.-J.; Riedel, R. Polymer-Derived Silicon Oxycarbide/Hafnia Ceramic Nanocomposites. Part II: Stability Toward Decomposition and Microstructure Evolution at T>>1000°C. *J. Am. Ceram. Soc.* **2010**, *93*, 1783–1789.
62. Ionescu, E.; Linck, C.; Fasel, C.; Müller, M.; Kleebe, H.-J.; Riedel, R. Polymer-Derived SiOC/ZrO₂ Ceramic Nanocomposites with Excellent High-Temperature Stability. *J. Am. Ceram. Soc.* **2010**, *93*, 241–250.
63. Kaspar, J.; Terzioglu, C.; Ionescu, E.; Graczyk-Zajac, M.; Hapis, S.; Kleebe, H.-J.; Riedel, R. Stable SiOC/Sn Nanocomposite Anodes for Lithium-Ion Batteries with Outstanding Cycling Stability. *Adv. Funct. Mater.* **2014**, *24*, 4097–4104.
64. Hojamberdiev, M.; Prasad, R.M.; Fasel, C.; Riedel, R.; Ionescu, E. Single-source-precursor synthesis of soft magnetic Fe₃Si- and Fe₅Si₃-containing SiOC ceramic nanocomposites. *J. Eur. Ceram. Soc.* **2013**, *33*, 2465–2472.
65. Sen, S.; Widgeon, S.J.; Navrotsky, A.; Mera, G.; Tavakoli, A.; Ionescu, E.; Riedel, R. Carbon substitution for oxygen in silicates in planetary interiors. *Proc. Natl. Acad. Sci.* **2013**, *110*, 15904–15907.
66. Ionescu, E.; Sen, S.; Mera, G.; Navrotsky, A. Structure, energetics and bioactivity of silicon oxycarbide-based amorphous ceramics with highly connected networks. *J. Eur. Ceram. Soc.* **2018**, *38*, 1311–1319.
67. Williams, D.F. *The Williams Dictionary of Biomaterials*; Liverpool University Press, 1999; ISBN 978-0-85323-734-1.
68. Binyamin, G.; Shafi, B.M.; Mery, C.M. Biomaterials: A primer for surgeons. *Semin. Pediatr. Surg.* **2006**, *15*, 276–283.
69. Williams, D.F. On the mechanisms of biocompatibility. *Biomaterials* **2008**, *29*, 2941–2953.
70. Yu, W.; Wang, X.; Zhao, C.; Yang, Z.; Dai, R.; Dong, F. Biocompatibility of subretinal parylene-based Ti/Pt microelectrode array in rabbit for further artificial vision studies. *J. Ocul. Biol. Dis. Infor.* **2009**, *2*, 33–36.

71. Takami, Y.; Nakazawa, T.; Makinouchi, K.; Glueck, J.; Nosé, Y. Biocompatibility of alumina ceramic and polyethylene as materials for pivot bearings of a centrifugal blood pump. *J. Biomed. Mater. Res.* **1997**, *36*, 381–386.
72. Nair, L.S.; Laurencin, C.T. Biodegradable polymers as biomaterials. *Prog. Polym. Sci.* **2007**, *32*, 762–798.
73. Ignatius, A.A.; Claes, L.E. In vitro biocompatibility of bioresorbable polymers: poly(L, DL-lactide) and poly(L-lactide-co-glycolide). *Biomaterials* **1996**, *17*, 831–839.
74. Naahidi, S.; Jafari, M.; Logan, M.; Wang, Y.; Yuan, Y.; Bae, H.; Dixon, B.; Chen, P. Biocompatibility of hydrogel-based scaffolds for tissue engineering applications. *Biotechnol. Adv.* **2017**, *35*, 530–544.
75. Anderson, J.M.; Shive, M.S. Biodegradation and biocompatibility of PLA and PLGA microspheres. *Adv. Drug Deliv. Rev.* **2012**, *64*, 72–82.
76. Böstman, O.; Pihlajamäki, H. Clinical biocompatibility of biodegradable orthopaedic implants for internal fixation: a review. *Biomaterials* **2000**, *21*, 2615–2621.
77. Albrektsson, T.; Johansson, C. Osteoinduction, osteoconduction and osseointegration. *Eur. Spine J.* **2001**, *10*, S96–S101.
78. Rahaman, M.N.; Day, D.E.; Bal, B.S.; Fu, Q.; Jung, S.B.; Bonewald, L.F.; Tomsia, A.P. Bioactive glass in tissue engineering. *Acta Biomater.* **2011**, *7*, 2355–2373.
79. Hench, L.L. Genetic design of bioactive glass. *J. Eur. Ceram. Soc.* **2009**, *29*, 1257–1265.
80. Jell, G.; Stevens, M.M. Gene activation by bioactive glasses. *J. Mater. Sci. Mater. Med.* **2006**, *17*, 997–1002.
81. Cao, W.; Hench, L.L. Bioactive materials. *Ceram. Int.* **1996**, *22*, 493–507.
82. Oonishi, H.; Hench, L.L.; Wilson, J.; Sugihara, F.; Tsuji, E.; Matsuura, M.; Kin, S.; Yamamoto, T.; Mizokawa, S. Quantitative comparison of bone growth behavior in granules of Bioglass®, A-W glass-ceramic, and hydroxyapatite. *J. Biomed. Mater. Res.* **2000**, *51*, 37–46.
83. Ghosh, S.K.; Nandi, S.K.; Kundu, B.; Datta, S.; De, D.K.; Roy, S.K.; Basu, D. In vivo response of porous hydroxyapatite and β -tricalcium phosphate prepared by aqueous solution combustion method and comparison with bioglass scaffolds. *J. Biomed. Mater. Res. B Appl. Biomater.* **2008**, *86B*, 217–227.
84. Pan, H.; Zhao, X.; Darvell, B.W.; Lu, W.W. Apatite-formation ability – Predictor of “bioactivity”? *Acta Biomater.* **2010**, *6*, 4181–4188.
85. Saravanapavan, P.; Jones, J.R.; Pryce, R.S.; Hench, L.L. Bioactivity of gel–glass powders in the CaO–SiO₂ system: A comparison with ternary (CaO–P₂P₅–SiO₂) and quaternary glasses (SiO₂–CaO–P₂O₅–Na₂O). *J. Biomed. Mater. Res. A* **2003**, *66A*, 110–119.
86. Zhu, Y.; Kaskel, S. Comparison of the in vitro bioactivity and drug release property of mesoporous bioactive glasses (MBGs) and bioactive glasses (BGs) scaffolds. *Microporous Mesoporous Mater.* **2009**, *118*, 176–182.
87. Alemany, M.I.; Velasquez, P.; de la Casa-Lillo, M.A.; De Aza, P.N. Effect of materials’ processing methods on the ‘in vitro’ bioactivity of wollastonite glass-ceramic materials. *J. Non-Cryst. Solids* **2005**, *351*, 1716–1726.
88. Kokubo, T.; Kushitani, H.; Sakka, S.; Kitsugi, T.; Yamamuro, T. Solutions able to reproduce in vivo surface-structure changes in bioactive glass-ceramic A-W. *J. Biomed. Mater. Res.* **1990**, *24*, 721–734.
89. Maçon, A.L.B.; Kim, T.B.; Valliant, E.M.; Goetschius, K.; Brow, R.K.; Day, D.E.; Hoppe, A.; Boccaccini, A.R.; Kim, I.Y.; Ohtsuki, C.; et al. A unified in vitro evaluation for apatite-forming ability of bioactive glasses and their variants. *J. Mater. Sci. Mater. Med.* **2015**, *26*, 115.
90. Kokubo, T.; Takadama, H. Simulated Body Fluid (SBF) as a Standard Tool to Test the Bioactivity of Implants. In *Handbook of Biomineralization*; John Wiley & Sons, Ltd, 2008; pp. 97–109 ISBN 978-3-527-61944-3.
91. Bohner, M.; Lemaître, J. Can bioactivity be tested in vitro with SBF solution? *Biomaterials* **2009**, *30*, 2175–2179.
92. Kokubo, T.; Takadama, H. How useful is SBF in predicting in vivo bone bioactivity? *Biomaterials* **2006**, *27*, 2907–2915.
93. Hench, L.L. Bioactive Ceramics. *Ann. N. Y. Acad. Sci.* **1988**, *523*, 54–71.
94. Brauer, D.S. Bioactive Glasses—Structure and Properties. *Angew. Chem. Int. Ed.* **2015**, *54*, 4160–4181.
95. Chen, X.; Chen, X.; Brauer, D.S.; Wilson, R.M.; Law, R.V.; Hill, R.G.; Karpukhina, N. Sodium is not essential for high bioactivity of glasses. *Int. J. Appl. Glass Sci.* **2017**, *8*, 428–437.
96. Kansal, I.; Reddy, A.; Muñoz, F.; Choi, S.-J.; Kim, H.-W.; Tulyaganov, D.U.; Ferreira, J.M.F. Structure, biodegradation behavior and cytotoxicity of alkali-containing alkaline-earth phosphosilicate glasses. *Mater. Sci. Eng. C* **2014**, *44*, 159–165.

97. Tilocca, A.; Cormack, A.N. Structural Effects of Phosphorus Inclusion in Bioactive Silicate Glasses. *J. Phys. Chem. B* **2007**, *111*, 14256–14264.
98. Goel, A.; Kapoor, S.; Rajagopal, R.R.; Pascual, M.J.; Kim, H.-W.; Ferreira, J.M.F. Alkali-free bioactive glasses for bone tissue engineering: A preliminary investigation. *Acta Biomater.* **2012**, *8*, 361–372.
99. Elgayar, I.; Aliev, A.E.; Boccaccini, A.R.; Hill, R.G. Structural analysis of bioactive glasses. *J. Non-Cryst. Solids* **2005**, *351*, 173–183.
100. Lockyer, M.W.G.; Holland, D.; Dupree, R. NMR investigation of the structure of some bioactive and related glasses. *J. Non-Cryst. Solids* **1995**, *188*, 207–219.
101. Hill, R.G.; Brauer, D.S. Predicting the bioactivity of glasses using the network connectivity or split network models. *J. Non-Cryst. Solids* **2011**, *357*, 3884–3887.
102. Edén, M. The split network analysis for exploring composition–structure correlations in multi-component glasses: I. Rationalizing bioactivity-composition trends of bioglasses. *J. Non-Cryst. Solids* **2011**, *357*, 1595–1602.
103. Watts, S.J.; Hill, R.G.; O'Donnell, M.D.; Law, R.V. Influence of magnesia on the structure and properties of bioactive glasses. *J. Non-Cryst. Solids* **2010**, *356*, 517–524.
104. Pereira, M.M.; Clark, A.E.; Hench, L.L. Calcium phosphate formation on sol-gel-derived bioactive glasses in vitro. *J. Biomed. Mater. Res.* **1994**, *28*, 693–698.
105. Sepulveda, P.; Jones, J.R.; Hench, L.L. Characterization of melt-derived 45S5 and sol-gel-derived 58S bioactive glasses. *J. Biomed. Mater. Res.* **2001**, *58*, 734–740.
106. Li, R.; Clark, A.E.; Hench, L.L. An investigation of bioactive glass powders by sol-gel processing. *J. Appl. Biomater.* **1991**, *2*, 231–239.
107. Chen, X.; Meng, Y.; Li, Y.; Zhao, N. Investigation on bio-mineralization of melt and sol-gel derived bioactive glasses. *Appl. Surf. Sci.* **2008**, *255*, 562–564.
108. Shie, M.-Y.; Ding, S.-J.; Chang, H.-C. The role of silicon in osteoblast-like cell proliferation and apoptosis. *Acta Biomater.* **2011**, *7*, 2604–2614.
109. Henstock, J.R.; Canham, L.T.; Anderson, S.I. Silicon: The evolution of its use in biomaterials. *Acta Biomater.* **2015**, *11*, 17–26.
110. Aminian, A.; Solati-Hashjin, M.; Samadikuchaksaraei, A.; Bakhshi, F.; Gorjipour, F.; Farzadi, A.; Moztarzadeh, F.; Schmücker, M. Synthesis of silicon-substituted hydroxyapatite by a hydrothermal method with two different phosphorous sources. *Ceram. Int.* **2011**, *37*, 1219–1229.
111. Khan, A.F.; Saleem, M.; Afzal, A.; Ali, A.; Khan, A.; Khan, A.R. Bioactive behavior of silicon substituted calcium phosphate based bioceramics for bone regeneration. *Mater. Sci. Eng. C* **2014**, *35*, 245–252.
112. Barradas, A.M.C.; Fernandes, H.A.M.; Groen, N.; Chai, Y.C.; Schrooten, J.; van de Peppel, J.; van Leeuwen, J.P.T.M.; van Blitterswijk, C.A.; de Boer, J. A calcium-induced signaling cascade leading to osteogenic differentiation of human bone marrow-derived mesenchymal stromal cells. *Biomaterials* **2012**, *33*, 3205–3215.
113. An, S.; Gao, Y.; Ling, J.; Wei, X.; Xiao, Y. Calcium ions promote osteogenic differentiation and mineralization of human dental pulp cells: implications for pulp capping materials. *J. Mater. Sci. Mater. Med.* **2012**, *23*, 789–795.
114. Kajiya, H. Calcium Signaling in Osteoclast Differentiation and Bone Resorption. In *Calcium Signaling*; Islam, Md.S., Ed.; Advances in Experimental Medicine and Biology; Springer Netherlands: Dordrecht, 2012; pp. 917–932 ISBN 978-94-007-2888-2.
115. Diba, M.; Tapia, F.; Boccaccini, A.R.; Strobel, L.A. Magnesium-Containing Bioactive Glasses for Biomedical Applications. *Int. J. Appl. Glass Sci.* **2012**, *3*, 221–253.
116. Diba, M.; Goudouri, O.-M.; Tapia, F.; Boccaccini, A.R. Magnesium-containing bioactive polycrystalline silicate-based ceramics and glass-ceramics for biomedical applications. *Curr. Opin. Solid State Mater. Sci.* **2014**, *18*, 147–167.
117. Nabyouni, M.; Brückner, T.; Zhou, H.; Gbureck, U.; Bhaduri, S.B. Magnesium-based bioceramics in orthopedic applications. *Acta Biomater.* **2018**, *66*, 23–43.
118. Zhang, Y.; Wei, L.; Chang, J.; Miron, R.J.; Shi, B.; Yi, S.; Wu, C. Strontium-incorporated mesoporous bioactive glass scaffolds stimulating in vitro proliferation and differentiation of bone marrow stromal cells and in vivo regeneration of osteoporotic bone defects. *J. Mater. Chem. B* **2013**, *1*, 5711–5722.
119. O'Donnell, M.D.; Hill, R.G. Influence of strontium and the importance of glass chemistry and structure when designing bioactive glasses for bone regeneration. *Acta Biomater.* **2010**, *6*, 2382–2385.
120. Gentleman, E.; Fredholm, Y.C.; Jell, G.; Lotfibakhshaiesh, N.; O'Donnell, M.D.; Hill, R.G.; Stevens, M.M. The effects of strontium-substituted bioactive glasses on osteoblasts and osteoclasts in vitro. *Biomaterials* **2010**, *31*, 3949–3956.

121. Sabareeswaran, A.; Basu, B.; Shenoy, S.J.; Jaffer, Z.; Saha, N.; Stamboulis, A. Early osseointegration of a strontium containing glass ceramic in a rabbit model. *Biomaterials* **2013**, *34*, 9278–9286.
122. Gorustovich, A.A.; Steimetz, T.; Cabrini, R.L.; López, J.M.P. Osteoconductivity of strontium-doped bioactive glass particles: A histomorphometric study in rats. *J. Biomed. Mater. Res. A* **2010**, *92A*, 232–237.
123. Hasan, J.; Crawford, R.J.; Ivanova, E.P. Antibacterial surfaces: the quest for a new generation of biomaterials. *Trends Biotechnol.* **2013**, *31*, 295–304.
124. van Oosten, M.; Schäfer, T.; Gazendam, J.A.C.; Ohlsen, K.; Tsompanidou, E.; de Goffau, M.C.; Harmsen, H.J.M.; Crane, L.M.A.; Lim, E.; Francis, K.P.; et al. Real-time in vivo imaging of invasive- and biomaterial-associated bacterial infections using fluorescently labelled vancomycin. *Nat. Commun.* **2013**, *4*, 2584.
125. Xie, Y.; He, Y.; Irwin, P.L.; Jin, T.; Shi, X. Antibacterial Activity and Mechanism of Action of Zinc Oxide Nanoparticles against *Campylobacter jejuni*. *Appl. Environ. Microbiol.* **2011**, *77*, 2325–2331.
126. Raghupathi, K.R.; Koodali, R.T.; Manna, A.C. Size-Dependent Bacterial Growth Inhibition and Mechanism of Antibacterial Activity of Zinc Oxide Nanoparticles. *Langmuir* **2011**, *27*, 4020–4028.
127. Qi, K.; Cheng, B.; Yu, J.; Ho, W. Review on the improvement of the photocatalytic and antibacterial activities of ZnO. *J. Alloys Compd.* **2017**, *727*, 792–820.
128. Yazdi, A.R.; Torkan, L.; Stone, W.; Towler, M.R. The impact of gallium content on degradation, bioactivity, and antibacterial potency of zinc borate bioactive glass. *J. Biomed. Mater. Res. B Appl. Biomater.* **2018**, *106*, 367–376.
129. BAGHBANI, F.; MOZTARZADEH, F.; HAJIBAKI, L.; MOZAFARI, M. Synthesis, characterization and evaluation of bioactivity and antibacterial activity of quinary glass system (SiO₂–CaO–P₂O₅–MgO–ZnO): In vitro study. *Bull. Mater. Sci.* **2013**, *36*, 1339–1346.
130. Sánchez-Salcedo, S.; Shruti, S.; J. Salinas, A.; Malavasi, G.; Menabue, L.; Vallet-Regí, M. In vitro antibacterial capacity and cytocompatibility of SiO₂–CaO–P₂O₅ meso-macroporous glass scaffolds enriched with ZnO. *J. Mater. Chem. B* **2014**, *2*, 4836–4847.
131. Balasubramanian, P.; Büttner, T.; Miguez Pacheco, V.; Boccaccini, A.R. Boron-containing bioactive glasses in bone and soft tissue engineering. *J. Eur. Ceram. Soc.* **2018**, *38*, 855–869.
132. Durand, L.A.H.; E. Vargas, G.; M. Romero, N.; Vera-Mesones, R.; M. Porto-López, J.; R. Boccaccini, A.; P. Zago, M.; Baldi, A.; Gorustovich, A. Angiogenic effects of ionic dissolution products released from a boron-doped 45S5 bioactive glass. *J. Mater. Chem. B* **2015**, *3*, 1142–1148.
133. Kargozar, S.; Bairo, F.; Hamzehlou, S.; Hill, R.G.; Mozafari, M. Bioactive Glasses: Sprouting Angiogenesis in Tissue Engineering. *Trends Biotechnol.* **2018**, *36*, 430–444.
134. Balasubramanian, P.; Hupa, L.; Jokic, B.; Detsch, R.; Grünewald, A.; Boccaccini, A.R. Angiogenic potential of boron-containing bioactive glasses: in vitro study. *J. Mater. Sci.* **2017**, *52*, 8785–8792.
135. Durand, L.A.H.; Góngora, A.; López, J.M.P.; R. Boccaccini, A.; Paola Zago, M.; Baldi, A.; Gorustovich, A. In vitro endothelial cell response to ionic dissolution products from boron-doped bioactive glass in the SiO₂–CaO–P₂O₅–Na₂O system. *J. Mater. Chem. B* **2014**, *2*, 7620–7630.
136. Clupper, D.C.; Hench, L.L. Crystallization kinetics of tape cast bioactive glass 45S5. *J. Non-Cryst. Solids* **2003**, *318*, 43–48.
137. Lefebvre, L.; Chevalier, J.; Gremillard, L.; Zenati, R.; Thollet, G.; Bernache-Assolant, D.; Govin, A. Structural transformations of bioactive glass 45S5 with thermal treatments. *Acta Mater.* **2007**, *55*, 3305–3313.
138. Plewinski, M.; Schickle, K.; Lindner, M.; Kirsten, A.; Weber, M.; Fischer, H. The effect of crystallization of bioactive bioglass 45S5 on apatite formation and degradation. *Dent. Mater.* **2013**, *29*, 1256–1264.
139. Peitl, O.; Dutra Zanotto, E.; Hench, L.L. Highly bioactive P₂O₅–Na₂O–CaO–SiO₂ glass-ceramics. *J. Non-Cryst. Solids* **2001**, *292*, 115–126.
140. Buchanan, L.A.; El-Ghannam, A. Effect of bioactive glass crystallization on the conformation and bioactivity of adsorbed proteins. *J. Biomed. Mater. Res. A* **2010**, *93A*, 537–546.
141. Brink, M. The influence of alkali and alkaline earths on the working range for bioactive glasses. *J. Biomed. Mater. Res.* **1997**, *36*, 109–117.
142. Lichte, P.; Pape, H.C.; Pufe, T.; Kobbe, P.; Fischer, H. Scaffolds for bone healing: Concepts, materials and evidence. *Injury* **2011**, *42*, 569–573.
143. Bose, S.; Roy, M.; Bandyopadhyay, A. Recent advances in bone tissue engineering scaffolds. *Trends Biotechnol.* **2012**, *30*, 546–554.

144. Saiz, E.; Gremillard, L.; Menendez, G.; Miranda, P.; Gryn, K.; Tomsia, A.P. Preparation of porous hydroxyapatite scaffolds. *Mater. Sci. Eng. C* **2007**, *27*, 546–550.
145. Lacroix, J.; Jallot, E.; Lao, J. Gelatin-bioactive glass composites scaffolds with controlled macroporosity. *Chem. Eng. J.* **2014**, *256*, 9–13.
146. Wu, Z.Y.; Hill, R.G.; Yue, S.; Nightingale, D.; Lee, P.D.; Jones, J.R. Melt-derived bioactive glass scaffolds produced by a gel-cast foaming technique. *Acta Biomater.* **2011**, *7*, 1807–1816.
147. Jones, J.R.; Hench, L.L. Factors affecting the structure and properties of bioactive foam scaffolds for tissue engineering. *J. Biomed. Mater. Res. B Appl. Biomater.* **2004**, *68B*, 36–44.
148. Deville, S.; Saiz, E.; Tomsia, A.P. Freeze casting of hydroxyapatite scaffolds for bone tissue engineering. *Biomaterials* **2006**, *27*, 5480–5489.
149. Liu, X.; Rahaman, M.N.; Fu, Q. Oriented bioactive glass (13-93) scaffolds with controllable pore size by unidirectional freezing of camphene-based suspensions: Microstructure and mechanical response. *Acta Biomater.* **2011**, *7*, 406–416.
150. Chen, Q.Z.; Thompson, I.D.; Boccaccini, A.R. 45S5 Bioglass®-derived glass–ceramic scaffolds for bone tissue engineering. *Biomaterials* **2006**, *27*, 2414–2425.
151. Eqtessadi, S.; Motealleh, A.; Miranda, P.; Pajares, A.; Lemos, A.; Ferreira, J.M.F. Robocasting of 45S5 bioactive glass scaffolds for bone tissue engineering. *J. Eur. Ceram. Soc.* **2014**, *34*, 107–118.
152. González, P.; Serra, J.; Liste, S.; Chiussi, S.; León, B.; Pérez-Amor, M.; Martínez-Fernández, J.; de Arellano-López, A.R.; Varela-Feria, F.M. New biomorphic SiC ceramics coated with bioactive glass for biomedical applications. *Biomaterials* **2003**, *24*, 4827–4832.
153. Blaker, J.J.; Nazhat, S.N.; Boccaccini, A.R. Development and characterisation of silver-doped bioactive glass-coated sutures for tissue engineering and wound healing applications. *Biomaterials* **2004**, *25*, 1319–1329.
154. Pratten, J.; Nazhat, S.N.; Blaker, J.J.; Boccaccini, A.R. In Vitro Attachment of Staphylococcus Epidermidis to Surgical Sutures with and without Ag-Containing Bioactive Glass Coating. *J. Biomater. Appl.* **2004**, *19*, 47–57.
155. Bosetti, M.; Vernè, E.; Ferraris, M.; Ravaglioli, A.; Cannas, M. In vitro characterisation of zirconia coated by bioactive glass. *Biomaterials* **2001**, *22*, 987–994.
156. Schrooten, J.; Helsen, J.A. Adhesion of bioactive glass coating to Ti6Al4V oral implant. *Biomaterials* **2000**, *21*, 1461–1469.
157. Lopez-Esteban, S.; Saiz, E.; Fujino, S.; Oku, T.; Suganuma, K.; Tomsia, A.P. Bioactive glass coatings for orthopedic metallic implants. *J. Eur. Ceram. Soc.* **2003**, *23*, 2921–2930.
158. Gomez-Vega, J.M.; Saiz, E.; Tomsia, A.P.; Marshall, G.W.; Marshall, S.J. Bioactive glass coatings with hydroxyapatite and Bioglass® particles on Ti-based implants. 1. Processing. *Biomaterials* **2000**, *21*, 105–111.
159. Zhuo, R.; Colombo, P.; Pantano, C.; Vogler, E.A. Silicon oxycarbide glasses for blood-contact applications. *Acta Biomater.* **2005**, *1*, 583–589.
160. Whitehurst, T.K.; McGivern, J.P.; Woods, C.M.; Meadows, P.M.; Kuzma, J.A. Fully implantable miniature neurostimulator for stimulation as a therapy for headache and/or facial pain 2004.
161. Franzini, A.; Ferrolì, P.; Servello, D.; Broggi, G. Reversal of thalamic hand syndrome by long-term motor cortex stimulation: Case report. *J. Neurosurg.* **2000**, *93*, 873–875.
162. Grossenbacher, J.; Gullo, M.R.; Dalcanele, F.; Blugan, G.; Kuebler, J.; Lecaudé, S.; Stahel, H.T.; Brugger, J. Cytotoxicity evaluation of polymer-derived ceramics for pacemaker electrode applications. *J. Biomed. Mater. Res. A* **2015**, *103*, 3625–3632.
163. Sorarù, G.D.; Modena, S.; Guadagnino, E.; Colombo, P.; Egan, J.; Pantano, C. Chemical Durability of Silicon Oxycarbide Glasses. *J. Am. Ceram. Soc.* **2002**, *85*, 1529–1536.
164. Cogan, S.F. Biomedical device with a protective overlayer 1998.
165. Sasikumar, P.V.W.; Blugan, G.; Casati, N.; Kakkava, E.; Panusa, G.; Psaltis, D.; Kuebler, J. Polymer derived silicon oxycarbide ceramic monoliths: Microstructure development and associated materials properties. *Ceram. Int.* **2018**, *44*, 20961–20967.
166. Dalcanele, F.; Grossenbacher, J.; Blugan, G.; Gullo, M.R.; Lauria, A.; Brugger, J.; Tevaearai, H.; Graule, T.; Niederberger, M.; Kuebler, J. Influence of carbon enrichment on electrical conductivity and processing of polycarbosilane derived ceramic for MEMS applications. *J. Eur. Ceram. Soc.* **2014**, *34*, 3559–3570.
167. Kaspar, J.; Graczyk-Zajac, M.; Choudhury, S.; Riedel, R. Impact of the electrical conductivity on the lithium capacity of polymer-derived silicon oxycarbide (SiOC) ceramics. *Electrochimica Acta* **2016**, *216*, 196–202.
168. Perale, G.; Giordano, C.; Daniele, F.; Tunesi, M.; Colombo, P.; Gottardo, L.; Maccagnan, S.; Masi, M. Extruded Ceramic Microelectrodes for Biomedical Applications. *Int. J. Artif. Organs* **2008**, *31*, 272–278.

169. Bigerelle, M.; Anselme, K.; Noël, B.; Ruderman, I.; Hardouin, P.; Iost, A. Improvement in the morphology of Ti-based surfaces: a new process to increase in vitro human osteoblast response. *Biomaterials* **2002**, *23*, 1563–1577.
170. Hallab, N.J.; Bundy, K.J.; O'Connor, K.; Moses, R.L.; Jacobs, J.J. Evaluation of Metallic and Polymeric Biomaterial Surface Energy and Surface Roughness Characteristics for Directed Cell Adhesion. *Tissue Eng.* **2001**, *7*, 55–71.
171. Nakamura, M.; Hori, N.; Ando, H.; Namba, S.; Toyama, T.; Nishimiya, N.; Yamashita, K. Surface free energy predominates in cell adhesion to hydroxyapatite through wettability. *Mater. Sci. Eng. C* **2016**, *62*, 283–292.
172. Ueno, H.; Inoue, M.; Okonogi, A.; Kotera, H.; Suzuki, T. Correlation between Cells-on-Chips materials and cell adhesion/proliferation focused on material's surface free energy. *Colloids Surf. Physicochem. Eng. Asp.* **2019**, *565*, 188–194.
173. Tamayo, A.; Peña-Alonso, R.; Rubio, J.; Raj, R.; Sorarù, G.D.; Oteo, J.L. Surface Energy of Sol Gel-Derived Silicon Oxycarbide Glasses. *J. Am. Ceram. Soc.* **2011**, *94*, 4523–4533.
174. Barralet, J.; Gbureck, U.; Habibovic, P.; Vorndran, E.; Gerard, C.; Doillon, C.J. Angiogenesis in calcium phosphate scaffolds by inorganic copper ion release. *Tissue Eng. Part A* **2009**, *15*, 1601–1609.
175. Wu, C.; Zhou, Y.; Fan, W.; Han, P.; Chang, J.; Yuen, J.; Zhang, M.; Xiao, Y. Hypoxia-mimicking mesoporous bioactive glass scaffolds with controllable cobalt ion release for bone tissue engineering. *Biomaterials* **2012**, *33*, 2076–2085.
176. Tamayo, A.; Mazo, M.A.; Ruiz-Caro, R.; Martín-Illana, A.; Bedoya, L.M.; Veiga-Ochoa, M.D.; Rubio, J. Mesoporous silicon oxycarbide materials for controlled drug delivery systems. *Chem. Eng. J.* **2015**, *280*, 165–174.
177. Khalilpour, P.; Lampe, K.; Wagener, M.; Stigler, B.; Heiss, C.; Ullrich, M.S.; Domann, E.; Schnettler, R.; Alt, V. Ag/SiO(x)C(y) plasma polymer coating for antimicrobial protection of fracture fixation devices. *J. Biomed. Mater. Res. B Appl. Biomater.* **2010**, *94*, 196–202.
178. Guo, A.; Roso, M.; Colombo, P.; Liu, J.; Modesti, M. In situ carbon thermal reduction method for the production of electrospun metal/SiOC composite fibers. *J. Mater. Sci.* **2015**, *50*, 2735–2746.
179. Hojamberdiev, M.; Prasad, R.M.; Morita, K.; Schiavon, M.A.; Riedel, R. Polymer-derived mesoporous SiOC/ZnO nanocomposite for the purification of water contaminated with organic dyes. *Microporous Mesoporous Mater.* **2012**, *151*, 330–338.
180. Vallet-Regí, M.; Balas, F.; Arcos, D. Mesoporous Materials for Drug Delivery. *Angew. Chem. Int. Ed.* **2007**, *46*, 7548–7558.
181. Tamayo, A.; Ruiz-Caro, R.; Mazo, A.; Veiga-Ochoa, M.D.; Rubio, J. Chemical oxidation of silicon oxycarbide ceramics for advanced drug delivery systems. *J. Mater. Sci.* **2016**, *51*, 1382–1391.
182. Vakifahmetoglu, C.; Zeydanli, D.; Ozalp, V.C.; Borsa, B.A.; Soraru, G.D. Hierarchically porous polymer derived ceramics: A promising platform for multidrug delivery systems. *Mater. Des.* **2018**, *140*, 37–44.
183. Suárez, F.J.; Sevilla, M.; Álvarez, S.; Valdés-Solís, T.; Fuertes, A.B. Synthesis of Highly Uniform Mesoporous Sub-Micrometric Capsules of Silicon Oxycarbide and Silica. *Chem. Mater.* **2007**, *19*, 3096–3098.
184. Caruso, F. Nanoengineering of Particle Surfaces. *Adv. Mater.* **2001**, *13*, 11–22.
185. Bennett, A.E.; Rienstra, C.M.; Auger, M.; Lakshmi, K.V.; Griffin, R.G. Heteronuclear decoupling in rotating solids. *J. Chem. Phys.* **1995**, *103*, 6951–6958.
186. Jaeger, C.; Hemmann, F. EASY: a simple tool for simultaneously removing background, dead-time and acoustic ringing in quantitative NMR spectroscopy--part I: basic principle and applications. *Solid State Nucl. Magn. Reson.* **2014**, *57–58*, 22–28.
187. Sze, A.; Erickson, D.; Ren, L.; Li, D. Zeta-potential measurement using the Smoluchowski equation and the slope of the current–time relationship in electroosmotic flow. *J. Colloid Interface Sci.* **2003**, *261*, 402–410.
188. Brunauer, S.; Emmett, P.H.; Teller, E. Adsorption of Gases in Multimolecular Layers. *J. Am. Chem. Soc.* **1938**, *60*, 309–319.
189. Barrett, E.P.; Joyner, L.G.; Halenda, P.P. The Determination of Pore Volume and Area Distributions in Porous Substances. I. Computations from Nitrogen Isotherms. *J. Am. Chem. Soc.* **1951**, *73*, 373–380.
190. Pearson, R.G.; Moore, J.W. The Rates and Mechanism of Hydrolysis Reactions of Some Metal Acetylacetonates. *Inorg. Chem.* **1966**, *5*, 1528–1532.
191. Rudolph, G.; Henry, M.C. The Thermal Decomposition of Zinc Acetylacetonate Hydrate. *Inorg. Chem.* **1964**, *3*, 1317–1318.

192. Hoene, J.V.; Charles, R.G.; Hickam, W.M. Thermal Decomposition of Metal Acetylacetonates: Mass Spectrometer Studies. *J. Phys. Chem.* **1958**, *62*, 1098–1101.
193. Mehrotra, R.K.; Mehrotra, R.C. Reactions of Aluminium Alkoxides with Acetylacetone, Benzoylacetone, and Ethyl Acetoacetate. *Can. J. Chem.* **1961**, *39*, 795–798.
194. Tamayo, A.; Peña-Alonso, R.; Rubio, F.; Rubio, J.; Oteo, J.L. Synthesis and characterization of boron silicon oxycarbide glass fibers. *J. Non-Cryst. Solids* **2012**, *358*, 155–162.
195. Kalampounias, A.G. IR and Raman spectroscopic studies of sol–gel derived alkaline-earth silicate glasses. *Bull. Mater. Sci.* **2011**, *34*, 299–303.
196. Schiavon, M.A.; Armelin, N.A.; Yoshida, I.V.P. Novel poly(borosiloxane) precursors to amorphous SiBCO ceramics. *Mater. Chem. Phys.* **2008**, *112*, 1047–1054.
197. Balamurugan, A.; Sockalingum, G.; Michel, J.; Fauré, J.; Banchet, V.; Wortham, L.; Bouthors, S.; Laurent-Maquin, D.; Balossier, G. Synthesis and characterisation of sol gel derived bioactive glass for biomedical applications. *Mater. Lett.* **2006**, *60*, 3752–3757.
198. Serra, J.; González, P.; Liste, S.; Serra, C.; Chiussi, S.; León, B.; Pérez-Amor, M.; Ylänen, H.O.; Hupa, M. FTIR and XPS studies of bioactive silica based glasses. *J. Non-Cryst. Solids* **2003**, *332*, 20–27.
199. Rokita, M.; Mozgawa, W.; Adamczyk, A. Transformation of silicate gels during heat treatment in air and in argon – Spectroscopic studies. *J. Mol. Struct.* **2014**, *1070*, 125–130.
200. Tavakoli, A.H.; Campostrini, R.; Gervais, C.; Babonneau, F.; Bill, J.; Sorarù, G.D.; Navrotsky, A. Energetics and Structure of Polymer-Derived Si–(B–)O–C Glasses: Effect of the Boron Content and Pyrolysis Temperature. *J. Am. Ceram. Soc.* **2014**, *97*, 303–309.
201. Sorarù, G.D.; Dallabona, N.; Gervais, C.; Babonneau, F. Organically Modified SiO₂–B₂O₃ Gels Displaying a High Content of Borosiloxane (B–O–Si) Bonds. *Chem. Mater.* **1999**, *11*, 910–919.
202. Gaillardet, J.; Lemarchand, D.; Göpel, C.; Manhès, G. Evaporation and Sublimation of Boric Acid: Application for Boron Purification from Organic Rich Solutions. *Geostand. Newsl.* **2007**, *25*, 67–75.
203. White, J.F.; Lee, J.; Hessling, O.; Glaser, B. Reactions Between Liquid CaO–SiO₂ Slags and Graphite Substrates. *Metall. Mater. Trans. B* **2017**, *48*, 506–515.
204. Saravanapavan, P.; Hench, L.L. Mesoporous calcium silicate glasses. I. Synthesis. *J. Non-Cryst. Solids* **2003**, *318*, 1–13.
205. Fiocco, L.; Elsayed, H.; Badocco, D.; Pastore, P.; Bellucci, D.; Cannillo, V.; Detsch, R.; Boccacini, A.R.; Bernardo, E. Direct ink writing of silica-bonded calcite scaffolds from preceramic polymers and fillers. *Biofabrication* **2017**, *9*, 025012.
206. Elsayed, H.; Carraro, F.; Agnoli, S.; Bellucci, D.; Cannillo, V.; Ferroni, L.; Gardin, C.; Zavan, B.; Bernardo, E. Direct ink writing of silica-carbon-calcite composite scaffolds from a silicone resin and fillers. *J. Eur. Ceram. Soc.* **2018**, *38*, 5200–5207.
207. Sing, K.S.W. Reporting physisorption data for gas/solid systems with special reference to the determination of surface area and porosity (Recommendations 1984). *Pure Appl. Chem.* **1985**, *57*, 603–619.
208. Zhong, J.; Greenspan, D.C. Processing and properties of sol–gel bioactive glasses. *J. Biomed. Mater. Res.* **2000**, *53*, 694–701.
209. Ciraldo, F.E.; Boccardi, E.; Melli, V.; Westhauser, F.; Boccaccini, A.R. Tackling bioactive glass excessive in vitro bioreactivity: Preconditioning approaches for cell culture tests. *Acta Biomater.* **2018**, *75*, 3–10.
210. Rámila, A.; Vallet-Regí, M. Static and dynamic in vitro study of a sol–gel glass bioactivity. *Biomaterials* **2001**, *22*, 2301–2306.
211. Cerruti, M.; Greenspan, D.; Powers, K. Effect of pH and ionic strength on the reactivity of Bioglass® 45S5. *Biomaterials* **2005**, *26*, 1665–1674.
212. Arcos, D.; Greenspan, D.C.; Vallet-Regí, M. A new quantitative method to evaluate the in vitro bioactivity of melt and sol-gel-derived silicate glasses. *J. Biomed. Mater. Res. A* **2003**, *65A*, 344–351.
213. Xu, G.; Zhang, J.; Song, G. Effect of complexation on the zeta potential of silica powder. *Powder Technol.* **2003**, *134*, 218–222.
214. Fisher, M.L.; Colic, M.; Rao, M.P.; Lange, F.F. Effect of Silica Nanoparticle Size on the Stability of Alumina/Silica Suspensions. *J. Am. Ceram. Soc.* **2001**, *84*, 713–718.
215. Li, W.; Chen, P.; Gu, M.; Jin, Y. Effect of TMAH on rheological behavior of SiC aqueous suspension. *J. Eur. Ceram. Soc.* **2004**, *24*, 3679–3684.
216. Mori, T.; Kitamura, K. Effect of adsorption behaviour of polyelectrolytes on fluidity and packing ability of aqueous graphite slurries. *Adv. Powder Technol.* **2017**, *28*, 280–287.

217. Perera, G.; Doremus, R.H.; Lanford, W. Dissolution Rates of Silicate Glasses in Water at pH 7. *J. Am. Ceram. Soc.* **1991**, *74*, 1269–1274.
218. Viallis-Terrisse, H.; Nonat, A.; Petit, J.-C. Zeta-Potential Study of Calcium Silicate Hydrates Interacting with Alkaline Cations. *J. Colloid Interface Sci.* **2001**, *244*, 58–65.
219. Diaz-Cano, A.; Trice, R.W.; Youngblood, J.P. Stabilization of highly-loaded boron carbide aqueous suspensions. *Ceram. Int.* **2017**, *43*, 8572–8578.
220. Chen, J.; Zeng, L.; Chen, X.; Liao, T.; Zheng, J. Preparation and characterization of bioactive glass tablets and evaluation of bioactivity and cytotoxicity in vitro. *Bioact. Mater.* **2018**, *3*, 315–321.
221. Chen, F.; Wang, Z.-C.; Lin, C.-J. Preparation and characterization of nano-sized hydroxyapatite particles and hydroxyapatite/chitosan nano-composite for use in biomedical materials. *Mater. Lett.* **2002**, *57*, 858–861.
222. Aguiar, H.; Serra, J.; González, P.; León, B. Structural study of sol–gel silicate glasses by IR and Raman spectroscopies. *J. Non-Cryst. Solids* **2009**, *355*, 475–480.
223. Mačković, M.; Hoppe, A.; Detsch, R.; Mohn, D.; Stark, W.J.; Spiecker, E.; Boccaccini, A.R. Bioactive glass (type 45S5) nanoparticles: in vitro reactivity on nanoscale and biocompatibility. *J. Nanoparticle Res.* **2012**, *14*, 966.
224. Ślósarczyk, A.; Paszkiewicz, Z.; Paluszkiwicz, C. FTIR and XRD evaluation of carbonated hydroxyapatite powders synthesized by wet methods. *J. Mol. Struct.* **2005**, *744–747*, 657–661.
225. Landi, E.; Celotti, G.; Logroscino, G.; Tampieri, A. Carbonated hydroxyapatite as bone substitute. *J. Eur. Ceram. Soc.* **2003**, *23*, 2931–2937.
226. Yan, H.; Zhang, K.; Blanford, C.F.; Francis, L.F.; Stein, A. In Vitro Hydroxycarbonate Apatite Mineralization of CaO–SiO₂ Sol–Gel Glasses with a Three-Dimensionally Ordered Macroporous Structure. *Chem. Mater.* **2001**, *13*, 1374–1382.
227. Cao, N.; Dong, J.; Wang, Q.; Ma, Q.; Xue, C.; Li, M. An experimental bone defect healing with hydroxyapatite coating plasma sprayed on carbon/carbon composite implants. *Surf. Coat. Technol.* **2010**, *205*, 1150–1156.
228. Kazemi, A.; Faghihi-Sani, M.A.; Alizadeh, H.R. Investigation on cristobalite crystallization in silica-based ceramic cores for investment casting. *J. Eur. Ceram. Soc.* **2013**, *33*, 3397–3402.
229. O'Donnell, M.D.; Candarlioglu, P.L.; Miller, C.A.; Gentleman, E.; Stevens, M.M. Materials characterisation and cytotoxic assessment of strontium -substituted bioactive glasses for bone regeneration. *J. Mater. Chem.* **2010**, *20*, 8934–8941.
230. Koutsoukos, P.G.; Nancollas, G.H. Influence of strontium ion on the crystallization of hydroxyapatite from aqueous solution. *J. Phys. Chem.* **1981**, *85*, 2403–2408.
231. Fredholm, Y.C.; Karpukhina, N.; Brauer, D.S.; Jones, J.R.; Law, R.V.; Hill, R.G. Influence of strontium for calcium substitution in bioactive glasses on degradation, ion release and apatite formation. *J. R. Soc. Interface* **2012**, *9*, 880–889.
232. Pan, H.-B.; Li, Z.-Y.; Wang, T.; Lam, W.M.; Wong, C.T.; Darvell, B.W.; Luk, K.D.K.; Hu, Y.; Lu, W.W. Nucleation of Strontium-Substituted Apatite. *Cryst. Growth Des.* **2009**, *9*, 3342–3345.
233. Christoffersen, J.; Christoffersen, M.R.; Kolthoff, N.; Bärenholdt, O. Effects of strontium ions on growth and dissolution of hydroxyapatite and on bone mineral detection. *Bone* **1997**, *20*, 47–54.
234. Kumar, G.S.; Girija, E.K. Flower-like hydroxyapatite nanostructure obtained from eggshell: A candidate for biomedical applications. *Ceram. Int.* **2013**, *39*, 8293–8299.
235. He, Q.; Huang, Z.; Liu, Y.; Chen, W.; Xu, T. Template-directed one-step synthesis of flowerlike porous carbonated hydroxyapatite spheres. *Mater. Lett.* **2007**, *61*, 141–143.
236. Posner, A.S.; Betts, F. Synthetic amorphous calcium phosphate and its relation to bone mineral structure. *Acc. Chem. Res.* **1975**, *8*, 273–281.
237. Singh, A.K.; Pantano, C.G. Porous Silicon Oxycarbide Glasses. *J. Am. Ceram. Soc.* **1996**, *79*, 2696–2704.
238. Yuan, X.; Jin, H.; Yan, X.; Cheng, L.; Hu, L.; Xue, Q. Synthesis of ordered mesoporous silicon oxycarbide monoliths via preceramic polymer nanocasting. *Microporous Mesoporous Mater.* **2012**, *147*, 252–258.
239. Duan, L.; Ma, Q.; Chen, Z. Preparation and characterization of mesoporous silicon oxycarbide ceramics without free carbon from polysiloxane. *J. Eur. Ceram. Soc.* **2013**, *33*, 841–846.
240. Liu, C.; Zhang, H.; Komarneni, S.; Pantano, C.G. Porous silicon oxycarbide glasses from organically modified silica gels of high surface area. *J. Sol-Gel Sci. Technol.* **1994**, *1*, 141–151.
241. Aravind, P.R.; Soraru, G.D. Porous silicon oxycarbide glasses from hybrid ambigels. *Microporous Mesoporous Mater.* **2011**, *142*, 511–517.
242. Yan, X.; Su, D.; Duan, H.; Zhang, F. Preparation of SiOC/HfO₂ fibers from silicon alkoxides and tetrachloride hafnium by a sol–gel process. *Mater. Lett.* **2015**, *148*, 196–199.

243. Wootton, A.M.; Rappensberger, M.; Lewis, M.H.; Kitchin, S.; Howes, A.P.; Dupree, R. Structural properties of multi-component silicon oxycarbide glasses derived from metal alkoxide precursors. *J. Non-Cryst. Solids* **1996**, *204*, 217–227.
244. Chen, Q.-Z.; Li, Y.; Jin, L.-Y.; Quinn, J.M.W.; Komesaroff, P.A. A new sol–gel process for producing Na₂O-containing bioactive glass ceramics. *Acta Biomater.* **2010**, *6*, 4143–4153.
245. Hurwitz, F.I.; Heimann, P.; Farmer, S.C.; Hembree, D.M. Characterization of the pyrolytic conversion of polysilsesquioxanes to silicon oxycarbides. *J. Mater. Sci.* **1993**, *28*, 6622–6630.
246. Lin, S.; Ionescu, C.; J. Pike, K.; E. Smith, M.; R. Jones, J. Nanostructure evolution and calcium distribution in sol–gel derived bioactive glass. *J. Mater. Chem.* **2009**, *19*, 1276–1282.
247. Fidalgo, A.; Ilharco, L.M. Chemical Tailoring of Porous Silica Xerogels: Local Structure by Vibrational Spectroscopy. *Chem. – Eur. J.* **2004**, *10*, 392–398.
248. Brinker, C.J.; Scherer, G.W. *Sol-Gel Science: The Physics and Chemistry of Sol-Gel Processing*; Academic Press, 2013; ISBN 978-0-08-057103-4.
249. Schitco, C.; Bazarjani, M.S.; Riedel, R.; Gurlo, A. NH₃-assisted synthesis of microporous silicon oxycarbonitride ceramics from preceramic polymers: a combined N₂ and CO₂ adsorption and small angle X-ray scattering study. *J. Mater. Chem. A* **2014**, *3*, 805–818.
250. Seifollahi Bazarjani, M.; Kleebe, H.-J.; Müller, M.M.; Fasel, C.; Baghaie Yazdi, M.; Gurlo, A.; Riedel, R. Nanoporous Silicon Oxycarbonitride Ceramics Derived from Polysilazanes In situ Modified with Nickel Nanoparticles. *Chem. Mater.* **2011**, *23*, 4112–4123.
251. Ettarh, C.; Galwey, A.K. A kinetic and mechanistic study of the thermal decomposition of calcium nitrate. *Thermochim. Acta* **1996**, *288*, 203–219.
252. Sarmiento, C.; Luklinska, Z.B.; Brown, L.; Anseau, M.; Aza, P.N.D.; Aza, S.D.; Hughes, F.J.; McKay, I.J. In vitro behavior of osteoblastic cells cultured in the presence of pseudowollastonite ceramic. *J. Biomed. Mater. Res. A* **2004**, *69A*, 351–358.
253. Fernández-Pradas, J.M.; Serra, P.; Morenza, J.L.; De Aza, P.N. Pulsed laser deposition of pseudowollastonite coatings. *Biomaterials* **2002**, *23*, 2057–2061.
254. Almasri, K.A.; Sidek, H.A.A.; Matori, K.A.; Zaid, M.H.M. Effect of sintering temperature on physical, structural and optical properties of wollastonite based glass-ceramic derived from waste soda lime silica glasses. *Results Phys.* **2017**, *7*, 2242–2247.
255. Bernardo, E. Fast sinter-crystallization of a glass from waste materials. *J. Non-Cryst. Solids* **2008**, *354*, 3486–3490.
256. Ciobanu, C.S.; Massuyeau, F.; Constantin, L.V.; Predoi, D. Structural and physical properties of antibacterial Ag-doped nano-hydroxyapatite synthesized at 100°C. *Nanoscale Res. Lett.* **2011**, *6*, 613.
257. Li, X.; Shi, J.; Dong, X.; Zhang, L.; Zeng, H. A mesoporous bioactive glass/polycaprolactone composite scaffold and its bioactivity behavior. *J. Biomed. Mater. Res. A* **2008**, *84A*, 84–91.
258. Lukito, D.; Xue, J.M.; Wang, J. In vitro bioactivity assessment of 70 (wt.%)SiO₂–30 (wt.%)CaO bioactive glasses in simulated body fluid. *Mater. Lett.* **2005**, *59*, 3267–3271.
259. Iimori, Y.; Kameshima, Y.; Okada, K.; Hayashi, S. Comparative study of apatite formation on CaSiO₃ ceramics in simulated body fluids with different carbonate concentrations. *J. Mater. Sci. Mater. Med.* **2005**, *16*, 73–79.

Acknowledgement

I would like to thank **Prof. Dr. Ralf Riedel** for giving me the chance to work on this PhD topic in Disperse Feststoffe group and his continuous support and advice for the research work.

I would express my great gratitude to **PD Dr. Emanuel Ionescu** for his valuable suggestions on my PhD plan. Besides, the inspiring discussions with him help solving research difficulties. I appreciate particularly his precious contributions to the optimization and correction of scientific writings, as well as the first survey of this thesis.

Dr. Isabel Gonzalo-Juan is greatly acknowledged for the preliminary study for this research topic. Her idea and experience on bioactive silicon oxycarbide materials have helped continuously guiding the research direction. I also thank her for the valuable discussions and the corrections of scientific writings.

Prof. Dr.-Ing. Aldo R. Boccaccini is gratefully acknowledged for the second survey of this thesis and his valuable contributions at project meetings as collaboration partner. His profound experience in bio-active material field is indispensable for the research success.

In particular, I would like to thank **Dipl.-Ing. Claudia Fasel** for her extensive and patient help with lab equipments and techniques, and also for conducting the thermogravimetric measurements and data evaluation of evolved gas analysis.

I want to thank **Dr. Kai Zheng** and **M.Sc. Marcela Arango-Ospina** for the advice on preparing simulated body liquid, for the valuable discussions about cellular assessments of bioactive materials and for providing the bioactive glass with 45S5 composition. **Dr. Hergen Breitzke** and **Prof. Dr. Gerd Buntkowsky** are gratefully acknowledged for the solid state NMR measurements and the support on data evaluation. **M.Sc. Maximilian Trapp** and **Prof. Dr. Hans-Joachim Kleebe** are gratefully acknowledged for the TEM measurements and the EDS data evaluation. **Dipl.-Geol. Christian Scholz** is gratefully acknowledged for the ICP-OES measurements. Furthermore, I would like to thank **Jean-Christophe Jaud** for the valuable discussions about the XRD measurement techniques and **Ulrike Kunz** for the elaborate instructions to the SEM equipment.

Meanwhile, I would like to thank all DF group members for the cooperative and friendly working environment. Especially, **Dr. Christina Stabler** is acknowledged for sharing her experience in dealing with polymer precursors. **Dr. Dragoljub Vrankovic** and **M.Sc. Yao Feng** are acknowledged for the valuable discussions about BET measurement.

I gratefully acknowledge the financial support of the Deutsche Forschungsgemeinschaft DFG (Project number 317658328, "Novel bioactive Si-M-O-C glasses (M = Sr, Zn, B) with outstanding high-temperature crystallization resistance").

Last but not least, I would like to express my great gratitude to my family and friends, who have accompanied me through the challenges and difficulties during the entire PhD period. Without their support, I would not be able to reach where I am now.

List of Figures

Figure 2-1. Thermal decomposition of Si-based polymers and their corresponding ceramic products [38].	4
Figure 2-2. (a) Typical ^{29}Si MAS NMR spectrum of polysiloxane derived silicon oxycarbide (solid bold line) with the simulated spectrum (dashed line) and individual simulation components (thin solid lines). The peaks (I, II, III, IV and V) correspond to SiO_4 , SiO_3C , SiO_2C_2 , SiOC_3 and SiC_4 units, respectively [51]; (b) TEM micrograph of a C-rich silicon oxycarbide sample synthesized at 1400 °C [54].	6
Figure 2-3. (a) Structural model of silicon oxycarbide, in which black regions represent “free carbon” and the patterned matrix is oxygen-rich silicon oxycarbide domains. Between the two regions lie the grey regions referring to carbon-rich silicon oxycarbide [51]; (b) Structural model of silicon oxycarbide, in which oxygen-rich silica regions are separated by “free carbon” sheets [36].	8
Figure 2-4. Thermodynamically predicted phase composition of metal modified silicon oxycarbide (Si(M)OC) upon pyrolysis from 1100-1300 °C: Red-marked metals tend to form metal oxide or metal silicate phases in silicon oxycarbide; Blue-marked metals tend to form metallic, metal silicide, metal carbide phases in silicon oxycarbide due to carbothermal reaction [17].	10
Figure 2-5. Schematic illustration of Ca^{2+} and Mg^{2+} ions incorporation in silicon oxycarbide network at non-bridging-oxygen sites.	10
Figure 2-6. Kinetically determined boundaries for SiO_2 - CaO - Na_2O glasses (with 6 wt.% P_2O_5). Depending on glass compositions, different bone-bonding behaviors (bioactivity) are to be expected [2].	13
Figure 2-7. Summary of therapeutic effects of released ions from bioactive glasses [4].	15
Figure 2-8. Human nature femur bone, with in the inset the 3D porous structure of the cancellous bone scanned by X-ray microtomography [3].	17
Figure 2-9. Summary of the biomedical applications of silicon oxycarbide materials in published research work.	19
Figure 3-1. Pyrolysis program for PMS derived silicon oxycarbides.	27
Figure 3-2. Sol-gel procedure for silicon oxycarbide xerogel precursors.	28
Figure 3-3. Pyrolysis program for sol-gel derived silicon oxycarbides.	28
Figure 4-1. (a) Thermogravimetric (TGA) curves for MK (black line), MK-B7 (green line), MK-Ca5 (red line), MK-B7Ca5 (blue line) and MK-Ca12 (orange line). The characteristic peaks of the evolved gas species are determined via in situ FTIR to be located between 758-787 cm^{-1} for $\text{C}_8\text{H}_{24}\text{O}_{12}\text{Si}_8$, 3638-3689 cm^{-1} for $\text{C}_2\text{H}_6\text{O}$, 1709-1763 cm^{-1} for $\text{C}_3\text{H}_6\text{O}$, 1594-1651 cm^{-1} for $\text{C}_5\text{H}_8\text{O}_2$, 1454-1546 cm^{-1} for H_2O , 948-952 cm^{-1} for C_2H_4 and 3011-3019 cm^{-1} for CH_4 . The individual TG curves and in situ recorded signal intensities of the characteristic IR peaks are shown in (b), (c), (d), (e), and (f), respectively.	36
Figure 4-2. Schematic illustration of the chemical modification of the polymethylsilsequioxane with boric acid and/or calcium acetylacetonate.	37
Figure 4-3. FTIR spectra of silicon oxycarbide based samples prepared upon pyrolysis of the polymethylsilsequioxane based precursors at 1100 °C.	38
Figure 4-4. XRD pattern of silicon oxycarbide based samples prepared upon pyrolysis of the corresponding precursors at 1100 °C.	39
Figure 4-5. Bright field and high resolution TEM micrographs of the samples (a) SiOC-Ca5 and (b) SiOC-B7Ca5 . The FFT (Fast Fourier transformation) and SAED (selected area electron diffraction) insets depict the amorphous or crystalline nature of the respective regions. As shown by the EDS measurements, the crystalline regions have a significantly higher Ca content than the Ca-poor amorphous parts, which is indicative for a phase separation process occurring in both samples.	40
Figure 4-6. ^{29}Si MAS NMR spectra (top black lines) of (a) SiOC-B7 , (b) SiOC-Ca5 , (c) SiOC-B7Ca5 and (d) SiOC-Ca12 . The spectra are fitted to $\text{Q}^4 \text{SiO}_4$ (peak I), $\text{Q}^3 \text{SiO}_4$ (peak II), SiO_3C (peak III), SiO_2C_2 (peak IV), SiOC_3 (peak V), SiC_4 (peak VI) and Q^2 (wollastonite / pseudowollastonite) (peak VII) sites (bottom black lines). The sum of all fitted peaks yields the blue lines in the spectra.	42
Figure 4-7. ^{11}B MAS NMR spectra (top black lines) of (a) SiOC-B7 and (b) SiOC-B7Ca5 . The fitted signals are assigned to BO_3 (I), BO_2C (II) and BOC_2 (III) sites (bottom black lines). The sum of all fitted signals yields the blue lines.	43
Figure 4-8. Evolution of (a) pH value, (b) Si concentration, (c) Ca concentration, (d) P concentration of the filtered SBF solutions as a function of the soaking time for silicon oxycarbide based and 45S5 samples.	51

Figure 4-9. Arrhenius plots of silicon release after 3 days SBF testing at 24 °C, 37 °C and 55 °C for the investigated samples.	52
Figure 4-10. (a) Evolution of surface charge during the first 8 h of the SBF test, measured on zeta potential of particles in deionized water (pH ≈ 5.0), for SiOC, SiOC-B7, SiOC-B7Ca5, SiOC-Ca5, SiOC-Ca12 and 45S5; (b) Schematic illustration of zeta potential evolution with soaking time during the SBF test for 45S5, Si(Ca,B)OC and SiOC. Shadowed region refers to the first 8 h of soaking, during which the zeta potential was measured in the present study. It is seen, that the samples are assumed to show the same evolution concerning their zeta potential, i.e., approaching in a first step the zeta potential value of silica (gel) and subsequently evolving towards the value of HA. The difference between the samples relies only (and mainly) on the different time needed to develop the HA precipitates on their surface.	55
Figure 4-11. XRD diffractograms of silicon oxycarbide based and 45S5 samples (a) before SBF soaking and (b) after 4 weeks soaking in SBF.	57
Figure 4-12. FTIR spectra of silicon oxycarbide based and 45S5 samples (a) before SBF soaking and (b) after 4 weeks soaking in SBF.	59
Figure 4-13. SEM micrographs obtained at the earliest time points of the individual samples to visually detect hydroxyapatite formation after SBF exposure.	60
Figure 4-14. XRD patterns of Si(B,Ca,Sr)OC samples and SiOC-B7Ca5.	64
Figure 4-15. Evolution of pH value of the filtered SBF solutions as a function of the soaking time for Si(B,Ca,Sr)OC samples and SiOC-B7Ca5.	66
Figure 4-16. Evolution of (a) Si concentration, (b) Ca concentration, (c) P concentration and (d) Sr concentration of the filtered SBF solutions as a function of the soaking time for Si(B,Ca,Sr)OC samples and SiOC-B7Ca5.	68
Figure 4-17. XRD patterns of Si(B,Ca,Sr)OC samples and SiOC-B7Ca5 (a) after 3 days SBF soaking and (b) after 7 days SBF soaking.	70
Figure 4-18. SEM surface morphology of SiOC-B7Ca5Sr0.8 and SiOC-B7Ca5Sr4 after 1 day, 3 days and 7 days SBF soaking.	72
Figure 4-19. (a) FTIR spectra and (b) XRD diffractograms of xerogels SG-Ca0, SG-Ca5, SG-Ca12 and SG-Ca50.	75
Figure 4-20. (a) FTIR spectra and (b) XRD diffractograms of silicon oxycarbide samples SiCa0, SiCa5, SiCa12, SiCa50 (samples obtained from corresponding xerogel precursors via pyrolysis at 1100 °C in Ar atmosphere).	76
Figure 4-21. Deconvolution of FTIR spectra (black lines) between 600 cm ⁻¹ and 1500 cm ⁻¹ for (a) SiCa0, (b) SiCa5 and (c) SiCa12 into LO v(Si-O-Si), TO v(Si-O-Si), overlapping v(Si-O-Si)/v(Si-C) (OV) and Q ³ components (red lines). The sum of all fitted peaks yields the blue lines in spectra.	78
Figure 4-22. N ₂ sorption isotherms of SG-Ca0 and SiCa0 in (a), SG-Ca5 and SiCa5 in (b) and the BJH desorption particle size distribution calculated for SG-Ca0 and SiCa0 in (c) and SG-Ca5 and SiCa5 in (d).	81
Figure 4-23. Optical pictures of gels, aged gels and xerogels prepared in sol-gel process (see Figure 3-2).	81
Figure 4-24. N ₂ sorption isotherms of SG-Ca12 and SiCa12 in (a), SG-Ca50 and SiCa50 in (b) and the BJH desorption particle size distribution calculated for SG-Ca12 and SiCa12 in (c) and SG-Ca50 and SiCa50 in (d).	83
Figure 4-25. Schematic illustration of the porosity evolution from gels to xerogels and then to silicon oxycarbide materials and the porosity dependency on the designed Ca/Si molar ratio.	84
Figure 4-26. SEM surface morphology analysis of (a) SiCa0, (b) SiCa5, (c) SiCa12 and (d) SiCa50.	85
Figure 4-27. (a) FTIR spectra and (b) XRD diffractograms of silicon oxycarbide samples after 7 days SBF test.	87
Figure 4-28. SEM surface morphology analysis of silicon oxycarbide samples after 7 days SBF test: (a) SiCa0-T, (b) SiCa5-T, (c) SiCa12-T and (d) SiCa50-T. The hydroxyapatite precipitation is marked in white circles for SiCa12-T.	88

List of Tables

Table 2-1. Summary of cytotoxic investigations on silicon oxycarbide materials in literature.....	22
Table 3-1. The amounts of Silres® MK, calcium acetylacetonate, boric acid and strontium acetylacetonate used for the preparation of the precursor mixtures and the corresponding molar ratios.	26
Table 3-2. Amounts of chemicals for sol-gel procedure.	27
Table 3-3. Reagents for the preparation of SBF solution.	29
Table 4-1. Silicon site fractions in the prepared silicon oxycarbides determined from ²⁹ Si MAS NMR spectra.	42
Table 4-2. Boron site fractions in SiOC-B7 and SiOC-B7Ca5 determined from ¹¹ B MAS NMR spectra.	43
Table 4-3. Network connectivity value NC calculated based on NMR data; the value of vitreous silica SiO ₂ is given for the sake of comparison.	45
Table 4-4. Elemental contents, empirical formulae and estimated phase compositions of the prepared Si(B,Ca)OC samples.....	46
Table 4-5. Mean particle size d ₅₀ , BET specific surface area (SSA) analysis and total pore volume of silicon oxycarbide based samples and 45S5.	48
Table 4-6. Average Si release rates (values normalized to Si content in amorphous silicon oxycarbide network) between 3 days and 4 weeks soaking time.	62
Table 4-7. BET specific surface area (SSA) analysis and total pore volume of Si(B,Ca,Sr)OC samples, with comparison to that of SiOC-B7Ca5.....	65
Table 4-8. Percentual peak area to the total fitting area and area ratios of fitted components and the calculated LO-TO splitting from LO and TO peak centers for SiCa0, SiCa5 and SiCa12.	79
Table 4-9. Elemental contents, empirical formulae and estimated phase compositions of prepared silicon oxycarbide samples.	80
Table 4-10. BET specific surface area (SSA) values calculated for xerogel samples and silicon oxycarbide samples from N ₂ sorption isotherms.	83

Curriculum Vitae

Personal Data:

Name: Fangtong Xie

Date of birth: July 17, 1990

Nationality: Chinese

Education:

Since 08.2016 Technical University of Darmstadt

PhD candidate in Materials Science

10.2012 – 11.2015 Technical University of Darmstadt

Graduation: M.Sc. Materials Science

09.2007 – 07.2011 Xiamen University, Xiamen, China

Graduation: B.Eng. Materials Science and Engineering

List of publications

Xie, F.; Gonzalo-Juan, I.; Breitzke, H.; Fasel, C.; Trapp, M.; Buntkowsky, G.; Kleebe, H.-J.; Riedel, R.; Boccaccini, A.R.; Ionescu, E. Effect of Ca and B Incorporation into Silicon Oxycarbide on its Microstructure and Phase Composition. *J. Am. Ceram. Soc.* **2019**, *102*, 7645–7655. (IF: 3.1)

Xie, F.; Gonzalo Juan, I.; Arango-Ospina, M.; Riedel, R.; Boccaccini, A.R.; Ionescu, E. Apatite Forming Ability and Dissolution Behavior of Boron- and Calcium-Modified Silicon Oxycarbides in Comparison to Silicate Bioactive Glass. *ACS Biomater. Sci. Eng.* **2019**, *5*, 5337–5347. (IF: 4.5)

Arango-Ospina, M.; **Xie, F.**; Gonzalo-Juan, I.; Riedel, R.; Ionescu, E.; Boccaccini, A.R. Review: Silicon Oxycarbide Based Materials for Biomedical Applications. *Appl. Mater. Today* **2019**, 100482. (IF: 8.0)

Xie, F.; Ionescu, E.; Arango-Ospina, M.; Riedel, R.; Boccaccini, A.R.; Gonzalo-Juan, I. Facile Preparative Access to Bioactive Silicon Oxycarbides with Tunable Porosity. *Materials* **2019**, *12*, 3862. (IF: 3.0)

Liu, X.; Xu, H.; **Xie, F.**; Yin, X.; Riedel, R. Light-weight and Highly Flexible TaC Modified PyC Fiber Fabrics Derived from Cotton Fiber Textile with Excellent Electromagnetic Shielding Effectiveness. *Chem. Eng. J.* **2020**, 387, 124085. (IF: 8.4)

Liu, X.; Xu, H.; **Xie, F.**; Fasel, C.; Yin, X.; Riedel, R. Highly Flexible and Ultrathin Mo₂C Film via in-situ Growth on Graphene Oxide for Electromagnetic Shielding Application. *Carbon* **2020**. In Press. (IF: 7.5)